ISTITUTO ITALIANO DI TECNOLOGIA
SYNAPTIC NEUROSCIENCE

enTRAIN Vision
European Network for integrated TRAINing on innovative therapies for vision restoration

UNIVERSITÀ DEGLI STUDI DI GENOVA

PhD course in

Neuroscience and Neurotechnology (XXXVI cycle)

INJECTABLE PHOTOACTIVE DEVICES FOR RETINAL PROSTHESIS: DESIGN, SYNTHESIS AND TESTING OF POLYMER-BASED NANOPARTICLES

Jasnoor

Supervisors: Prof. Fabio Benfenati and Dr. Elisabetta Colombo

November 2023

ACKNOWLEDGMENTS

It is said that our brain has about 100 billion neurons – which is about as many galaxies in the observable Universe. Galaxies house star clusters, which in turn have several stars tied together in shared synergy. Well, I feel like such a star emerging from a cluster, absorbing, and reflecting the collective brilliance of many.

Foremost, I sincerely acknowledge my supervisor, Professor Fabio Benfenati, for giving me the opportunity to pursue my Ph.D. in his lab. I feel incredibly fortunate to have the mentorship of such a highly respected academic, whose guidance, expertise, and supervision steered me through this research. Your commitment to supporting early-stage researchers is evident in the countless opportunities you provide for growth and collaboration, fostering a community of learning.

To Dr Elisabetta Colombo, my co-supervisor, I owe a debt of gratitude that words can barely encompass. From the initial stages of refining my research proposal to the final submission of my thesis, you have been tirelessly committed to my intellectual and personal growth. I highly valued our frequent meetings, which not only served as crucial checkpoints to keep me on track academically but also provided me with plenty of encouragement. I deeply appreciate your scientific approach, attention to detail, and enthusiasm for cross-disciplinary research.

Special thanks to Professor Guglielmo Lanzani for your time, advice, and contribution to the realization of this academic milestone.

This endeavor would not have been possible without the support of the Marie Skłodowska-Curie Scholarship funded by the European Union. In the enTRAIN Vision Network, I forged connections that transcended professional boundaries and evolved into invaluable friendships. My academic journey took me to several conferences in Europe, the United States, and Japan, providing a wealth of experiences that will resonate throughout my career and beyond. I sincerely thank Aurelie, Rossana, Arta, Ilaria, and Diego for being the pillars of crucial administrative and technical support throughout my time in Italy.

In the embrace of a foreign land, I was challenged and inspired, pushed beyond my comfort zone, and compelled to adapt to new cultures, languages, and perspectives. My journey intersected with those of many, and I have immense love for my friends: Marwa, Alessandra, Bhavya, Garima, Itika, Alicja, and Janina. Each of you impacted me in so many unsaid ways, I am blessed to have you all to learn from and lean on, through it all.

The most significant acknowledgment is reserved for my parents, it is the love and support they have provided me that has enabled me to achieve everything that I have and ever will. Nanki, you are a powerhouse of positivity; your bubbly laughter fades away all my stress.

I dedicate this thesis to my husband, whose love for me never changed, whether the experiments succeeded or failed. Mann, thank you for enduring my endless amount of panic with your best smile and kind words. Your extraordinary belief in me makes every challenge seem conquerable. I cherish the gift of your wonderful family, a source of warmth that makes me feel so special and loved.

I express my gratitude to all those who made this journey possible.

Thank you for making me shine brighter each day!

ABSTRACT

The past three decades have witnessed tremendous research to bridge the gap between simulated and natural vision. With a fair share of breakthroughs and challenges, visual restorative therapy continues to fuel interest amongst the scientific community globally. Age-related macular degeneration and Retinitis pigmentosa are among the top untreatable, chronic neurodegenerative eye diseases responsible for debilitating lives of millions of people.

Different therapeutic methods have been investigated including gene replacement, optogenetics, stem cell therapy, and electronic retinal prostheses, among which the latter holds the longest development period. Subretinal retinal approaches have shown encouraging results for a partial enhancement in vision acquired by targeting the residual inner retinal neurons, exploiting various stimulation mechanisms. Notwithstanding the scientific community's efforts in enhancing a suitable retinal restorative stimulation tool, surgical invasiveness, and genetic modification still represent a bottleneck in the field of retinal degeneration therapies, together with the inability to provide high-resolution vision.

Over recent years, significant advancements have been achieved in retinal prosthetics, primarily driven by the shift from inorganic to organic devices that utilize conjugated polymers. A potential breakthrough involves the development of injectable conjugated polymeric nanoparticles serving as a "liquid" retinal prosthesis.

This thesis aims to explore a prospective enhancement of the "liquid" retinal concept by incorporating graphene to a novel co-polymeric formulation of the previously developed injectable nanoparticles. It outlines the design and fabrication of P3HT:PCBM nanoparticles with graphenic core via the nanoprecipitation method. The comprehensive evaluation of physical properties confirms the formation of a reproducible, stable, and fairly monodisperse population. *In vitro* viability experiments on primary neuronal cultures and *ex vivo* multi-electrode recordings from dystrophic retinal explants show good biocompatibility of the nanoparticles, localization on the cell membrane without internalization over time, and increased firing modulation of retinal neurons upon illumination. These results overall suggest that graphene could be successfully embedded in nanoparticles of photovoltaic polymers and represents a potential new strategy for the development of an injectable light-sensitive neurostimulation tool.

TABLE OF CONTENTS

LIST OF FIGURES

LIST OF ABBREVIATIONS

AMD	**A**ge-related **M**acular **D**egeneration
AOSLO	**A**daptive **O**ptics **S**canning **L**aser **O**phthalmoscopy
CNV	**C**horoidal **N**eo **V**ascularization
CS	**C**onditioned **S**timulus
DIV	**D**ays **I**n **V**itro
DLS	**D**ynamic **L**ight **S**cattering
ERG	**E**lectro **R**etino **G**raphy
FA	**F**luorescein **A**ngiography
FAF	**F**undus **A**uto **F**luorescence
GA	**G**eographic **A**trophy
GO	**G**raphene **O**xide
HEK	**H**uman **E**mbryonic **K**idney
HOMO	**H**ighest **O**ccupied **M**olecular **O**rbital
ICGA	**I**ndo **C**yanine **G**reen **A**ngiography
iPSCs	**i**nduced **P**luripotent **S**tem **C**ells
LUMO	**L**owest **U**noccupied **M**olecular **O**rbital
MEA	**M**ulti-**E**lectrode **A**rray
MNV	**M**acular **N**eo **V**ascularization
MPEG-PLGA	**M**ethoxyl **P**oly-(**E**thylene **G**lycol)–**P**oly-(**L**actic-co-**G**lycolic **A**cid)
NMR	**N**uclear **M**agnetic **R**esonance
NPs	**N**ano**P**articles
NTA	**N**anoparticle **T**racking **A**nalysis
OCP	**O**rganic **C**onjugated **P**olymers
OCT	**O**ptical **C**oherence **T**omography
OCTA	**O**ptical **C**oherence **T**omography **A**ngiography
P3HT	**P**oly(3-**H**exyl**T**hiophene)
PCBM	**P**henyl-**C**61-**B**utyric-acid-**M**ethyl-ester
PdI	**P**oly**d**ispersity **I**ndex
PDMS	**P**oly**d**i**m**ethyl**s**iloxane
PEDOT:PSS	**P**oly(3,4-**E**thylene**d**i**o**xy**t**hiophene) **P**oly**S**tyrene **S**ulfonate
PEGMA	**P**oly (**E**thylene **G**lycol) **M**ethyl meth**A**crylate
PET	**P**oly**E**thylene **T**erephthalate
PSTH	**P**eri **S**timulus **T**ime **H**istogram
RCS	**R**oyal **C**ollege of **S**urgeons
rd10	**r**etinal **d**egeneration **10**
rdy	dominant **r**od-cone **dy**splasia
RGC	**R**etinal **G**anglion **C**ell
RP	**R**etinitis **P**igmentosa

RPC	**R**etinal **P**rogenitor **C**ells
RPE	**R**etinal **P**igment **E**pithelium
SAE	**S**erious **A**dverse **E**ffects
SDS	**S**odium **D**odecyl **S**ulfate
SPN	**S**emiconducting **P**olymeric **N**anoparticles
TEM	**T**ransmission **E**lectron **M**icroscopy
THF	**T**etra **H**ydro**F**uran
TRPV1	**T**ransient **R**eceptor **P**otential **V**anilloid member **1**
US	**U**nconditioned **S**timulus
VEGF	**V**ascular **E**ndothelial **G**rowth **F**actor
VEP	**V**isually **E**voked **P**otential
VPU	**V**ideo **P**rocessing **U**nit

1 INTRODUCTION

1.1 VISION IMPAIRMENT AND RETINAL DEGENERATION

Of all the given human senses, sight is by far the most valued ability, since it corresponds to the majority of information that we absorb from our five combined senses[1]. Vision impairment and blindness rank among the most feared sensory disabilities and affect an estimate of 596 million and 43 million people respectively[2]. Most patients with vision impairment exhibit a loss of quality of life and sometimes are rendered incapable of performing everyday tasks without assistance. Suffering from visual impairment or blindness can profoundly impact access to education and job opportunities, especially in low-income settings. This can lead to various physical and psychological health issues[3] in addition to posing a substantial economic burden, with projected productivity losses reaching up to 16.5 billion USD in the United States alone[4]. The primary reason for blindness (51%) is cataract, which can be effectively treated to restore vision. Other significant contributors include hereditary retinal diseases, such as Retinitis pigmentosa (RP), or other neurodegenerative conditions, including age-related macular degeneration (AMD), posing a considerable societal burden, especially as the world population ages[2,5,6].

At the centre of the retina sits the macula, comprising of the cone-rich region of fovea, which plays an essential role in contributing to high acuity vision. Although the fovea comprises less than 4% of the total retinal area, it is responsible for almost all our photopic information, thereby providing retinal input to thevisual cortex. Photoreceptors are situated in the outer retinal layers and are highly differentiated cells containing light-sensitive pigments that drive phototransduction, i.e., generation of neural signals in response to light stimulation. These signals undergo intricate processing by a neural network before being sent to retinal ganglion cells (RGCs) located in the inner layers. The axonal extensions of RGCs constitute the optic nerve, transmitting light-triggered neural signals to the visual cortex. The degeneration of photoreceptors is a complex phenomenon, impacted by numerous genes, as well as by environmental factors. It triggers retinal remodelling, leading to cell death and subsequent retinal topology restructuring[7], causing changes at morphological as well as physiological level. Regardless of which photoreceptors undergo degeneration first, inner retinal rearrangements occur in conjunction with and subsequent to the death of both rods and cones. Concurrent with the loss of photoreceptors, glial mobilization in the outer retina cells can be observed. Resident microglia become activated and migrate to the superficial layers of the retina to engulf and clear dying photoreceptors. Müller glial cells experience hypertrophy, leading to the formation of a scar that fills the typical subretinal space[8]. The next morphological alterations can be seen in bipolar and horizontal cells, which show dendrite retraction, reduction and mislocation, causing outer plexiform layer thinning. Physiologically, alterations involve modifications in their responsiveness to glutamate and a substantial modification in the expression of metabotropic glutamate receptor (mGluR6) and ionotropic glutamate receptor (iGluR) channels in the degenerated retina. This points to a shared biological pattern in response to neural deafferentation, effectively reprogramming the remaining retina by transforming rod

and ON bipolar cells into an OFF bipolar cell phenotype[9]. Amacrine cells, initially stable, later exhibit chemical alterations and formation of new, abnormal synaptic connections within networks. These alterations could potentially play a role in the observed oscillatory signals in degenerating retinas recognized as a distinctive feature in animal models of RP[10]. However, in the long term, amacrine cells tend to exhibit greater survival compared to bipolar cells and retain their responsiveness to iGluR. A decline in the inner nuclear layer and RGC layer was observed in retinas derived from aged RP donors[11] which could be attributed to a reduction in the number of RGCs[12]. Comparing healthy retinas with the ones having degenerated photoreceptors, the spontaneous firing rate of RGCs in darkness was found to be higher in the latter[13–15]. This hyperactivity emerges concurrently with the loss of light responses. RGCs can be categorized broadly into ON-RGCs, OFF-RGCs, and ON/OFF-RGCs, with the strongest evidence for hyperactivity found in OFF-RGCs[13,16]. The emergence of oscillatory activity in the outer and inner retinal network reflects upon the intrinsic properties of the retinal network unleashed by the loss of photoreceptor input onto the ON-bipolar cell pathway[17].

1.1.1 RETINITIS PIGMENTOSA

Retinitis pigmentosa[18,19] encompasses a diverse group of genetically heterogeneous retinal disorders that result in the gradual degeneration of rods followed by cones (**Figure 1**). Typically, this degeneration begins in the mid-peripheral retina and advances toward the macula and fovea, leading to the characteristic “tunnel vision”. Initially, central vision is retained and affected individuals can read and recognize faces, despite experiencing tunnel vision and night blindness due to rod degeneration. Eventually, visual impairment stems from the progressive decline in cone function and soon tunnel vision deteriorates into complete blindness. Cone degeneration is triggered by various factors linked to rod degeneration, including (i) release of toxic substances through gap junctions from dying rods[20], (ii) damage inflicted by microglia migrating to the outer retina[21,22], (iii) absence of a growth factor for cones produced by rods[23], and (iv) significant damage caused by reactive oxygen species due to an excess of oxygen following rod cell death[24]. With an age of onset that varies from childhood to adulthood, RP affects approximately 1 in 4000 people worldwide[25], resulting in considerable social and economic challenges.

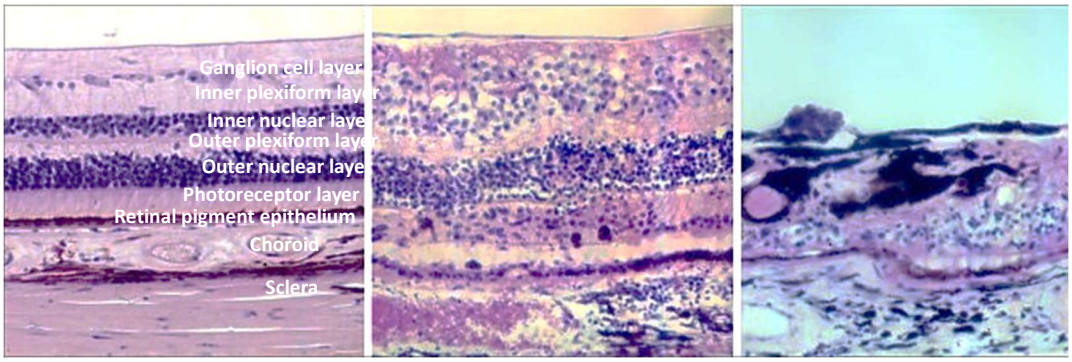

Figure 1. Histological cross-section of the human retina (healthy v/s RP affected). Left: healthy retina; middle: retina of a patient with mid-stage RP; right: retina of a patient with late-stage RP. Image taken from Konieczka et al. 2012.

GENETICS AND PATHOGENESIS

While RP was initially described in 1857 within the context of retinal dystrophies, its genetic underpinnings were only identified in 1999. Since then, nearly 3000 genetic mutations involving over 70 genes have been associated with RP[26] showing substantial genetic overlap with other types of retinal dystrophies. RP can be inherited in an autosomal dominant, autosomal recessive, or X-linked manner. Autosomal dominant and recessive patterns account for 15-35% and 5-45% of cases, respectively, while X-linked inheritance constitutes 5-17% of cases. Moreover, 38-50% of cases involve *de novo* mutations (simplex cases), lacking any familial history of the disorder[27]. The intricate genetic pathophysiology of RP poses significant challenges for its treatment with gene therapy.

CLINICAL PICTURE AND DIAGNOSIS

The clinical onset of RP exhibits significant variability: some individuals experience visual loss during childhood, while others remain asymptomatic until their mid-adulthood. This diverse onset and progression of the disease contribute to delayed

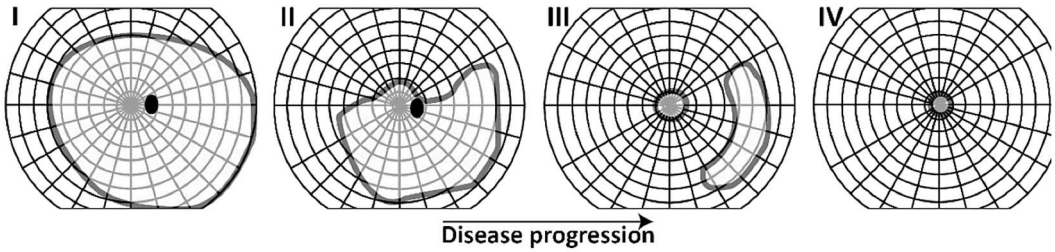

Figure 2. Kinetic perimetry assessment of visual field progression in a patient with RP. (I) Early RP: visual fields may appear normal despite underlying visual field defects; (II, III) Visual field constriction occurs over time, with defects typically showing symmetry and expanding outwards faster than they do inwards; (IV) End RP: a small central portion of visual field, commonly referred to as "tunnel vision" may remain. Progression pattern of visual field loss can vary between individuals. Image taken from Nguyen et al. 2023.

diagnoses, ultimately limiting the potential advantages of therapeutic interventions. Typically, in the early stages of the disease, the main symptom is nocturnal visual loss (nyctalopia), resulting from the initial degeneration of rods. This symptom becomes apparent as patients encounter situations with distinct patterns, such as difficulties noticing pedestrians along the sides of the road or recognizing objects while driving. Additionally, patients may develop photophobia[28], photopsia[29,30], and in some cases, dyschromatopsia[31]. Reading difficulties due to a decline in visual acuity may also arise. As the disease advances to its later stages, patients experience heightened photophobia and develop tunnel vision, with only a limited visual field remaining around the fixation point. At this point, approximately 90% of foveal cones have degenerated, resulting in central vision loss[32]. The complete clinical picture becomes evident only when the disease has progressed to a mid-stage, characterized by nearly compromised rod function, ongoing degeneration of peripheral cones, and initiation of the tunnel vision phenomenon.

Clinical assessment serves as a crucial initial step in diagnosing RP and plays a pivotal role in monitoring the disease's progression. Various techniques are available for testing retinal appearance and function as the disease advances through its different stages, such as: (i) perimetry (kinetic, static or fundus driven) (**Figure 2**), (ii) color vision assessment (e.g., with Ishihara plates), (iii) dark adaptometry, and (iv) electroretinography (e.g., full-field electroretinography, multifocal electroretinography) (**Figure 3**). Retinal imaging also can aid in the characterization and diagnosis of RP; several techniques have been employed for this purpose, as described below.

(i) Fundus imaging aims to offer insights into various aspects, including the presence of bone spicule pigmentary deposits (a parameter that indicates the disease's advancement), the structure of blood vessels, and the optic disc opacity (**Figure 4**) [28].

(ii) Fluorescence angiography (FAF) surpasses conventional fundus imaging by providing a precise understanding of Retinal Pigment Epithelium (RPE) disruption, achieved through the utilization of autofluorescent pigment known as lipofuscin[33]. In the earlier stages of RP, a hyper-autofluorescent ring around the macula is frequently observable[34]. This ring serves as an indicator of the border regions where the retina transitions from healthy to degenerating. As RP advances into its later stages, marked by extensive photoreceptor and RPE degeneration leading to decreased lipofuscin levels in these tissues[35], FAF reveals widespread areas of reduced autofluorescence.

(iii) Optical Coherence Tomography (OCT) can identify early signs of outer segment shortening[36], contingent upon the disease's progression. Some patients at later disease stages might exhibit outer nuclear layer narrowing[37] in parallel with inner nuclear layer and RGC layer thickening, potentially due to retinal remodelling that involves neurons and glial cells[38]. Hence, OCT serves as a sensitive and non-invasive method capable of documenting disease progression. Moreover, it permits the identification of the hyper-reflective layer, also known as the Ellipsoid Zone, which typically experiences relatively milder photoreceptor loss (**Figure 5**).

(iv) Adaptive optics scanning laser ophthalmoscopy (AOSLO) aims to compensate for the eye’s aberrations and achieves resolution close to the diffraction limit. The technique enables the detection of photoreceptor damage that might not be visible using OCT[39]. Additionally, it has the capacity to unveil a decrease in cone photoreceptor density prior to the onset of visual acuity impairment. This observation implies that AO-based imaging tools might offer precise anatomical measures for evaluating outcomes in clinical trials.

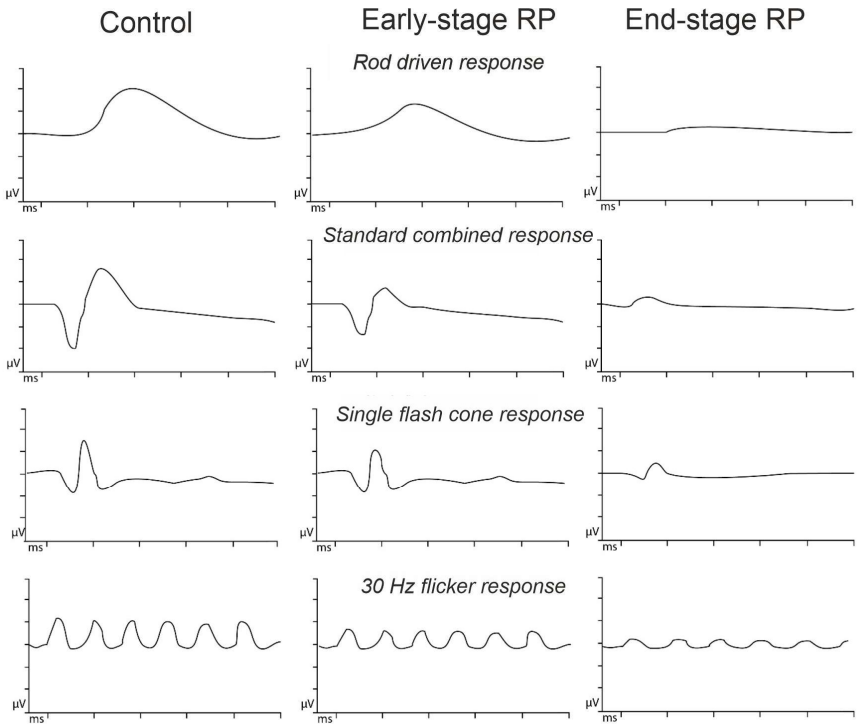

Figure 3. Example full-field electroretinography recordings (healthy v/s RP patients). Diagnosis of RP is established using diverse stimuli, following guidelines of the International Society for Clinical Electrophysiology of Vision (ISCEV). In advanced disease stages, RP patients often exhibit a significant reduction or even absence of rod-driven responses, although some cone-driven responses may persist. Image taken from Nguyen et al. 2023.

TREATMENTS

RP treatments can be grouped into two main groups: preventive and restorative.

Nutritional therapy

Preventative strategies frequently involve oral supplementation with Vitamin A, Vitamin E, lutein, and docosahexaenoic acid. The idea behind Vitamin A supplementation rests on its role as a crucial chromophore in the visual cycle, potentially compensating for deficiencies in RP patients. Nevertheless, less than 10% of RP-linked genes relate to

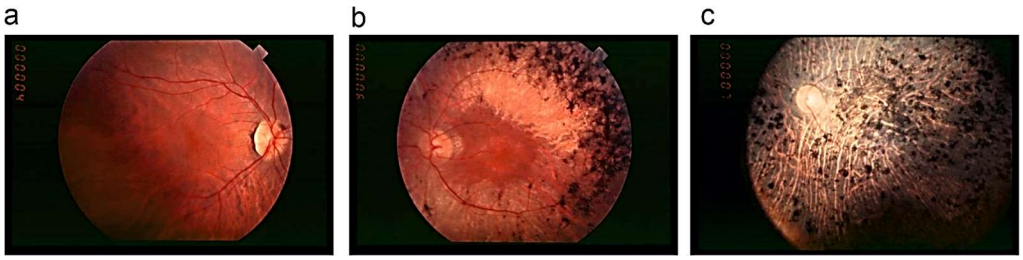

Figure 4. Fundus images of an RP patient. (a) early-stage: fundus appears normal, bone spicule-shaped pigment deposits absent or rare, modest retinal arterioles constriction; (b) mid-stage: bone spicule-shaped deposits in mid-periphery, retinal atrophy, preserved macula with a peripheral ring of depigmentation and attenuated retinal vessels; (c) end-stage: widespread pigment deposits across the retina, narrow retinal vessels, and pale optic disc.

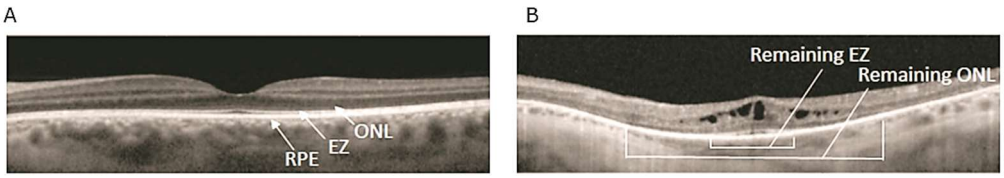

Figure 5. Optical Coherence Tomography (healthy v/s RP-affected retina). (A) Normal OCT scan showing intact RPE, ellipsoid zone (EZ), and outer nuclear layer (ONL); (B) OCT scan revealing a central foveal region with an island of ellipsoid zone and outer nuclear layer surrounded by atrophy in these layers, along with foveal cystoid macular oedema, a frequently observed consequence of RP.

Vitamin A metabolism[40]. B-Carotene, a dimerized form of Vitamin A, exhibits better tolerability; however, its inconsistent monomerization makes it an inadequate substitute for Vitamin A treatments. Conversely, Vitamin E was swiftly disregarded due to an accelerated ERG decline[41]. Another candidate in oral supplement treatments is docosahexaenoic acid, an omega-3 fatty acid highly concentrated in photoreceptor membranes containing rhodopsin and cone opsins. Docosahexaenoic acid expression is found to be less in RP patients as compared to healthy individuals. In one study, the authors observed that simultaneous supplementation of both Vitamin A and docosahexaenoic acid was beneficial for retinal health and could potentially extend vision preservation by a decade if initiated early enough[42]. However, the overall evidence supporting nutritional supplements for RP patients is not robust. While such supplements might slow down disease progression in inherited retinal dystrophies closely tied to the Vitamin A pathway in the retina, their definite benefits remain insufficiently proven by studies[40]. In recent years, investigations have turned to lutein, a carotenoid found in dark green leafy vegetables, and zeaxanthin, another carotenoid naturally occurring in the human retina. While control subjects displayed slower visual field sensitivity loss in comparison to those with RP, the outcomes were only modest[43].

Gene Therapy

Ocular genetic therapies have emerged as a promising treatment approach for various inherited retinal dystrophies[44,45], due to the eye's compartmentalized nature, immune privilege, and relative accessibility for localized administration. Gene-based strategies

Disease/Gene	Vector/Strategy	Drug	Phase	Sponsor/Company
arRP MERTK58	AAV, SR	AAV2-VMD2-hMERTK	I	King Khaled Eye Specialist F
arRP PDE6A	AAV, SR	AAV8-hPDE6A	I/II	RD-CURE
arRP PDE6B	AAV, SR	AAV5-hPDE6B	I/II	Horama
arRP RLBP1	AAV, SR	AAV8-hRLBP1 (CPK850	I/II	Novartis
RP, X-linked RPGR	AAV, SR	AAV8-RPGR	II/III	NightstaRx/Biogen
RP, X-linked RPGR	AAV,SR	AAV5-hRKp-RPGR	I/II	LTFU MeiraGTx
RP, X-linked RPGR	AAV,SR	AAV2tYF-GRK1-RPGR	I/II	AGTC
RP, X-linked RPGR	AAV, IVT	AAV.R100-RPGR	I/II	4D Molecular Therapeutics
RP, late stage Gene-independent	AAV, IVT	AAV-ChR2	I/II	Allergan
RP, late stage Gene-independent	AAV, IVT	AAV2.7m8-CAG-ChrimsonRtdTomato	I/II	Gensight
adRP RHO	AON, IVT	QR-1123 (RHO-P23H specific)	I/II	ProQR

Figure 6. Gene therapy approaches for RP. To date gene therapy strategies to treat RP.

are most impactful during the initial stages of the disease, aiming to halt further degeneration of surviving target cells. However, it is important to note that they cannot

restore cells that have already undergone degeneration. The approach can be applied either as a knock-in strategy (compensating a loss-of-function) or a knock-down strategy (removing a gain-of-function). In 2017, the U.S. Food and Drug Administration (FDA) granted approval for the first *in vivo* gene therapy treatment for Leber's congenital amaurosis, known as voretigene neparvovec (AAV2-hRPE65v2), or commonly referred to as Luxturna. This therapy targeted the RPE65 gene, a mutation found in various retinal dystrophies, including RP[46]. For gene therapy targeting RP, a substantial number of preclinical programs centered on gene supplementation exist, with few currently in the clinical trial phase (**Figure 6**). Except for one clinical study, all the other ongoing trials are based on gene supplementation strategies, specifically designed to address recessive forms of RP. Given RP's progressive nature, these gene therapies are not suitable for patients in the advanced stages of the disorder, characterized by significant degeneration and photoreceptor loss. As a result, alternative methods have been developed to manipulate the remaining retinal circuitry (e.g., combining gene therapy with optogenetics[47]).

Stem cell therapy

Stem cell therapy allows to restore the functionality of impaired retinal cells by either replacing or repairing them[48]. This approach is potentially applicable to any RP patients, irrespective of their genotype. The therapy can be classified based on its intended impact—either cell replacement or preservation—and the specific type of stem cells employed, which includes embryonic stem cells, induced pluripotent stem cells (iPSCs), hematopoietic stem cells, mesenchymal stem cells, and retinal progenitor cells[49,50]. Retinal progenitor cells sourced from human embryonic stem cell and transplanted into the ganglion cell layer prompted an increase in outer nuclear layer thickness, although the longevity of the transplanted cells was limited[51]. In separate experiments, iPSCs were subretinally transplanted into monkeys and rats. These iPSCs formed synaptic connections with host bipolar cells, resulting in improved ERG responses[52]. In another mouse model, transplantation of iPSC-derived RPE spheroids effectively delayed thinning of the outer nuclear layer [53]. In Royal College of Surgeon (RCS) rats with the *Mertk* mutation, the same iPSC-derived RPE transplant exhibited partial rescue of visual function, although it induced some inflammatory reaction[54]. Moreover, in a rat model of retinal degeneration, the co-transplantation of both RPCs and RPE cells derived from iPSCs yielded promising outcomes in terms of visual responses and preservation of the outer nuclear layer[55]. In humans subjected to treatment with mesenchymal stem cells derived from bone marrow, initial enhancements in best-corrected visual acuity were reported; however, their visual acuity returned to baseline levels at the 12-month evaluation[56]. In recent times, cell transplantation for RP has progressed to clinical trials, demonstrating effectiveness in enhancing visual quality[57,58]. However, there remain unresolved concerns about the long-term efficacy, potential immune rejection, inflammation and surgical complications[59,60]. Despite the encouraging outcomes of all stem cell approaches, significant challenges arise due to the inherent characteristics of retinal degeneration. In advanced stages of RP, when retinal circuitry remodelling is underway, the retinal structures may become inadequate for effective stimulation. Following the death of photoreceptors, the remodelling of retinal circuitry occurs,

resulting in a structure that may no longer be capable of sustaining vision, even with appropriate stimulation. Moreover, potential abnormal connections between transplanted tissue or a device and the recipient can worsen circuitry issues. As degeneration progresses, extensive gliosis by Müller cells and astrocytes leads to the formation of a glial scar, hindering not only the development of functional synapses but also the proper migration of retinal progenitor cells to their specific neuroanatomical locations, a process already challenging in itself. Improperly executed surgical intervention is likely to worsen tissue gliosis, further limiting the effectiveness of the transplant or implant. Consequently, regardless of the approach—whether it involves cell replacement or artificial prosthetics, it becomes crucial to intervene as early as possible, ideally aligning with the onset of the initial disease stages.

1.1.2 AGE-RELATED MACULAR DEGENERATION

Age-related macular degeneration (AMD) is a neurological condition that impacts the fovea in humans, resulting in a gradual decline in central vision, and in some instances, complete blindness[61]. In developed nations, AMD ranks as the primary cause of visual impairment and blindness among the elderly, affecting approximately 15-20% of the population aged over 65, with more than 190 million individuals worldwide grappling with this condition[62]. The economic significance of finding a remedy is substantial, given the estimated global cost exceeding 300 billion dollars annually[61], and a projected rise in the number of AMD sufferers to as many as 300 million by the year 2040[63] (**Figure 7**). Furthermore, AMD significantly impairs the quality of life for affected individuals. Those with AMD are more prone to experiencing depression, reporting significant life stress, and having lower levels of physical activity compared to their healthy counterparts[64] or individuals of the same age group suffering from other severe chronic health conditions[65]. Additionally, AMD patients face an elevated risk of encountering difficulties in their daily activities[66], often leading to injuries such as falls or accidents[67], which impose additional costs on both families and the healthcare system. Considering these challenges, there is a pressing need to explore new therapies that can enhance the overall quality of life for affected individuals and alleviate the financial burden. Based on the stage of progression[68], AMD can be categorized as (i) early stage, when symptoms are often absent and only limited patients report mild central distortion or diminished visual acuity, when reading under low luminance; or (ii) late stage, which results in

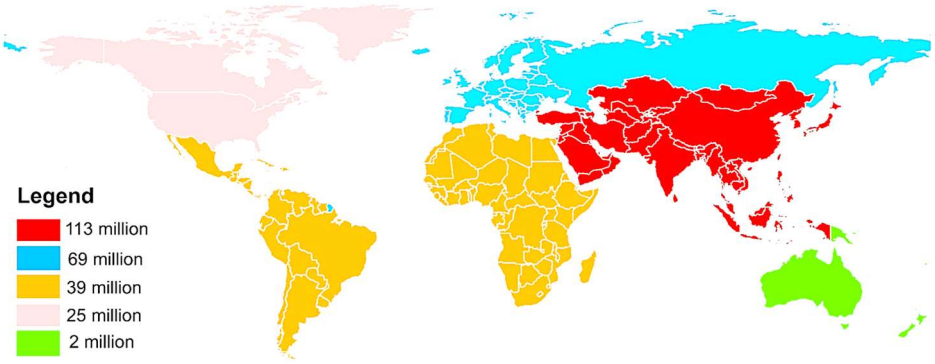

Figure 7. The predicted worldwide occurrence of AMD in 2040. Image taken from Deng et al. 2022.

central vision impairment within the macula, primarily due to the progressive neurodegeneration of photoreceptors and the RPE. It can be further categorized into two subtypes: geographic atrophy (GA) and choroidal neovascularization (CNV) (**Figure 8**).

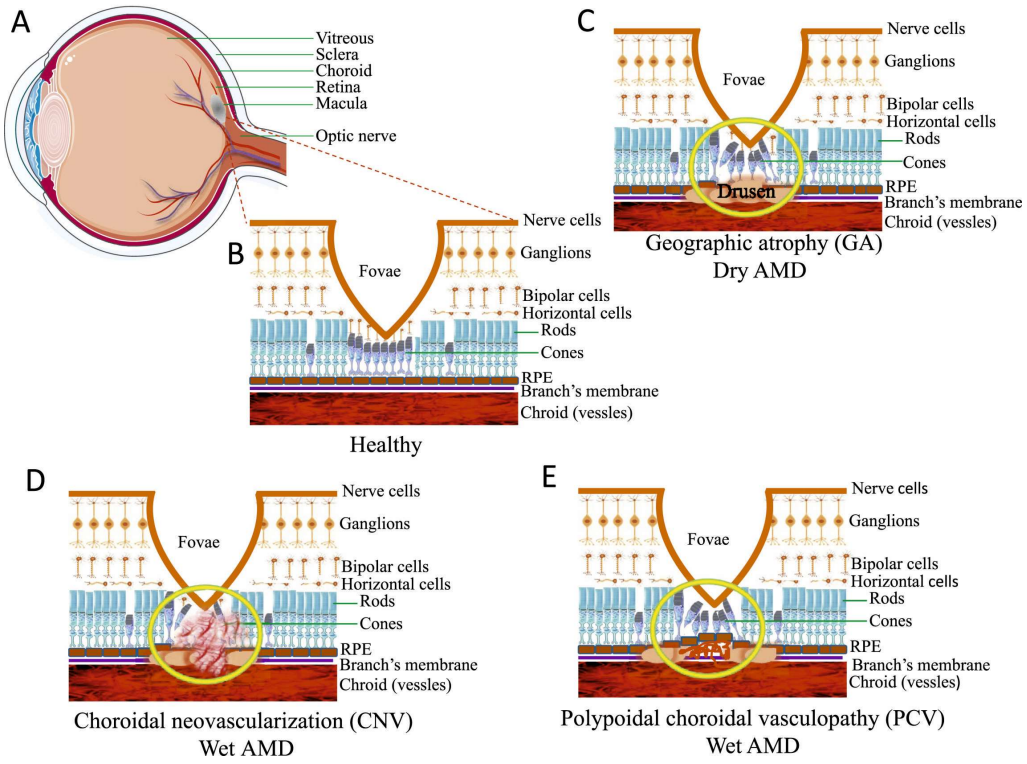

Figure 8. Neovascularization and development of drusen. (A) A cross-sectional view of a typical human eye, indicating the macula's position (diameter 1.5 mm); (B) An enlarged depiction of the retina within the macular region, where the most significant pathological changes occur; (C) The development of drusen, causing atrophy of the retinal tissue and rupture of the Bruch membrane calcification, subsequently leading to AMD; (D) The emergence of choroid polypoid lesion; (E) The proliferation of new blood vessels. Image taken from Deng et al. 2022.

RISK FACTORS AND PATHOPHYSIOLOGY

The development of AMD is influenced by various risk factors, including but not limited to age, ethnicity, and genetic predisposition. Among phenotypic risk factors, drusen deposition between the RPE and Bruch's membrane can be an early indicator of the disease. As the name implies, advancing age represents the primary demographic risk factor for the condition[69,70], with a risk of developing it exceeding threefold in individuals aged 75 or older compared to those aged 65 to 74[71]. Advanced age represents the primary risk factor for AMD because the aging process is linked to alterations in both the structure and function of the retina, making it more susceptible to AMD development. Furthermore, age compounds the influence of other pathological risk factors over time[72]. Smoking consistently emerges as the most frequently cited modifiable risk factor for AMD and is linked to a 2- to 4-fold rise in the risk of developing early AMD[73], or late stage AMD[71,74]. Cigarette smoke is recognized for its harmful constituents that can induce

pathological consequences through various biochemical mechanisms. These include the induction of oxidative stress in the retina, triggering inflammation in RPE cells, and bringing about vascular alterations in the choroidal vessels. Diet is believed to play a possible role in the prevention or postponement of AMD advancement, e.g. Mediterranean diet[75] , fish consumption[76], and mono-saturated fats could have a protective effect[77]. Other factors are likely to play a minor role in increasing AMD risks, such as sunlight exposure, iris colour[71], alcohol consumption[78] and high pulse pressure[79].

At the heart of the disease's progression lies the Bruch's membrane, a multi-layered structure comprising a central core composed of collagen and elastic fibers, surrounded by the innermost basement membrane of the RPE and the outermost basement membrane of the choroid. A prominent characteristic of AMD is the presence of "drusen", debris accumulations of various components, including at least 129 different proteins[80], many of which are involved in regulating the complement system, as well as neutral lipids[81], and zinc and iron ions[82]. These deposits typically manifest in both the peripheral and macular regions, usually situated between the RPE's basement membrane and the inner collagenous layer of Bruch's membrane[83]. Additionally, another type of retinal deposit associated, with AMD is referred to as basal laminar deposits. Comprised of basement membrane proteins and long-spacing collagen[80,84], they are found between the basement membrane of the RPE and its plasma membrane. Variation in morphology, number, size, shape, and distribution of drusen[85,86] can give useful insights into disease progression, thereby making them good prognostic markers toward the final stage of the disease.

Geographic atrophy (GA), also referred to as 'dry AMD' is characterized by the contiguous degeneration of photoreceptors, the RPE, and the choriocapillaris. It is associated with the development of scotomas or areas of impaired vision and is usually eyes symmetric. Over time, these areas of GA tend to expand, leading to progressive loss

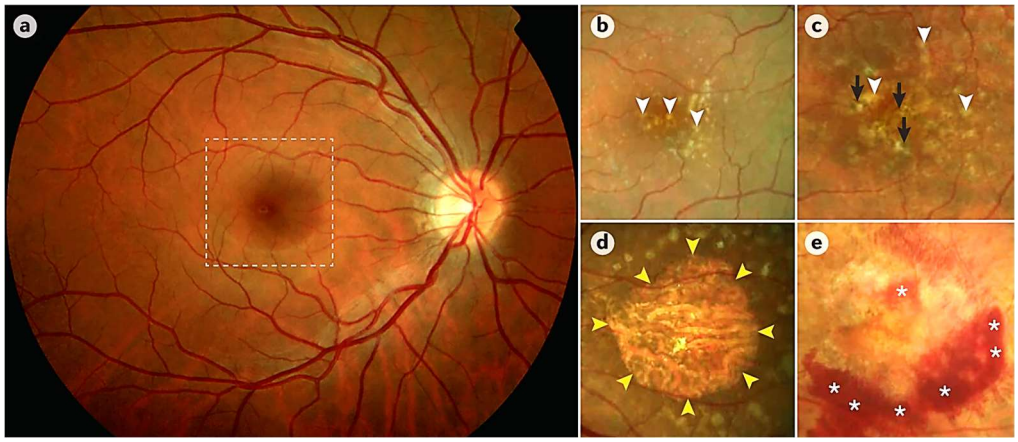

Figure 9. Color fundus photography depicting manifestation of AMD. (a) AMD impacts the central region of the macula, as shown by the square box highlighting this region in a healthy eye; (b) Early AMD with medium-sized drusen (yellowish deposits, indicated by arrowheads); (c) Mid-stage AMD featuring large drusen (arrowheads) and areas of hyperpigmentation (arrows); (d) Geographic atrophy (arrowheads); (e) Neovascular AMD with hemorrhage (asterisks). Image taken from Fleckstein et al. 2021.

of central visual field[87]. In any stage of AMD, new blood vessels may invade the outer retina, subretinal space, or subRPE space, giving rise to a condition known as macular neovascularization (MNV), which is the defining feature of neovascular AMD[88]. The exudative stage of neovascular AMD, also known as 'wet AMD,' becomes evident when these newly formed vessels start to leak or rupture, resulting in the accumulation of fluids and/or hemorrhages. The leaky nature of the new vessels can cause hemorrhage and lead to scar formation, which in turn results in rapid loss of visual function (usually from one eye first) in the macula due to photoreceptor death. If left untreated, exudative MNV often leads to extensive fibrosis and severe central vision loss.

CLINICAL PICTURE AND DIAGNOSIS

Patients typically manifest symptoms such as distortion, blurred vision, or a scotoma in their central field of vision. In neovascular AMD, these symptoms tend to develop suddenly, while in GA, they progress more gradually over time. Typically, in early or intermediate stages, patients remain asymptomatic with visual acuity in normal range, despite the presence of drusen. On the other hand, patients with advanced AMD experience a decline in visual acuity in the affected eye. They may also identify an area of central distortion or a scotoma when using an Amsler grid. In most cases, clinical assessment is adequate for diagnosing AMD. However, more subtle macular irregularities are often better identified with the assistance of ancillary diagnostic tests such as fundus imaging, fluorescein angiography, indocyanine green angiography, optical coherence tomography, optical coherence tomography angiography and artificial intelligence.

(i) Fundus imaging: The clinical manifestation of AMD varies among individuals but often involves specific observable alterations in the fundus of the eye (**Figure 9**). This condition tends to exhibit a high degree of symmetry, particularly in the GA form. In addition to the conventional drusen, pseudodrusen in GA constitute a distinct entity, primarily linked to more advanced disease stages. Neovascular AMD also includes drusen, along with RPE detachment, intraretinal hemorrhages and CNV, among its characteristic features. Fluorescein angiography (FA) is conducted to validate presence of neovascularization and ascertain lesion attributes such as location and composition of neovascularization. It is helpful in distinguishing CNV variations: classic (where new vessels penetrate the RPE resulting in well-defined hyperfluorescent lesions) and occult (where new vessels localize beneath the RPE, leading to ill-defined dye leakage from undetermined source). Indocyanine green angiography (ICGA) provides a more detailed depiction of the choroidal circulation, compared to FA and is helpful in identifying varying CNV.

(ii) Optical coherence tomography (OCT) (**Figure 10**) is a non-invasive technique, capable of providing anatomical cross-section details about the retina, RPE and choroid thickness, an indicator of disease progression (thickness increase indicative of wet AMD, while decrease of dry AMD[89]). A faster and enhanced diagnosis can be conducted with Spectral OCT, which samples multiple points in the optical path simultaneously.

(iii) Optical coherence tomography angiography (OCTA) enables non-invasive

assessment and measurement of the microvascular system under various retinal conditions[90]. In contrast to the gold standard FA, OCTA is less affected by subretinal hemorrhage and offers enhanced vascular clarity, accurate detection, and quantification of CNV lesions. Studies show that the sensitivity for detecting active CNV's using OCT was as high as 80.7%[91].

(iv) Artificial intelligence has tremendous potential in aiding doctors to assess disease conditions as well as formulate optimal treatment plans. Recent work demonstrates that AI models have achieved results with high accuracy in AMD classification and diagnosis[92,93]. Consequently, creating a high-quality database remains a significant hurdle for complete implementation of AI in disease diagnosis.

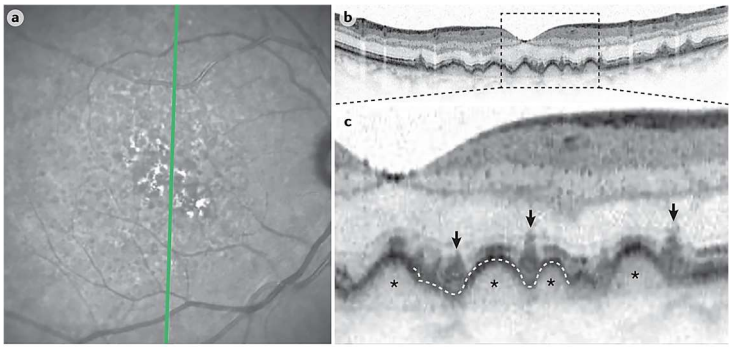

Figure 10. Subretinal drusenoid deposits. (a) An image in near-infrared reflectance indicating the position of the OCT scan (green line); (b) The corresponding OCT scan; (c) Enlarged OCT image. The indicated arrows point to the structures that correlate with subretinal drusenoid deposits, while the asterisks denote the structures typically associated with drusen. Pseudodrusen appear to be situated above a hyperreflective band whereas the drusen seem to be positioned beneath the same hyperreflective band (dashed line). Reticular pseudodrusen are suggested to be found in the subretinal space, explaining the term 'subretinal drusenoid deposits', based on the assumption that the hyperreflective band represents the RPE. Image taken from Fleckstein et al. 2021.

TREATMENTS

Since a definitive cure for both forms of advanced AMD remains elusive, primary emphasis lies on prevention or delay of disease progression from initial stages. This is mostly based on use of oral supplementation and specific nutrients. In one study, supplementing the diet with high doses of antioxidants and minerals, including Vitamin C (500 mg), Vitamin E (400 IU), beta-carotene (15 mg), zinc oxide (80 mg) and cupric acid (2 mg) effectively postponed the advancement of AMD, even in high risk patients[94]. Subsequent follow ups demonstrated that individuals with greatest omega-3 fatty acid consumption had a reduced susceptibility to GA. Due to concerns regarding a potential rise in lung cancer rates associated with carotenoid, it was substituted with a combination of lutein and zeaxathin[95]. This mixture, however, was found to have negligible effect, as determined in a later study[96]. In addition to supplements, it is crucial to address modifiable risk factors, with smoking cessation being of utmost importance. Management of AMD relies heavily on documentation, continuous monitoring, and

surveillance to promptly identify potential alterations in visual function.

Dry AMD

Currently, there is no approved treatment for dry AMD, and due to the intricate nature of GA, it's probable that targeting a single molecular pathway might not yield satisfactory results. Anti-inflammatory agents and complement inhibitors are currently being tested as therapeutics for AMD: no reduction of GA was detected using either Eculizumab (complement component 5 C5 inhibitor)[97], Lampalizumab (complement factor D inhibitor)[98], Sirolimus (immunosuppressive agent)[99] or Tedisolumab (complement component 5 C5 inhibitor), while Avacincaptad pegol (anti-C5 aptamer) and Pegcetacoplan (complement component 3 C3 inhibitor) administration showed a reduction in the rate of GA growth[100]. Another treatment is represented by gene therapy, which focuses on anti-complement and antiangiogenic proteins. A first study used subretinal injection of GT005 to regulate complement activation and membrane attack complex formation, showing complement-driven CNV remission in a mouse model of CNV[101]. RPE transplantation may be finally a valuable therapy to treat AMD, as demonstrated by a study showing an increased subretinal pigmentation adjacent to atrophic areas[102]. Additional approaches with encouraging results involve techniques aiming at visual cycle modulators[103,104], neuroprotective agents[105,106] and stem cell based transplantation[102,107].

Wet AMD

Although one of the noteworthy breakthroughs in the field of ophthalmology pertains to management of neovascular AMD, none of the treatments provide a complete cure or disease reversal. Introduction of anti-vascular endothelial growth factor (VEGF) agents has marked progress, where approximately 30% of patients who were previously almost certain to go blind now have a chance for improved visual acuity in the first two years of treatment. Numerous studies have also indicated a substantial reduction in central macular thickness and improvements in visual acuity. One of the initial studies demonstrated visual acuity enhancements through repeated intravitreal injections of Pegaptanib sodium, a VEGF165 inhibitor. However, Pegaptanib is no longer employed in neovascular AMD treatment due to its comparatively lower efficacy when compared to other available anti-VEGF drugs. Repeated intravitreal injections of Bevacizumab, a VEGF-A inhibitor, have been shown to enhance best-corrected visual acuity[108]. Similarly, repeated injections of Ranibizumab and Brolucizumab, which are also anti-VEGF-A agents, have resulted in improvements in mean best-corrected visual acuity [109–111]. While anti-VEGF therapies have become the standard for treating neovascular AMD, some individuals are non-responders (to initial loading dose) or tachyphylactic (show diminishing responses with successive injections)[112]. Additionally, the necessity for repeated anti-VEGF injections has adverse effects on patients' quality of life and treatment costs[113].

These drawbacks have prompted the search for viable alternatives, such as Faricimab, which has demonstrated effectiveness similar to Ranibizumab in terms of changes in best-corrected visual acuity, central macular thickness, and CNV[114]. More recently,

Abicipar pegol[115], has shown promising results in terms of durability when compared to Ranibizumab, with comparable effectiveness. A more comprehensive review of anti-VEGF treatments and potential treatments for AMD, can be found in Ricci et al.[116].

1.2 CURRENT RETINAL PROSTHESIS

Despite significant alteration of the neural retina in advanced stages of photoreceptor damage, morphologic studies show a moderate degree of preservation of inner retinal neurons, 70-80% of bipolar cells and 25-40% of ganglion cells[117]. This degree of preservation opens windows of opportunity for utilizing different stimulation strategies interfacing with the surviving, healthy inner retinal neurons. Various stimulation modalities in current research involve optogenetics, bioelectronics, ultrasonic stimulation, etc. Retinal prostheses generate light-induced signals in the retina, utilizing engineered devices to replace the photoreceptive function of the eye. Unlike gene therapy, retinal prosthetics are not genotype-specific and can be considered as potential solutions at later stages of the disease where cell replacement approaches become unfeasible. Optic nerve prostheses as well as intracranial devices stimulating cortical or thalamic visual pathways, represent another way of approaching these patients and they could be considered in place of retinal prostheses, for example, in case of glaucoma, a

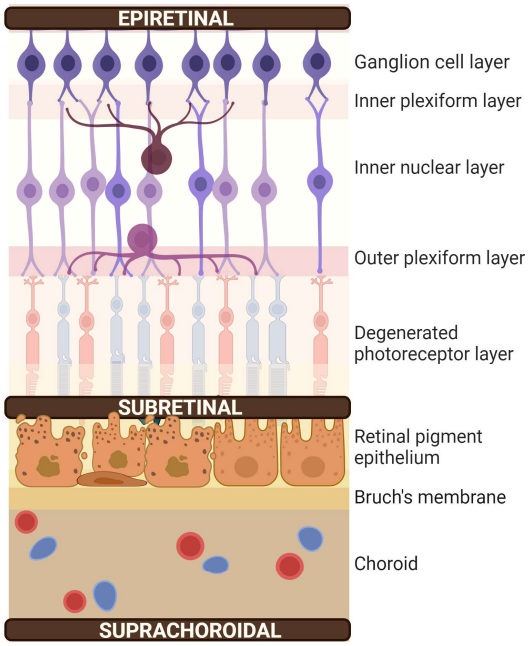

Figure 11. Different implant locations of retinal prosthetics. Retinal prostheses can be categorized according to their implant location: they can either be surgically implanted docking the retinal inner surface and stimulating retinal ganglion cells (Epiretinal), placed in between the degenerated photoreceptors and the retinal pigment epithelium (Subretinal) or finally anchored in between the choroid and the sclera (Suprachoroidal). Figure created with BioRender.

pathological process involving degeneration of inner retinal neurons. Although facing

many challenges, retinal prosthetics proved to be a suitable therapy for patients affected by late AMD or RP, recovering rudimental vision or visual percepts, a result hardly reached by any other technology so far at the clinical level.

Depending on the location of implantation of electrode array chips and device complexity, three distinct prosthesis systems have been studied (**Figure 11**).

1.2.1 EPIRETINAL PROSTHESES

Epiretinal prostheses are anchored to the innermost layer of the retina and serve in close proximity to the RGCs for direct stimulation. Surgical delivery of the device is usually transvitreal through a pars plana sclerotomy and a tack secures the microelectrode array to the retinal surface. From a surgical point of view, the epiretinal approach is easier to handle as the procedure is routinely practiced. It allows device placement in a large portion of visual field[118] and its vitreous proximity can aid heat dissipation[119]. From a functional standpoint, directly stimulating the retinal ganglion cells might not be ideal, as it circumvents the remaining intraretinal processing mechanism, limiting the ability to replicate the natural retinal topographical organization effectively. Furthermore, epiretinal proximity to axonal nerve fibres could cause unintended nerve excitation, hampering image resolution and obscuring the desired stimulation pattern. Retina anchorage can be problematic due to the copious usage of retina tacks, which may initially result in retinal damage and partially detach over time causing resolution loss[120]. To date, two epiretinal devices have been approved and brought to the U.S. (FDA) and European (CE) markets (Argus® II and IRISR® II), and two devices are still under clinical evaluation (EPI-RET3 and NR600).

ARGUS II®

The first retinal implant to gain regulatory approval, Argus (two generations, Argus I and II®) was developed by Second Sight Medical Products (CA, USA) and received CE and FDA approval in 2011 and 2013 respectively[121,122]. Up to 2018, it holds the record as the most extensively employed device globally, with over 300 implants performed. The system is comprised of two main components: an active implantable device and an external unit (**Figure 12**). The external unit contains a pair of glasses housing a small camera and a transmitter, along with a user-worn battery. The implantable portion consists of a receiving and transmitting coil, an electronic casing affixed to the sclera outside the eye, and a 60-channel electrode array (200 µm in size) array surgically placed in contact with the retina, fixed with a retinal tack. The electronics and the array are connected, through the pars plana, with a metallized polymer ribbon cable. The visual field is captured by the external camera and converted into electronic signals by the processor, which in turn sends them to the external transmitter coil on the glasses. The sent-out signals are then received by the internal coils and delivered, via the ribbon cable, to the electrode array, which emits electrical pulses to RGCs. External camera acquisition pixels (6 x 10) are mapped 1:1 onto the electrode array, resulting in a 20° field of view covering. The first studies saw 30 subjects, clinically evaluated up to 5 years after implantation with follow up measurements like fundus imaging, FA and OCT and functionally evaluated with full-

field light threshold stimuli, visual acuity, and real-world usefulness tests. Threshold testing revealed that all subjects perceived light when the implant was ON, 96% of subjects could localize high-contrast objects on a screen, 57% could discern motion direction and 23 could score on a grading visual acuity test (best result: 1.8 log MAR). After 5 years of implantation, 60% of patients (18/30) did not experience any device- or surgery-related serious adverse event (SAEs), the remaining 12 patients experienced 24 SAEs, always easily treatable with standard ophthalmic procedures[123].
Although, Second Sight halted the production in May 2019, National Institute of Health and Care Excellence assessment for Argus II® is still undergoing to ascertain the device benefits in terms of quality of life and daily activities of the patients.

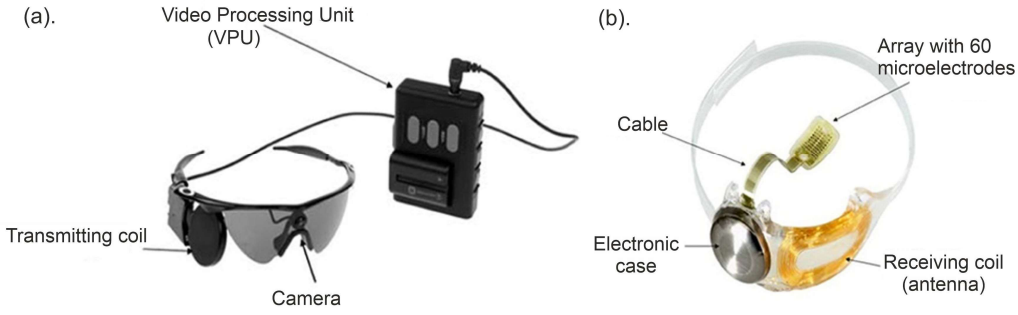

Figure 12. Argus II® Retinal Prosthesis System. (a) The external elements of the Argus II prosthesis system: glasses, portable video processing unit (VPU) and connecting cable. The glasses are equipped with a miniature video camera for image capture, and a coil for transmitting data and stimulation instructions to the implant. The VPU converts the video images into stimulation commands and is body-worn. The cable links the glasses to the VPU; (b) An image of the internal component including 6 x 10 channel array, an electronic case, and implanted radiofrequency coil. Images and description adapted from Second Sight Medical Products, Inc., Sylmar, CA.

IRIS II®

The basis for the development of Intelligent Retinal Implant System: IRIS II® (by Pixium Vision, SA, 2016) was the Intelligent Medical Implants (IMI) Learning Device[124,125]. It is composed of a 49-channel microelectrode array (250 µm size, 120 µm inter-electrode distance). Depicting a good safety profile and reasonable longevity, the device achieved good results with patient-reported phosphenes (19 out of 20 implants) and pattern perception during stimulation[126,127]. Pixium Vision S.A. acquired IMI in 2007 and made several enhancements which led to the birth of IRIS II®[128,129]. Similar to the ARGUS II®, the IRIS II® also consists of a glasses-like visual interface that communicates with the internal stimulation components. However, there exist notable distinctions between the two systems. The system comprises both an implantable and an external component (**Figure 13**). The implantable section consists of an intraocular front-end array of 150 microelectrodes, along with an extraocular receiver. Meanwhile, the external portion includes a visual interface mounted on glasses. This interface communicates with a pocket processor, which, in turn, connects to the extraocular receiver. As a substantial difference from ARGUS II®, IRIS II® employs a neuromorphic image sensor that is

designed to mimic the biological architecture of retina and generate a data format with temporal resolution akin to retinal processing, whilst continuously responding to visual inputs. The neuromorphic image sensor also imitates the retina's ability to suppress redundant information and can segregate sustained and transient components of visual input. Another difference from Argus II® is that the commands to the retinal stimulator are transmitted optically via an infrared array, and not by means of radio frequency. Utilizing fast optical transmission (Near Infra-Red) enhances data transfer rates and reduces implant size. The increased data transfer rates allow for better control of a larger number of electrodes (150 vs 60 of ARGUS II®) at higher refresh rates. Finally, the most unique and technologically advanced feature of the IRIS II® is its ability to integrate a learning retinal encoder that can distinguish excitatory and inhibitory pathways, mimicking ON/OFF pathways through multiple iterations (up to 100)[128]. In 2016, ten subjects with visual acuity of 2.3 logMAR or worse were implanted with this system. After one year of implantation, four subjects reported SAEs. Nonetheless, the visual tests yielded promising results: subjects showed improved viewing distances in square recognition tests (with an average reduction of 6.25 cm), enhanced motion perception, and wider visual field area[130]. The incidence of severe adverse effects was notably lower compared to the ARGUS II®. However, due to the device's shorter than expected lifespan, additional clinical trials were postponed, allowing device refinement.

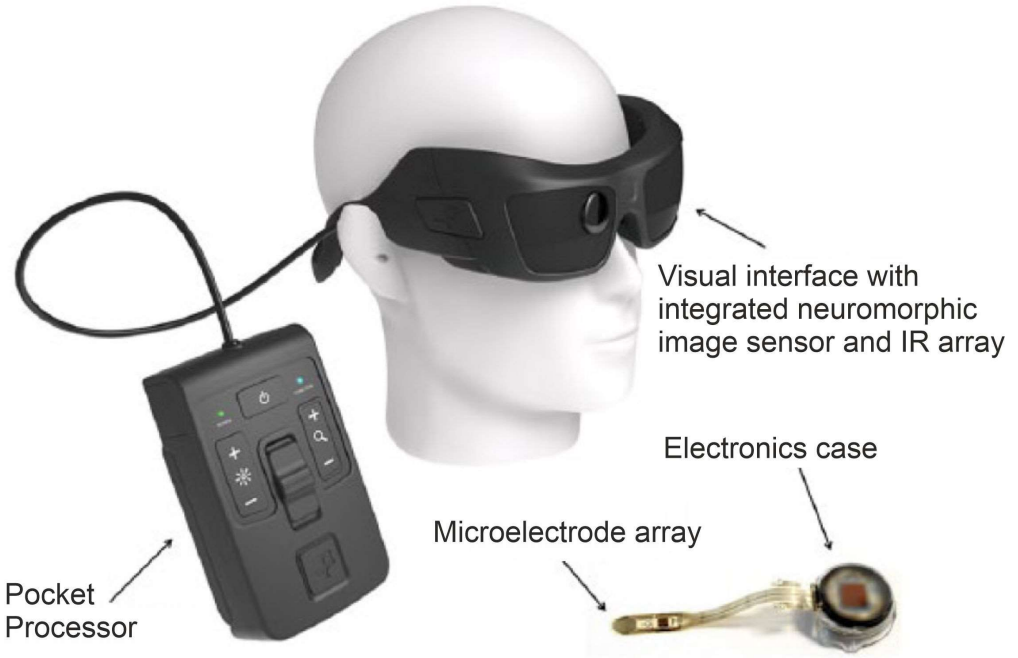

Figure 13. Intelligent Retinal Implant System (IRIS) II®. The external component of the IRIS II system consists of a glass-mounted camera, and the signal is processed by a pocket processor that subsequently transmits it to the extraocular implanted component (electronic case) to stimulate the ultimate target using a 150-channel microelectrode array. Image taken from Pixium Vision S.A., Paris, France.

EPI-RET3

EPI-RET3 (Philipps-University Marburg, Germany) is an epiretinal device that positions all its internal components entirely within the eye, eliminating the need for a trans-scleral connection. The device comprises two intraocular components: a microelectrode array with a variable number of 3D electrodes (height, 25 µm; diameter, 100 µm) and a receiving coil[131]. Similarly to ARGUS II® and IRIS II®, an external camera and visual processor are necessary for transmitting information to the internal coil. The device possesses bidirectional functionality, enabling both the stimulation and recording of retinal ganglion cells. This capability allows the device to learn and adapt its stimulation algorithms to better mimic natural retinal responses. During a 4-week trial, six subjects were implanted with a 25-channel EPI-RET3 device. All subjects reported perceiving phosphenes at low threshold stimulations, although the description of this perception varied among patients. Only one subject reported SAEs[132].

VLARS

Building on the EPI-RET3 design, the VLARS (Very Large Electrode Arrays for epiRetinal Stimulation) device represents an advancement of its predecessor[133]. It features a larger stimulator area (110 mm²) capable of accommodating up to 250 microelectrodes, which ensures a broader visual angle (up to 37.6 degrees). Positive outcomes were observed in animal studies (in pigs and rabbits) involving VLARS implants, prompting the authors to consider the device's potential entry into the clinical phase[134].

OPTOEPIRET

Following the path of EPI-RET3, another prototype called OPTOEPIRET emerged[118]. This prototype represents a significant advancement compared to its predecessors, as it eliminates the requirement for an external camera. Within the implantable component, photosensors are integrated, capable of capturing the visual field that is projected and focused by the physiological optics of the eye. This captured image is instantly translated into electrical stimulation patterns on the retina (**Figure 14**). The images are captured by

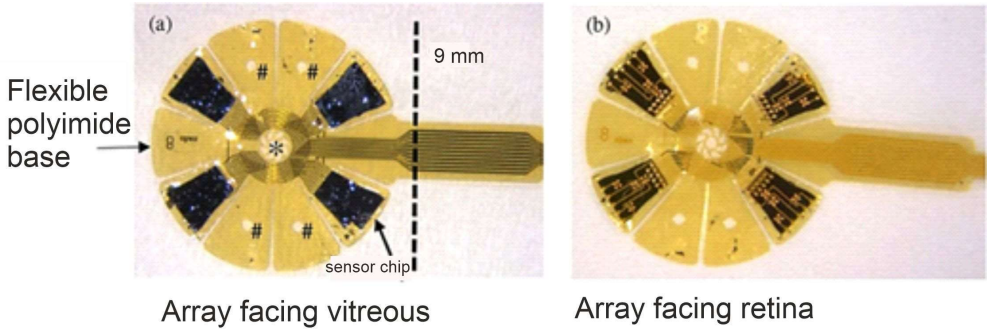

Figure 14. OPTOEPIRET Array. (a) Vitreous facing side of the 9 mm diameter array featuring a central aperture for retinal tacks (indicated by an asterisk) and peripheral aperture for retinal tacks (marked with number signs); (b) Retinal facing side of the array. Image taken from Schaffrath et al. 2021.

photosensors positioned on the chip's backside. An Integrated Circuit (IC) is responsible for generating signals, which are then transmitted to the front side for stimulating retinal ganglion cells[135]. This technology holds the potential for high-resolution prosthetics if each photodiode were to be linked to a stimulation electrode. Currently, the device's compatibility has been verified through *in vitro* and *in vivo* assessments, although the feasibility of surgical implementation is still under development.

NANORETINA

Nano Retina is a startup enterprise that has introduced a novel concept in epiretinal prosthetics (Nano Retina, Israel). The system is composed of an implanted component and a pair of glasses worn by the patient. These glasses serve as a power source for the implanted chip, utilizing infra-red laser light for transmission. Similar to OPTO-EPIRET, this prosthetic design eliminates the need for an external camera and exploits the eye's natural optics to project the image onto an array of photosensors. These photosensors, in turn, manage the conversion of the electrical signal to the stimulation front end. The stimulation front end comprises an array of hundreds of 3D microelectrodes positioned on the ganglion cell layer. The unique three-dimensional configuration of the electrodes enables penetration into the tissue down to the inner plexiform layer, where healthy cells can be stimulated (**Figure 15**). Notably, Nano Retina does not circumvent the processing of the still-functioning retinal cells. This approach ensures a higher level of bio-mimesis, which subsequently leads to greater restoration of visual acuity. Following successful testing on the eyes of chickens and domestic pigs by demonstrating encouraging outcomes in evoking visual perceptions[136,137], the device is currently undergoing clinical trials.

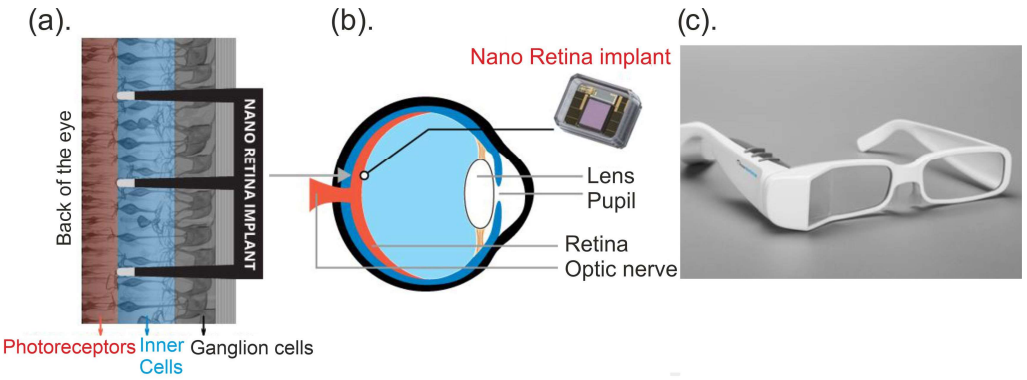

Figure 15. NANO RETINA. (a) Nano Retina implant is positioned within the retina using three-dimensional penetrating Ni electrodes that extend to the outer plexiform layer, even though the device is implanted epiretinally; (b) The placement of the Nano Retina implant within the eye; (c) The external component of the Nano Retina system represented by rechargeable eyeglasses, serving as both a wireless power source and a system for transmitting signals to the implanted part. Image adapted from Nano Retina website.

1.2.2 SUBRETINAL PROSTHESES

The subretinal prosthesis are implanted physically closest to damaged photoreceptors, between the photoreceptor layer and RPE. They do not require the use of additional retinal tacks and provide improved mechanical stability. The device directly contacts and stimulates the remaining inner nuclear layer exploiting interneurons processing machinery and thus potentially conferring higher visual acuity, more physiological perception, and less demand for image processing. In addition, given the use of the natural retina amplification cascade, the device needs lower stimulation intensities. However, the surgical processes required for the implantation of such devices are more intricate due to the inherent adhesion between the retina and RPE. The primary constraint of subretinal implants is the restricted area available at the implantation location, which prevents the creation of sizable devices to avoid the risk of retinal detachment. Consequently, typically only moderate visual angles can be restored, rendering the device inapplicable to completely blind individuals (e.g., those with retinitis pigmentosa).

The Boston Retinal Implant Project (BRIP) was one of the first subretinal prostheses to be tested in clinical trials on human subjects and its design is quite similar to that of ARGUS II®, except for the implantation site. In the early 90s, Artificial Silicon Retina (ASR, Optobionics) was designed, featuring embedded photovoltaic devices coupled to electrodes. Following this, Aplha IMS and its successor Alpha AMS received the CE mark and more recently, PRIMA (Pixium Vision S.A) is currently undergoing clinical evaluation.

BOSTON RETINA IMPLANT (BRIP)

The initial version of the subretinal device aimed to ensure both the chip's biocompatibility and functionality. It included an external video capture unit, which could transmit image data to the implanted component through a transmitter. The stimulation front-end contained 15 electrodes with a diameter of 400 µm. Initial studies were conducted on Yucatan micropigs to establish surgical implant procedures and

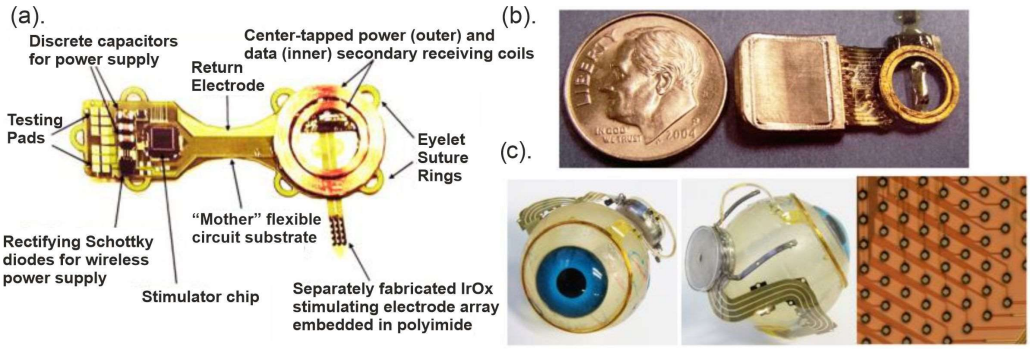

Figure 16. Three generations of the Boston Retinal Prosthesis featuring microfabricated elements. (a) First generation 16-channel stimulator with early micro-fabricated electrode array; (b) Second-generation hermetically packaged 16-channel device with bidirectional telemetry; (c) Third generation hermetically packaged 256 or more channels, demonstrated in a minipig, where the electrode array has a maximum width of 5 mm and features segmented leads, while the package measures 11 mm in diameter. Image adapted from Shire et al. 2020.

assess biocompatibility. Unfortunately, when the device was activated, no functional cortical responses were observed[138]. A second-generation device addressed some of the issues encountered with the first version, primarily related to both electrical and surgical constraints[139]. Subsequent iterations of the device focused on expanding the number of electrodes (up to 256, **Figure 16**) to more closely restore a physiological level of visual function in potential human recipients[140]. The Boston Retinal Implant Project is presently subjecting the new device to animal testing, as mandated by the FDA, and anticipates moving forward with phase I clinical trials in the near future.

ARTIFICIAL SILICON RETINA (ASR)

The ASR, developed by Optobionics, USA, was a trailblazer in the creation of a passive prosthesis that utilized wireless retinal stimulation via ambient light. The implanted chip comprised a photodiode array with 5000 channels (width 2 mm; thickness, 25 µm), coupled with an array containing an equivalent number of electrodes (9 µm wide, **Figure 17**). In an initial pilot study, 4 out of 6 implanted patients reported perceiving phosphenes upon exposure to light stimulation. This was accompanied by improvements in visual acuity, potential enhancements in color vision, contrast sensitivity, and an expanded visual field[141]. However, these effects were not attributed directly to the possible phosphene effect generated by the ASR. Instead, they were thought to be a result of a neurotrophic influence brought about by the action of neuroprotective growth factors[142,143]. Despite playing a pioneering role in advancing the field of photovoltaic prosthetic systems, the company eventually ceased operations due to concerns regarding whether sufficient stimulation currents could be achieved solely through the use of light[144].

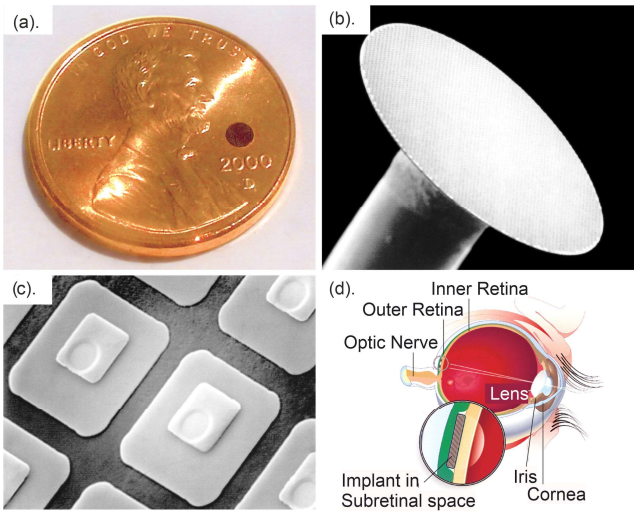

Figure 17. Artificial Silicon Retina. (a) A size comparison between the ASR system (black circle) and a penny; (b) The complete ASR microchip, (original magnification x 36) 2 mm in diameter, 25 µm thick; (c) Magnification of the ASR chip which implemented 5000 micro photodiodes (20 x 20 µm square, 5 µm interdiode distance); (d) Subretinal positioning of the implanted ASR chip. Image taken from Chow et al. 2004.

ALPHA IMS AND AMS

Alpha IMS (Retina Implant AG, Germany) was the first to obtain the CE certification in 2013. The implantable chip (3 mm^2 size, covering 11° of visual angle) achieves phototransduction utilizing a multi-photodiode array comprised of 1500 distinct photodiode-amplifier-electrode units. The amplifier necessitates external power, which is delivered through a cable originating from a subdermal coil affixed to the cranial bone behind the ear, passing subcutaneously. A removable external coil, magnetically attached to the subdermal one, facilitates power transmission via electromagnetic induction[145,146]. Moreover, the power supply can be manually adjusted using a handheld unit to manage image contrast and brightness[146]. The coil anchored to the bone, the connecting cable, and the subretinal implant demand coordination between different surgical teams, resulting in longer operative periods. This procedure is indeed invasive and demands specialized technical proficiency, leading to higher instances of device repositioning, subsequent replacement surgeries, and device malfunctions.

Clinical trials were carried out from 2010 to 2014, aimed at characterizing visual acuity, daily living and mobility and object recognition improvement. Daily living and motion enhancement was experienced by 21% of the subjects, as well as motion detection (up to 35° per second). All subjects improved object recognition up to 3 months from the

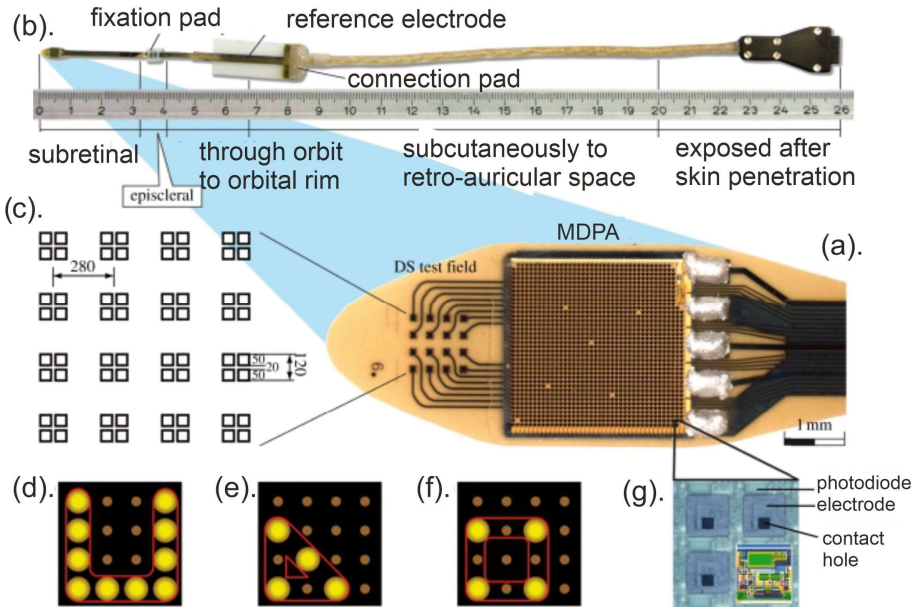

Figure 18. Alpha AMS. (a) The micro-photodiode array (MPDA) is a light-sensitive CMOS-chip measuring 3.0 × 3.1 mm^2 CMOS-chip with 1500 pixel-generating elements, mounted on a 20 µm thick polyimide foil. This sheet also holds an additional test field equipped with 16 electrodes for direct electrical stimulation (DS test field); (b) The foil is affixed to the sclera using a small fixation pad; (c) Magnification of the DS electrode array displaying the 16 quadruple electrodes and their dimensions; (d) Pattern stimulation conducted through the DS array (e.g. forming the letter "U"); (e,f) Shifting the stimulation from a triangle to a square by altering a single electrode; (g) Magnification of four of the 1500 elements ('pixels'), demonstrating the rectangular photodiodes above each squared electrode and their associated contact holes linking them to the amplifier circuit (overlaid sketch). Image taken from Zrenner et al. 2011.

implant, 86% reporting light perception and a maximum visual acuity of 1.44 logMAR[145] (standardize Landolt C-Rings). Only two SAEs (out of 75 AEs) have been reported in 1-year of implantation, thus qualifying the device as safe[147,148].

The second-generation device, named Alpha AMS, was granted CE approval in 2016 and retains the same phototransduction mechanism as its forerunner[149] **(Figure 18).** The device featured a larger chip size (3.2 x 4 mm² compared to the previous 3.2 x 3.1 mm²) and an increased number of photodiode-to-electrode pairings (1600 versus the previous 1500; with diameters of 30 µm versus 50 µm squares). While the device's functional outcomes were reportedly similar to those of its predecessor, the authors asserted that the new device had improved durability[148], attributed to alterations in the foil substrate and silicon cable materials.

PHOTOVOLTAIC RETINAL IMPLANT (PRIMA)

Following the creation of the IRIS II®, Pixium Vision S.A. shifted its attention to developing another device that is presently undergoing assessments of safety and performance feasibility in both Europe and the USA. The PRIMA bionic vision system introduces an innovative approach to photovoltaic stimulation. While being tested for dry AMD, there are plans to extend studies to patients with RP. The 3 mm implantable chip[150] has hexagonal shape and embeds 142 pixels (70 µm) which receive pulsed near infra-red (880 nm) light from a pair of external glasses **(Figure 19).** The entering near infra-red light is conveyed to a system of photodiodes and electrodes which, at the final stage, stimulate the contacted retinal tissue. The system does not depend on external

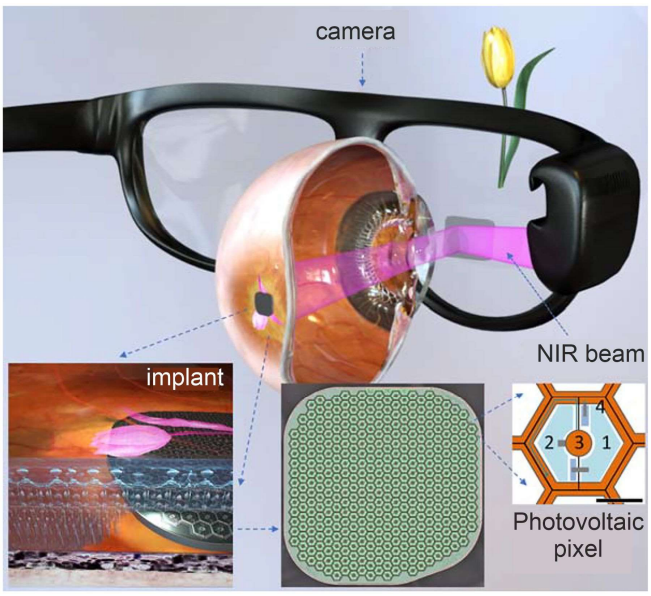

Figure 19. Photovoltaic Retinal Implant. Top view: a schematic displaying the system setup consisting of the photovoltaic retinal prosthesis (implanted component) and the external augmented reality-style video glasses (external component). These glasses project the image onto the retina by employing pulsed near-infrared light. The light is converted into current pulses by photodiodes, which subsequently activate the retinal neurons. Each pixel comprises two diodes (1 and 2), connected in series between the active (3) and return (4) electrodes. Scale bar = 50 µm. Image taken from Palanker et al. 2020.

power sources and requires no trans-scleral wires, which makes it more surgically manageable. Preclinical results in RCS rats demonstrated 100% contrast visual evoked potential waveforms. The parameters of these waveforms were comparable to those of wild-type rats, exhibiting amplitude and latency that could be adjusted according to light intensity[151]. From 2017 to 2018, the PRIMA device was surgically implanted in five patients with dry AMD, all of whom had visual acuity at or worse than 1.3 logMAR. All five patients experienced phosphenes perception through supra-threshold-frequency stimulation and reported persistent perceptions when the frequency was increased. In object orientation tests (using 2 alternative-force-choice method with horizontal and vertical bars), only one of the five subjects failed, while the remaining four subjects, reached visual acuity values from 1.37 to 1.6 logMAR (with the logMAR limit set at 1.32 by the pixel size)[152]. All restored functions demonstrated improvement at the 24-month mark[153], reflecting both the accurate functioning of the device and its safety and stability. One patient's visual acuity improved from 1.6 logMAR to 1.34 logMAR, approaching the visual acuity limit determined by the pixel size. The authors speculate that advancements in photovoltaic technology, leading to the availability of smaller pixels[154,155], could potentially achieve visual acuity values as low as 0.7 logMAR, or even null logMAR with the assistance of glasses' zoom function.

1.2.3 SUPRACHOROIDAL PROSTHESES

A third type of a more recent prosthesis is the suprachoroidal prosthesis, where the electrode implantation is between choroid and sclera: Semichronic suprachoroid transcleral prosthesis or alternatively, in the scleral sac: Bionic Vision Technology. This approach brings together the structural reliability seen in subretinal devices[156,157] with a substantial capacity for heat dissipation and sufficient room for the implantation of an epiretinal prosthesis[158]. Surgical implant of the device warrants reduced risk of retinal damage since no trans-vitreal access is required[159]. Nevertheless, some preclinical and clinical studies report subretinal and suprachoroidal hemorrhage risks[157,158,160]. A significant challenge with suprachoroidal devices is their distance from the intended stimulation site: bipolar cells. This makes selective stimulation challenging, resulting in poor spatial resolution[161,162]. Furthermore, the large current doses required to achieve stimulation might lead to the risk of causing damage due to overstimulation[154,163].

BIONIC VISION AUSTRALIA (BVA)

The BVA team was among the first groups to successfully advance this type of device to human trial stages. The first-generation device consisted of a 20-channel system (20 stimulating electrodes: 17 x 600 µm and 3 x 400 µm, in addition to 17 x 600 µm returning electrodes and 2 large returning electrodes), with a head-mounted external camera and an image processor which fed the implantable stimulation electrodes. The first pilot in-human study started in 2012 with a 2-year implant in 3 patients with advanced stage RP[158]. The complicated and faulty nature of the surgical procedure led to the development of combined subretinal and suprachoroidal hemorrhages in all patients, post operation. Conversely, phosphene perception could be triggered in all patients[164], but only 2 of them reported it to be controllable and retinotopically

locatable[161]. However, these responses exhibited variable characteristics and stimulation thresholds: while all three patients achieved light perception, only one of them successfully completed the visual acuity task, with significant improvements if compared with the device "off" (logMAR = 2.62). All the subjects were able to recognize characters and localize static objects, but only one was able to perceive dynamic motion[162]. After 2 years, upon device explantation, fibrous capsules were found around the implant in all three subjects, indicating poor device biocompatibility[165]. Given the issues encountered with the first-generation system, the BVA group directed their efforts towards creating two new devices: a fully implantable 44-channel system[160] and another device called the Phoenix-99, equipped with 99 stimulation electrodes, in an attempt to address the challenge of low spatial resolution[157]. The 44-channel system (**Figure 20**) was designed for at-home usage due to its complete implantability. It was successfully implanted in four subjects over a 56-week study period. This device consists of (i) 44 platinum electrodes (diameter 1 mm), covering an approximate visual field of 38 x 28°; (ii) 2 larger returning electrodes (diameter 2 mm). Each stimulator connects with 22 electrodes and captures the external visual scene through an external CMOS-based video camera. The video data is then processed by a video processor, which aims to enhance contrast[166]. All four subjects underwent implantation without any surgical complications, except for minor subretinal hemorrhages experienced by two patients. None of the participants encountered serious adverse events during the study. All subjects reported experiencing visual percept's, with peripheral phosphenes extending up to 25° from the fovea. In a square localization task, subjects demonstrated greater accuracy when the device was active, and they were also capable of differentiating object sizes in a tabletop task. Half of the participants achieved visual acuity values of up to 0.033 cycles/degree and exhibited improved performance in screen-based motion discrimination tasks. The Phoenix-99 device features an array measuring 18.7 x 10.8 mm² and is equipped with 98 platinum electrodes. It utilizes an internal-external transmission system similar to the 44-electrode version. Nine systems were implanted in sheep for up to 100 days as part of a feasibility assessment study, focusing on surgical practicality. This assessment resulted in the determination of device tolerability. Only three SAE were reported, along with no major adverse events. Mild cellular responses were observed in the suprachoroidal space, indicating the device's biocompatibility.

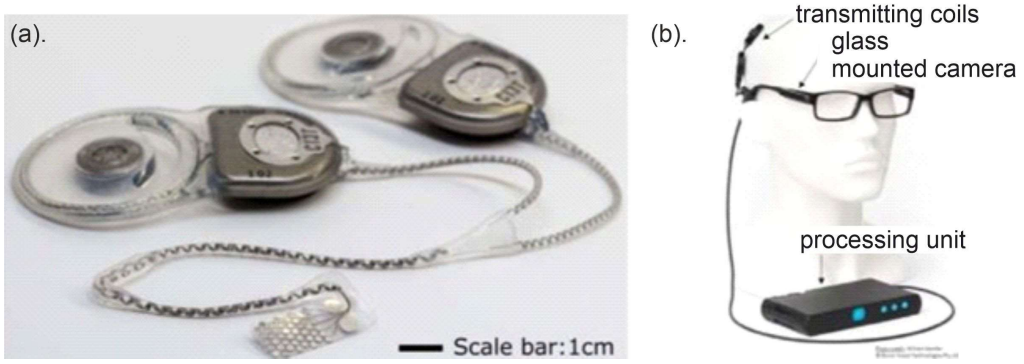

Figure 20. Bionic Vision Australia device (2nd generation). (a) An implantable ocular electrode array equipped with two stimulators; (b) The external parts of the BVA system incorporate a CMOS video camera mounted on glasses, head-worn transmission coils that use magnetic coupling and a pocket-sized video processor. Image taken from Petoe et al. 2021.

SUPRACHOROIDAL-TRANSRETINAL STIMULATION (STS)

The STS system was developed by Artificial Vision Project (Osaka University, Japan) and its first 9-electrode prototype[167] evolved in the second-generation device which embedded 49 protruding electrodes[168] (size, 5.7 x 4.6 mm^2; protrusion, 0.3 mm), controlled by an implanted coil receiving signals from an external component connected to a camera **(Figure 21).** Three individuals diagnosed with advanced RP underwent implantation of the second-generation device and no SAEs were documented within the 1 year of implantation[156]. Although all subjects experienced elicited phosphenes perception, no reproducibility was found in outcomes of functional assessment as compared to those conducted with the initial prototype. Only one subject managed to accurately localize squares at different time points, while two subjects demonstrated the ability to navigate along a white line and recognize common objects in daily life scenarios. In a separate study involving a patient afflicted with Stargardt disease, the device exhibited the potential to enhance visual performance when used during binocular vision[169]. A larger participant pool is required to derive even primary conclusions about the effectiveness of suprachoroidal stimulation and its potential advantages compared to the two methods discussed in earlier sections. However, the outcomes observed thus far imply that this approach presents more constraints than both epiretinal and subretinal prosthetic techniques.

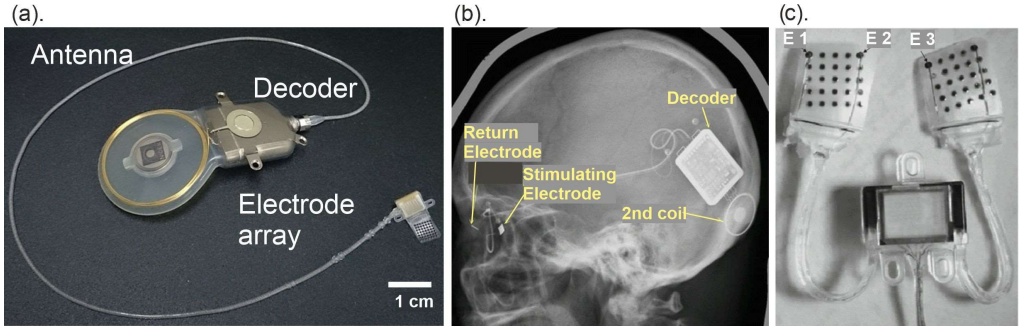

Figure 21. Suprachoroidal-Transretinal Stimulation device from Osaka University. (a) The components which are surgically implanted within the STS system; (b) A lateral X-ray projection taken after implantation; (c). A closer view of the 49-channel stimulating electrode array. Image courtesy Fujikado et al. 2016.

1.2.4 ORGANIC RETINAL PROSTHESES

Inorganic photovoltaic devices suffer from various disadvantages such as complex and expensive fabrication, poor flexibility, localized heat generation, low conformability, low spatial resolution, and restricted retinal coverage. Alternatives such as organic and biomimetic photovoltaic systems could potentially overcome some of these drawbacks.

Organic conjugated polymers (OCPs) are biocompatible, conformable, and softer than conventional electronic materials like metals and silicon. They can be easily integrated onto substrates with the same characteristics (i.e., silk fibroin scaffolds) leading to minimally invasive implants[170,171]. The mechanical compliance with soft-, non-planar- and moving-living tissues can be further enhanced by the formulation of OCP-based

hydrogels, stretchable materials and nanoparticles. OCPs can also be engineered to be biodegradable, leading to temporary implants that do not require surgical removal. OCPs form stable and oxide-free interfaces with aqueous electrolytes, capable of establishing direct contact with the biological milieu. In addition, they have a mixed ionic-electronic conductivity bridging the gap between ionic currents, typical of biological systems, and electronic currents, typical of the available electronic instrumentation. OCPs can be processed from solution, in mild conditions and at low temperatures. This allows for low-cost, low- environmental-impact processes that are compatible with biomolecules and sensitive substrates.

Most importantly, OCPs showcase optoelectronic properties which makes their incorporation a central idea in the new age organic bioelectronics. Owing to their ability to delocalize π-electrons which imparts them with semi-conducting properties, conjugated polymers offer potential for tunable optical properties. Upon light exposure, excitons are formed within photosensitive conjugated polymers, consisting of a bound state between an electron (e^-) and a virtual positive charge (h^+). In the presence of a driving force like an electric field, these excitons can be separated to generate a current. This electric field can be established through an external bias or by forming a heterojunction between an electron-donor and an electron-acceptor compound, which exploits favorable energy band alignment to enable charge separation. A local voltage drop occurs at the heterojunction due to the difference between the lowest unoccupied molecular orbitals (LUMO) and the highest occupied molecular orbitals (HOMO) energies

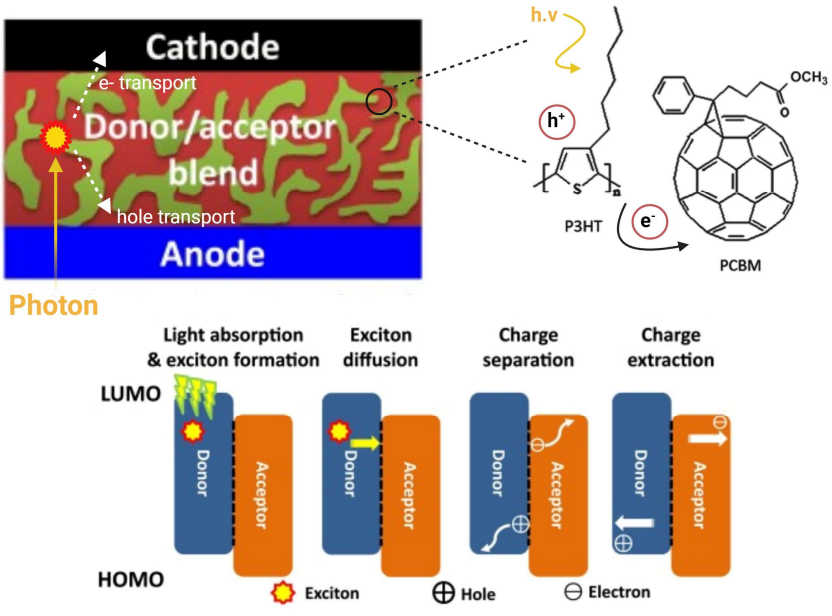

Figure 22. The operational mechanisms of organic solar cells (OSCs). Top: Device structure of bulk heterojunction OSCs. Electron donor (P3HT) and acceptor (PCBM) are blended to optimize the interface for effective exciton dissociation into electrons and holes. Bottom: The working mechanism through which OSCs operate. Abbreviations: HOMO, highest occupied molecular orbital; LUMO, lowest unoccupied molecular orbital. Molecular orbital; LUMO, lowest unoccupied molecular orbital.

of the donor and acceptor materials respectively. This voltage drop generates a driving force for the e^--h^+ pair dissociation. A strategic design of the energetic structure of the utilized materials facilitates the desired charge separation and collection, resulting in the creation of a "photo potential" between the cathode and anode (**Figure 22**).

Poly(3-hexylthiophene) (P3HT) is the most utilized conjugated polymer in both photovoltaics and vision restoration. It is employed either alone or combined with phenyl-C61-butyric-acid-methyl-ester (PCBM) or poly(3,4-ethylenedioxythiophene)-poly(styrenesulfonate) (PEDOT: PSS). P3HT's absorbance spectrum peak around 530 nm closely matches the wavelength sensitivity of green cones in primates. Various approaches involving P3HT have been explored, such as film-based devices or nanoparticle-based configurations, all demonstrating promising outcomes in preclinical trials. Globally, two primary research groups are testing such devices: one at IIT Italy and another at EPFL Switzerland.

A FULLY ORGANIC PLANAR PROSTHESIS

A novel class of fully organic, biocompatible, and functionally autonomous photovoltaic prosthesis was developed by the researchers at IIT (Genova and Milan) Italy. The device included a top layer of semiconductive P3HT, a middle layer of conductive PEDOT:PSS, and a passive substrate layer made of silk fibroin (average thickness of 30 µm). Characterization of biophysical and surface properties was carried out, in addition to long term biocompatibility[172] studies. For the purpose of visual studies, various genetic rodent models, which mimic retinal alterations seen in RP in humans, are employed. The rd1 and rd10 mice, along with the RCS rat model, are among the most frequently utilized. In RCS rats, a recessive mutation in the Mertk gene (receptor tyrosine kinase) results in impaired phagocytosis of photoreceptor outer segments by RPE cells. This dysfunction ultimately leads to the death of both rods and cones[173]. Due to the larger size of the eyes, RCS rats, unlike rd1 and rd10 strains, constitute a model that can more easily be handled from a surgical point of view, especially to access the subretinal region. Consequently, our research group chose the RCS rat in our investigations, specifically the pink-eyed strain, known for its faster degeneration compared to pigmented animals.

The device was implanted in the subretinal space of 2-3-month-old RCS rats and was found to achieve a retinal coverage of about 10-15%[174]. Restoration of light sensitivity was assessed by pupillary light reflex at 30 DPI. When comparing the age-matched implanted RCS rats with healthy RCS-rdy$^+$/Lav rats and non-implanted dystrophic RCS rats used as controls, the implanted RCS rats showed a pupillary response that closely resembled the response of healthy controls within a range of 3 to 10 lux luminance. Analysis of visual evoked potentials (VEPs) was used to assess the extent of visual acuity improvement facilitated by the device, using patterned visual stimuli with different spatial frequencies. The implanted animals demonstrated a notable two-fold increase in acuity at 30 DPI when compared to both non-implanted and sham-implanted animals. This improvement was sustained at the 180-DPI mark. Moreover, the results from the light-dark test indicate that the amount of time spent in the dark area was notably greater for the implanted animals compared to both non-implanted and sham-implanted animals at both the 30 and 180-DPI marks, suggesting that the organic P3HT-based device improved their ability to perceive light. This work represents the first long-

term utilization of a fully organic two-dimensional interface for neuronal photo-stimulation *in vivo* and paved the way for the development of a 3D prototype (described in section 1.4.1).

POLYRETINA

Polyretina (EPFL, Lausanne, Switzerland) is a foldable retinal prosthesis made of an array of photovoltaic pixels embedded into a polydimethylsiloxane (PDMS) matrix in the form

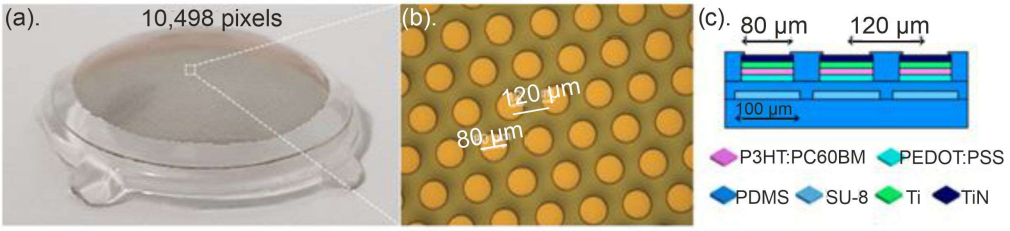

Figure 23. High-density POLYRETINA device. (a) Image of the high-density POLYRETINA prosthesis featuring 10,498 photovoltaic pixels; (b) Enlarged view of the photovoltaic pixels, each with a diameter of 80 µm and a spaced pitch of 120 µm; (c) Schematic representation of the cross-sectional structure of the POLYRETINA photovoltaic interface. Image adapted from Chenais et al. 2021.

of an implantable epiretinal lens. It adapts to the natural curvature of the eye and has the following distinct features: (i) in contrast to a uniform layer of photovoltaic-stimulating polymer, the first generation device comprises 2215 individual stimulating channels (diameter, 80 or 130 µm) distributed across a 12.7 mm area; (ii) the semiconductor layer of P3HT:PCBM is enclosed by a bottom anode made of PEDOT:PSS (Poly(3,4-ethylenedioxythiophene) polystyrene sulfonate) and an additional upper cathode constructed from Titanium, akin to a conventional solar cell. Notably, Titanium, aside from its mechanical and electrochemical stability, functions as a capacitive charge-injection material[175]. In contrast to alternative epiretinal devices, the POLYRETINA effectively achieves a wider visual field coverage (extending to 46.3 degrees) and potentially enhances visual acuity through an increased number of stimulating pixels, which correspond to an estimated acuity of 20/600 or 1 cycle per degree. To assess and validate the *ex vivo* efficacy of the device, experiments were conducted on rd10 mouse retinas and activity elicited by RGCs was studied. Different responses could be detected, indicating either direct or indirect (internal retinal circuit mediated) RGCs activation. The second-generation system[176] embedded 10,498 photovoltaic pixels (diameter, 80 µm; pitch, 120 µm) for a total active area of 13 mm in diameter, thus being more spatially resolved than its predecessor (**Figure 23**). The device was again tested on rd10 mice retinal explants for device mediated RGCs activity. Spatial resolution of the stimulation was assessed by observing RGCs responses to a grating pattern reversal protocol with bar widths down to 70 µm. This pattern encompassed both the prompt responses of inner retinal cells with short latency and the extended responses originating from the body and axons of RGCs. POLYRETINA also validated its third-generation device[177] in *vivo,* in a model of chemically induced blindness in Göttingen minipigs, a reliable animal model resembling the human eye size and fovea[178,179]. In the revised device, a new conductive layer was integrated, involving a mixture of P3HT:PC60BM instead of P3HT:PCBM, which enhanced mechanical durability. The *in vivo* assessment of the

device's functionality demonstrated restoration of light-evoked cortical responses at safe irradiance levels[177].

1.3 LIMITATIONS AND FUTURE CHALLENGES

During the last quarter century, the field of retinal prosthetics has witnessed remarkable innovation and advancement by enabling artificial vision in several visually impaired patients affected by RP, AMD, glaucoma etc. The ongoing advancements are fuelled by progression in image processing algorithms and optical data transmission speeds, coupled with developments in microelectronics and material fabrication. However, no single approach has exhibited a superior advantage over the others and several limitations in artificial vision remain to be addressed.

Quantitative challenges

1. Visual field size: Many studies show that incomplete recovery of visual field strongly impacts everyday life negatively[180] and a large visual field is necessary to ensure the practical utility of artificial vision[181]. Experiments conducted with simulated prosthetic vision have determined that a visual angle ranging from 30° to 35° is the essential minimum for enabling mobility and performing everyday tasks[181,182]. In retinal prosthetics, visual field enlargement can be obtained by increasing the electrodes' active area upon the retina. Although possible with epiretinal and suprachoroidal implants, this is a potential issue with subretinal implants. Given the same electrode density and thus the same stimulation resolution, the larger the covered area, the greater the number of electrodes and the bulkier the trans-scleral cables needed to transmit the signal. This results in a trickier and riskier surgery[117], in addition to poor visual resolution[133]. A strategy to address this issue is to use the wireless photovoltaic approach[152,153,174–177,183–187] which circumvents the need of a trans-scleral cable, thereby alleviating limitations on electrode number and density. It also avoids potential post-operative issues like ocular inflammation or incision leakage.

2. Spatial resolution: The currently available retinal prostheses do not provide high resolution to enable object identification and recognition. Although the subretinal approach is potentially able to restore higher visual acuity than the epiretinal one e.g., PRIMA (20/460 in AMD patients)[152], Alpha-AMS (20/546 in RP patients)[146] v/s ARGUS II® (20/1260)[123], it is not able to return the appropriate visual acuity needed thus far. The low spatial resolution of epiretinal devices is attributed to their stimulation location, which can activate nerve fiber bundle paths and generate distorted phosphenes[188–190]. A potential solution is to selectively activate individual RGCs, which can promote one to one connection with electrodes[191]. Subsequently, different RGC types can be differentiated by employing a high stimulation frequency[192]. Another possibility is to modulate pulse stimulation parameters which can aid in a network mediated response[193,194]. Reducing the electrode size could provide a high-density pattern of very small stimulation channels, however, electrodes placed in proximity might heighten the risk of crosstalk, and reducing electrode diameter does not necessarily equate to improved resolution[195]. Retinal prostheses could benefit from current steering

approaches such as bipolar stimulation[196,197] that could overcome the abovementioned challenges by selective and/or sequential activation[198,199] of electrodes.

3. Temporal resolution: Another important drawback in artificial vision is the occurrence of phosphene fading[200,201] owing to sustained electrical stimulation in response to unchanging incoming light. This phenomenon impacts retinal prosthetics and renders maintenance of continuous perception beyond flicker fusion nearly unachievable. Phosphene fading produced by retinal implants is believed to arise from the inner retinal circuits responsible for contrast adaptation[202,203]. Analogous to the adaptation observed with static visual stimuli (Troxler effect), the involvement of these circuits during RGC network-mediated stimulation (via epiretinal or subretinal implants), triggers an adaptive response to recurrent static electrical stimuli[202,204,205]. At the commonly employed stimulation frequencies for retinal stimulation, ranging from 5 to 30 Hz, RGC response ceases within a fraction of a second and the rate of desensitization increases with higher frequency[203]. In natural vision, ocular micromovements like microsaccades play a crucial role in refreshing the image projected onto the retina, preventing the Troxler effect[206]. In artificial vision, response adaptation can be avoided if the following conditions are true: a) light entering the eye through the pupil should activate the electrodes, a feature seen in photosensitive prostheses like Alpha AMS[207], PRIMA[152], and POLYRETINA[175,176]. This allows for effective shifts in the stimulated area of the retina through eye micromovements; b) The resolution of the stimulation array must be high to enable a shift of a few hundred micrometers (1°). This would ensure that moving the projected image by one or two electrodes over the prosthesis would stimulate different retinal areas; c) it is crucial to preserve physiological micromovements, as observed in age-related macular degeneration[152]. In order to refresh the visual field acquired by the camera, many retinal prostheses rely on head movements by the users[208]. Alternatively, eye trackers can be employed in cases where eye movements are still functional, and substantial voluntary eye movements can be used to adjust the region of interest within the camera's field of view[209]. Recent studies employing a naturalistic spatiotemporal modulation approach show success in reducing desensitization and extending RGC response duration to static stimulation in retinal explants[203]. The maximum reachable frame frequency is also another potential problem which affects the achieving of flicker fusion (the frequency at which an intermittent light appears steady to the observer) of 30 Hz or above. Until now, flicker fusion has been attained solely with the PRIMA device in AMD patients[152]. Lower frame frequencies (1 – 20 Hz) were noted for patients using other types of retinal prostheses, probably attributable to perceptual fading. Despite the extensive insights available on retinal prostheses, a deeper understanding of the spatiotemporal stimulation modulation is crucial to allow generation of individual phosphenes which could be combined to perceive objects and scenes.

Technological challenges

1. Electrode–tissue interface: The interface between electrodes and neural tissue holds paramount importance due to its mechanical, chemical, and electrical aspects[210,211]. The optimal arrangement involves positioning electrodes close to target

neurons to achieve precise and high-resolution stimulation, potentially down to a single neuron[212]. However, reducing the electrode size to be comparable with single neurons presents challenges of maintaining low impedance and high charge injection capacity in electrode materials. Surpassing the charge injection threshold can lead to irreversible harm to both electrodes and tissue. A possible solution is to use smaller electrodes which can safely deliver less charge compared to larger counterparts. Studies in explanted retinas show that smaller electrodes exhibit a higher charge density stimulation threshold and a lower dynamic range[213,214]. Over the past two decades, innovations such as carbon-based materials (e.g., graphene[215] and nanomaterials[216]) have been explored to enhance electrode-tissue interface performance[217–219]. Implantable devices made of conductive polymers have been extensively utilized in research due to the material softness, flexibility, conformity, and substantial charge injection capacity[219,220]. In essence, reducing electrode size holds the potential to substantially enhance the capacity of visual prostheses arrays by accommodating a greater number of electrodes. This development could translate into elevated visual acuity and improved visual function for patients.

2. Image processing: Since retinal processing involves the detection of particular features of the visual scene, another aspect that future retinal prostheses based on external cameras should rely on, is to bio-mimic the feature extraction function performed by the retina. Traditional computer vision approaches (e.g., edge detection, contrast enhancement) have shown limited usefulness in daily life[166,221,222] and newer alternatives (such as saliency detection, object recognition) have been tested[223] in combination with deep learning[224,225]. After pre-processing visual data and extracting relevant features, it is essential to create an individualized spatiotemporal stimulation plan with unique phosphene maps and the potential for these maps to undergo modifications over time. Researchers are also considering exploring bi-directional and closed loop feedback approaches which would allow automatic adjustment of stimulation parameters, thereby improving device performance[226,227].

3. Wireless power and data transmission: Neurostimulation has conventionally been conducted using electrodes connected to an electric pulse generator. Frequent breaks in these lead wires[163] result in device dysfunction or failure. Additionally, the cables exert mechanical pressure on the implant and can lead to persistent scarring over time[228]. These issues do not apply to photovoltaic devices which can wirelessly transduce light into an electrical signal. Organic bioelectronics and photovoltaics possess superior conformability, flexibility and stretchability characteristics as compared to silicon-based devices. It is fundamental to employ efficient materials that can reduce electrode size, enhance resolution, and still maintain satisfactory output current for stimulation.

Biological challenges

Gap exist in our knowledge of the neural visual code in visually impaired individuals and the implications of visual deprivation and plasticity[229]. Moreover, the extent to which experimental animals (sighted or blind) are reliable indicators of efficacy in humans

remains uncertain. When considering human studies, a high variability was reported in degree of remodelling, residual oculomotor behavior, visual pathway preservation and residual neuroplasticity. In fact, the history of blindness can have direct impact on the motor strategies and associative perceptions adopted by patient[230–232]. Synaptic reorganization can impact the efficiency of electrical stimulation[7,233,234], thus as a part of initial screening, it is crucial to verify retinal integrity[235] and excitability[121,235,236] in patients affected by retinal degenerations.

Although the field of retinal prostheses has made great advancements, subjects affected by retinal degeneration can only hope for vision substitution rather than full visual function restoration[237]. The next generation devices need to provide improved engineering, spatial and temporal resolution, stimulation strategies and image processing along with necessitating participant motivation and well-being.

1.4 NOVEL APPROACHES TO ORGANIC RETINAL PROSTHETICS

1.4.1 NANOPARTICLES FOR NEURONAL STIMULATION

Leveraging the exceptional attributes of nanoparticles (NPs), nanotechnology is fundamentally transforming the landscape of contemporary medicine, spanning from diagnostics to therapeutic applications. Many inorganic and organic NPs have progressed to clinical trials for various purposes, including medical imaging, drug delivery, and theranostics, with some receiving clinical approval for use[238]. In comparison to free drugs and larger medical devices like prostheses, NPs offer advantages such as simplified, targeted delivery; widespread distribution and diffusion; and the possibility of personalized formulation. One of the primary benefits of employing NPs lies in their ability, in addition to their advantageous surface-to-volume ratio, to be precisely adjusted for optical, electrical, magnetic, and biological applications. Notably, NPs are comparable in size to the main cellular components, such as synapses and intracellular organelles, facilitating the understanding of interaction with biological processes at nanoscale level. More recently, many studies have explored the potential of NPs to establish an interface with neurons, making them suitable for neurostimulation[216,239].

A novel approach for non-genetic optostimulation of neurons relies on the use of conjugated polymeric NPs. As mentioned earlier, opting for organic semiconductors offers clear advantages owing to their structural resemblance to the majority of natural molecules, which are built on conjugated carbon atoms. From a structural perspective, they possess critical attributes like biocompatibility[240], biodegradability[241], and flexibility[242,243]. On the functional front, they are capable of facilitating both electronic and ionic transport, a significant consideration given that the native communication system of biological tissues relies on ionic signalling. In addition to their optoelectronic characteristics, they possess additional attributes that render them highly suitable for biomedical purposes. Unlike inorganic compounds, organic backbone materials typically lend themselves to easier functionalization[244], both in terms of the carbon backbone and the side chains. This makes it feasible to customize the physical, chemical, and

biologically relevant properties of the conjugated polymer[241]. An example of backbone engineering involves incorporating donor-acceptor blocks to enhance charge generation upon photoexcitation[245]. Finally, weak nature of the interchain interactions in OCPs make them processable in mild conditions (low temperature, mild organic solvents). This lowers the costs and environmental impact of conjugated polymer based devices compared to conventional electronic and optoelectronic devices[241]. Moreover, such mild conditions are often compatible with sensitive molecules such as drugs or proteins, aiding straightforward loading or bioconjugation of polymeric NPs.

As previously discussed, P3HT is a well-studied conjugated polymer in the field of photovoltaics and vision restoration. It has found application not just as a planar substrate but has also been utilized at nanoscale level, as detailed in the section below.

LIQUID RETINA

Recently P3HT NPs have been used for the design of the "liquid" retina, a particular retinal prosthesis prototype injectable in the subretinal space. This prototype, developed at IIT, Italy, has the advantage of being able to be administered via a simple injection, in the absence of any surgical or geometrical constraints. "Liquid" retina is constructed using engineered P3HT NPs with an average diameter of approximately 300 nm[246]. These NPs are biocompatible and easy to inject, with improved spatial resolution and retinal coverage. *In vitro* studies indicated that these NPs do not internalize in neuronal cultures and when puffed between the outer plexiform layer and the choroid in retinal explants of RCS rats, they elicited light-dependent firing of retinal ganglion cells (**Figure 24**). When administered subretinally to young RCS rats (3-month-old), a substantial recovery of light-sensitivity was reported. *In vivo* electrophysiological characterization depicted a recovery in the amplitude of visually evoked potentials and an improved visual acuity up to 240 days after the surgery[247]. The idea of a "liquid" prosthetics solution was extended further by injecting P3HT NPs in RCS rats at a late stage of the disease (one year of age of

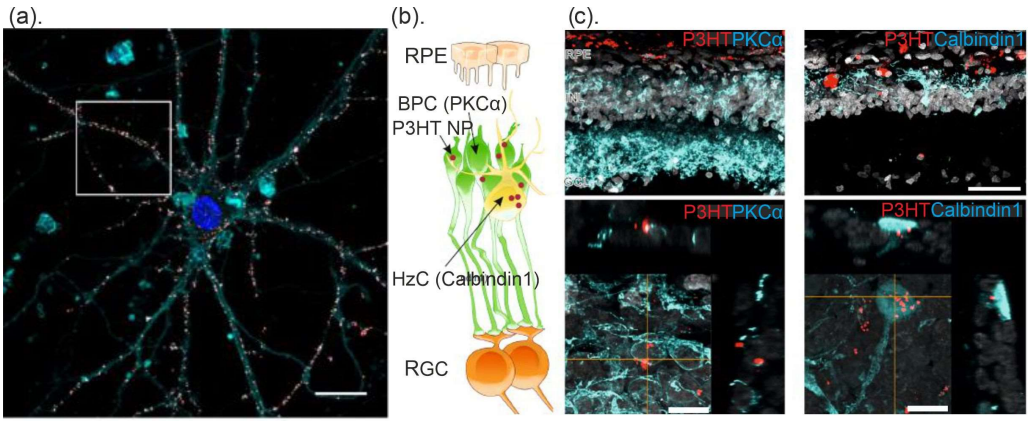

Figure 24. "Liquid" Retina. (a) Depiction of P3HT NPs (red) decorating the neuronal membrane (cyan) after 1 h of incubation; (b) A schematic illustration of P3HT NPs forming hybrid contacts with second-order retinal neurons, where rBPCs and HzCs were identified by using immunofluorescence markers, PKCα and Calbindin1, respectively; (c) Top: Representative transverse section images of 13/15-month-old P3HT-NP injected RCS animals stained for rBPCs or HzCs (blue). The P3HTNPs intrinsic fluorescence is in red. Scale bar, 50 µm; Bottom: Representative z-max projections with x- and y-orthoslices of super-resolution confocal images showing close contacts of P3HT-NPs with rBPCs and HzCs. Scale bar, 10 µm. Image adapted from Francia et al. 2022.

the animals), when the degeneration results in a complete rewiring of the inner retina[248]. The study allowed a translational analysis in the perspective of a human trial in which the possible treatment is feasible only at advanced stages of retinal degeneration. In this work, the retinas of young and old RCS rats and congenic non-dystrophic rats (rdy) were compared by OCT and immunofluorescence analysis showing a clear difference in both thickness of the inner retinal layers and number of photoreceptors. Behavioral and electrophysiological analysis demonstrated a significant recovery of light sensitivity and acuity. The results from the light-box test show that RCS animals treated with P3HT NPs recover their behavior to levels comparable to the one of normally sighted rdy rats and spend more time in the dark arena with respect to untreated rats or rats treated with a sham injection. These results opened the path towards the translational application of the "liquid" retinal prosthesis and called for improved prototypes that could enhanced the phototransduction process.

Stimulation voltage, current, and exciting light are crucial pillars of photovoltaic-driven retinal prosthesis. The table presented below offers a comparison between various photovoltaic devices (planar and NP-based) currently under study in different experimental systems.

	Experimental system	Device	Light intensity	References
Planar	in vitro	P3HT:PCBM+ ITO	10 mW/mm^2	Ghezzi et al., 2011
	retinal explant	Photovoltaic PRIMA	0.5 – 10 mW/mm^2	Mathieson et al., 2012
		P3HT/ITO	3 – 300 µW/mm^2	Ghezzi et al., 2013
		P3HT:PCBM + Pedot:PSS + Ti (Polyretina)	0.5 - 3 mW/mm^2	Ferlauto et al., 2018
		Photovoltaic PRIMA	8 mW/mm^2	Ho et al., 2018
		P3HT/Graphene	15 - 40 mW/mm^2	DiFrancesco et al., 2020
	in vivo	Photovoltaic PRIMA	10 mW/mm^2	Mandel et al., 2013
		Photovoltaic PRIMA	1 - 3 mW/mm^2	Lorach et al., 2015
		P3HT/ Pedot:PSS	2-30 lux (behaviour)	Maya-Vetencourt et al., 2017
		P3HT/Graphene	5 - 20 lux (behaviour)	Francia et al., 2022
Nanoparticles	in vitro	Semiconductor heirarchial nanocrystals	5 mW/mm^2	Sytnyk et al., 2017
	retinal explant	P3HT-NPs (acute NP puff)	20 - 40 mW/mm^2	Maya-Vetencourt et al. 2020
		P3HT-NPs (chronic NP administration)	20 mW/mm^2	Chiaravalli et al., 2023
		Oxidized core-shell P3HT-NPS	1 - 18 mW/mm^2	Barsotti et al., 2023
	in vivo	P3HT-NPs	2 - 10 lux (behaviour)	Maya-Vetencourt et al. 2020
		P3HT-NPs	2 - 10 lux (behaviour)	Francia et al., 2022

NANOPARTICLE SYNTHESIS METHODS

Conjugated polymeric NPs can be synthesized either through a bottom-up approach, where NPs are formed in situ during polymer synthesis (direct polymerization) or through a top-down approach, where NPs are formed post-polymerization. The choice of method depends on type of polymer, particle size requirement, application potential etc. While considering application in biomedical or environmental fields, it is necessary to ensure surfactant free NPs.

Post-polymerisation dispersion

This technique of NP synthesis generally relies on pre-prepared commercial polymers. The polymeric solution in an organic solvent is either emulsified with (mini emulsion) or precipitated in (reprecipitation) water (**Figure 25**). It is a widely employed fabrication strategy for conjugated polymeric NPs since it doesn't require elaborate equipment or expertise and allows for purification even post-polymerization. It is important for the polymer to display good solubility in organic solvents[249,250]. These solvents can lead to concerns regarding toxicity and environmental hazards and thus it is necessary to ensure the elimination of all residues in the final product. The technique allows particle size regulation by playing on factors such as polymer molecular weight, regioregularity, concentration, etc.

- Mini emulsion

One of the most common synthesis methods used for preparation of conjugated polymeric NPs, this technique utilizes a polymer dissolved in a water-immiscible organic solvent (e.g., chloroform, toluene, cyclohexane), injected into an aqueous solution. Rapid stirring of the mixture under ultrasonication and subsequent solvent evaporation forms a mini emulsion. As a pre-requisite, it is important to ensure the generation of sufficiently small drops, possessing colloidal stability even after solvent removal[251,252]. This can be achieved by high shear application, such that the formed mini emulsions avoid droplet coalescence. The addition of surfactants[253] generally SDS (sodium dodecyl sulfate) or poly (ethylene glycol) methyl methacrylate (PEGMA), in a concentration higher than critical micellar concentration counterbalances the interfacial tension between oil and water and prevents merging of smaller drops into larger ones (Ostwald Ripening[254]). NPs stabilized by a surfactant layer can be obtained from size 30 nm to 500 nm. Overall, the technique affords most control on NP fabrication, easily tunable parameters, and possibility of large-scale production. Some of the tunable parameters affecting NP morphology include nature and concentration of polymer and surfactant, nature of organic solvent, emulsion temperature etc. For example, changing the nature of organic solvent can impact optoelectronic properties of P3HT NPs[255,256]. Mini-emulsion NPs of conjugated polymer and fullerene-based acceptors typically adopt a core–shell type distribution during formation, confirmed using scanning transmission X-ray microscopy[257,258] and small angle neutron scattering[259] with corresponding bulk heterojunction devices reaching photo-conversion efficiencies of 2.5%.

- Reprecipitation

NP fabrication through reprecipitation (also known as nanoprecipitation or solvent displacement[260] method) involves dissolution of the polymer first into a water miscible organic solvent (e.g., tetrahydrofuran, THF), followed by rapid addition to large excess of water. A rapid change in solvent polarity favours π–π stacking and polymer chain folding, forcing water exclusion to minimise contact area of the hydrophobic polymer[244,261]. Usually, this process is aided by stirring or sonication, and does not involve use of surfactants or other additives such as hydrophobes. The evaporation of

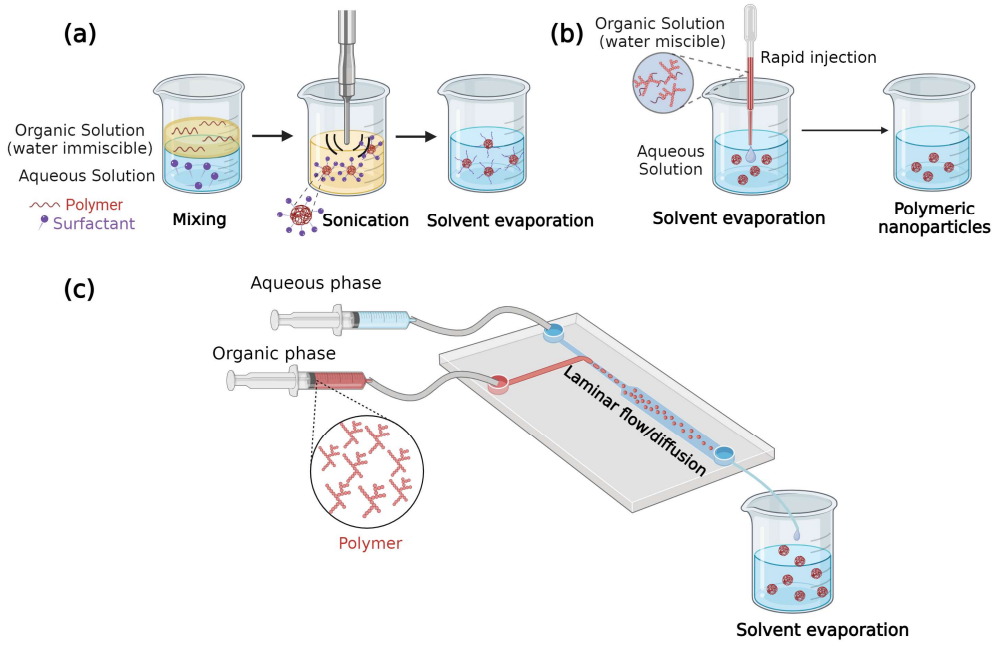

Figure 25. Schematic representation of post-polymerisation methods for the fabrication of Semiconducting Polymeric NPs. (a) Mini emulsion; (b) Reprecipitation; (c) Microfluidic assisted reprecipitation. Schematic made with BioRender, not to scale.

the solvent leaves a dispersion of polymer NPs in water[261,262]. This method, however, commonly produces NPs with wide size distribution and high degree of polydispersity, which can be fine-tuned for a particular sub population using techniques such as differential centrifugation[263]. By altering reaction parameters, formation of NPs with different sizes and morphologies is possible. For example, research shows polythiophene based NP size can be reduced by: (i) reducing the starting concentration of polymer, (ii) improving polymer regioregularity and mono-dispersity, and (iii) increasing the volume of solvent used[261,264]. NP formation during reprecipitation follows three stages: nucleation (i.e., initiation of reaction by physical mixing/activation), particle growth and particle aggregation. When polymer concentration in solution exceeds the maximum solvable amount, saturation occurs, leading to nucleation[265]. It has been shown that achieving high nucleation rates is a key result in obtaining uniform NPs of small size. This is because increasing the flow rate leads to rapid mixing of the solvent with anti-solvent, thereby favouring reduction of mean particle size[266].

- Microfluidic assisted fabrication

It is difficult to control the random nature of micro-environments, which leads to batch-to-batch NP variability. To curtail this problem, using a microfluidic device allows high reproducibility of synthesis, owing to control over experimental parameters. The microfluidic technique utilizes the same physical principles for NP formation as described previously but is considered a significant technological evolution over the bulk post polymerization methods. This is because it allows for fine tuning of relative flow rate of organic and aqueous phase by the microfluidic device, leading to monodisperse population of NPs with high production yield. The production is easily scalable and requires low reagent consumption[267,268]. Continuous flow microfluidics promotes rapid mixing of two miscible liquids by simple diffusion. The liquid streams can be manipulated and combined to form a sharp interface with precise tuning, leading to nanoprecipitation of polymeric NPs. It has been shown that size, polydispersity and drug loading ability of polymeric NPs could be optimized with varying flow rates, polymer concentration and composition[269]. Kang and co-workers fabricated methoxyl poly-(ethylene glycol)–poly-(lactic-co-glycolic acid) (MPEG–PLGA) block copolymers through parallel flow focusing microfluidics and compared them to those prepared by reprecipitation. Microfluidic assisted fabrication rendered highly monodisperse polymeric NPs with greatly improved speed of production. The parallel flow focusing device provided operational simplicity along with a potential of scaling up production[270]. In another study, the authors compared fabrication of rutin-loaded PLGA NPs using microfluidics v/s bulk production. The NPs produced using microfluidics method resulted in possessing higher entrapment efficiency and smaller size, showing faster drug release kinetics[271]. Wang et al. proposed another example of direct control of polymeric NPs properties, namely size and polydispersity, by controlling the antisolvent composition and the Reynolds number in a microfluidic system[272]. Droplet-based microfluidics enables the addition of discrete small volumes of polymer solution into a laminar flow of immiscible phase, forming a controlled and tuneable microemulsion[273]. Kuhene and co-workers demonstrated efficient fabrication synthesis of conjugated polymer NPs through a microfluidic drop-making device[274,275]. The particle size could be tuned between 150 nm and 2 µm by simply increasing the PFO solution concentration.

<u>Direct polymerisation in disperse heterophase systems</u>

With a goal of achieving desired properties depending upon the area of application, NPs can be prepared by direct polymerization of a monomer (or combination of monomers). Monomers are polymerised directly into a dispersing medium that is a non- solvent for the polymer, typically an aqueous solution of an initiator or catalyst to start the polymerisation reaction and a surfactant to stabilise the forming NPs. In dispersion polymerization, the monomer is completely miscible in dispersing medium while the polymer is not. Aggregation of the formed NPs is prevented by addition of stabilizers. In contrast, the emulsion polymerization utilizes a monomer with limited solubility in dispersing medium, forming a separate droplet phase. The process of synthesizing semiconducting polymeric NPs (SPN) through direct polymerization is specialized, as it demands substantial knowledge in synthetic chemistry and access to appropriate laboratory equipment. Nevertheless, this method provides the advantage of utilizing

polymers with low solubility in organic solvents. Additionally, it offers the ability to directly manage particle size by adjusting the extent of polymerization[261].

- Emulsion polymerisation

A widely used, fast, readily scalable method for NP synthesis, it uses water as a dispersion medium, promoting environment friendly synthesis and easy heat dissipation. The organic-phase-soluble monomer and catalyst are dissolved within the organic component, which is then transformed into an emulsion by blending it with an aqueous surfactant solution using constant stirring. Polymerization initiates within the organic droplets, and as the polymer chains steadily extend, this leads to the formation of polymer NPs. These NPs are stabilised by the surfactant. If this emulsion remains stable throughout the polymerization process, it is referred to as mini emulsion polymerization[276]. In this scenario, the goal is for each monomer droplet to ideally undergo polymerization, resulting in the creation of a NP. Notably, the technique utilizes a high shear device such as an ultrasound for emulsification[277]. Microemulsions are even more stable mixtures of organic and aqueous phases. The degree of dispersion is so high that the two phases are not macroscopically separated, and the NPs formed are typically very small (< 20 nm)[278]. Addition of high quantity of surfactant decreases the interfacial tension at oil/water interface, a crucial step in this technique. The polymerization kinetics is often governed by the type and concentration of initiator, surfactant and monomer[279].

- Dispersion polymerisation

This is a unique, one-step process to obtain monodisperse populations of polymer NPs. In contrast with emulsion polymerization, here the monomer, as well as the initiator are both soluble in the solvent, but the polymer is not. Upon solvent interaction, the polymer chains swell until they reach a critical chain length. This causes a sharp decrease in solubility followed by phase separation. The polymerization continues within swollen particles until all the monomer is used up, rendering an aqueous dispersion of polymer NPs. The resultant particles are in the size range 0.1–10 μm. The presence of a stabilizer promotes steric repulsion between growing particles and prevents coagulation[280]. Application of polymeric particles has been extensively investigated in fields of electronics, organic synthesis, biomedical engineering etc[281].

In the light of the above, post-polymerisation dispersion methods, especially reprecipitation, offer the possibility of easy implementation and scaling up. The utilization of microfluidic systems, which offer both control and uninterrupted production, positions microfluidic-assisted nanoprecipitation as the most promising fabrication strategy toward the large-scale and Good Manufacturing Practice production of SPNs required for clinical trials and applications.

MECHANISMS OF OPTOELECTRONIC STIMULATION OF CELLS

The literature outlines three primary mechanisms through which OCPs can transduce an optical signal into a bioelectronic one: photothermal, photochemical, and photovoltaic. These mechanisms frequently coexist within organic optoelectronic devices, with each mode's contribution contingent on various factors such as illumination specifics

(wavelength, duration, intensity), material attributes, and device architecture[220]. Furthermore, the interface between an OCP and an electrolyte (like extracellular fluid), demonstrates a diffuse, intermixed, and dynamic nature, owing to the penetration of water, ions, and small molecules into the OCP. This intricate dynamic gives rise to various interfacial phenomena that are often challenging to disentangle[282].

Photothermal mechanism

Efficient thermal stimulation depends on strong light absorption and the dissipation of energy without radiation. The non-radiative relaxation of the photo-induced excited state results in localized temperature elevation, known as the photothermal effect. Beyond a specific threshold (approximately 47 °C), this temperature rise induces cellular apoptosis, necroptosis, and necrosis, making it useful for activities like photothermal cancer treatment and sterilization[283]. Nonetheless, more controlled temperature increments can initiate an electrical response within the cell. This response arises from two distinct phenomena, illustrated in **Figure 26**; the opening of temperature-sensitive ion channels leading to an increased membrane conductance, and an elevation in membrane capacitance, recognized as opto-capacitance. As the temperature rises, the cell membrane experiences a phase transition, leading to an expansion of its surface area and a reduction in its thickness. This primarily arises from the significant temperature-dependent trans-gauche rotational isomerization of the hydrocarbon

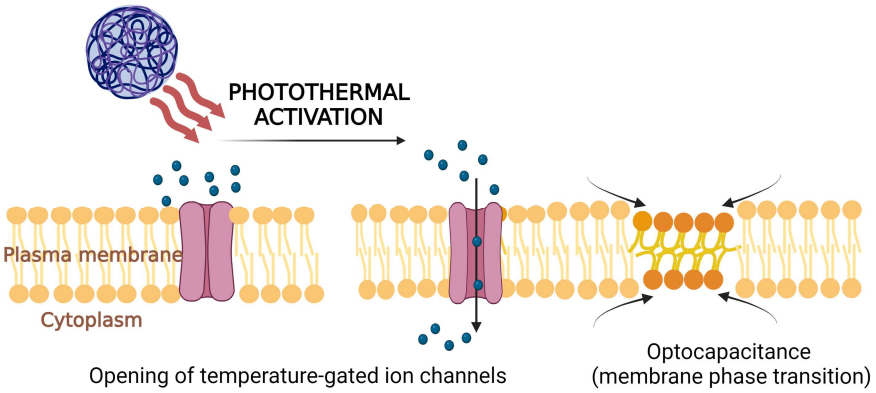

Figure 26. Schematic of cell optoelectronic stimulation mediated by organic conjugated polymers via the photothermal mechanism.

chains within the phospholipids. This rotation causes an increase in the angle between the tails of the phospholipids, inducing horizontal strain on the membrane[284]. Following the equation of a parallel plate capacitor C = eA/d (where "C" represents capacitance, "e" the permittivity of the dielectric, "A" the plate area, and "d" the dielectric thickness), the increased membrane area and decreased membrane thickness contribute to an elevation in membrane capacitance, triggering the movement of charges, known as opto-capacitive current[285].

Tests were carried out on HEK-293 cells cultivated on conjugated polymeric films to isolate the direct impacts of photostimulation on the plasma membrane potential[286]. Evaluation of capacitive charging at the polymer-electrolyte interface was carried out. To specifically isolate the thermal effect, a neutral glass plate was used to replace the

Indium Tin Oxide substrate upon which P3HT film was coated. This modification minimized the elevation of charge separation. The rapid depolarizing spike patterns that had been observed previously were no longer reported, thus attributing to generation of surface potential at the P3HT/Indium Tin Oxide interface. Conversely, a more gradual response element marked by a transient depolarization followed by hyperpolarization emerged. This component seemed unrelated to the electrical process and persisted even on a glass substrate, although not in the absence of the polymer. Given the absence of apparent correlation with other fundamental electrical properties, heating in the device proximity was the most likely source of this effect. The temperature rose by 3 to 7 °C during 20 ms or 200 ms of stimulation, respectively, at a maximum intensity of 57 mW/mm^2. This might stem from temperature-dependent alterations in the physical attributes of the cell membrane, such as different orderings within the lipid bilayer gel or liquid phase, along with a reduction in its thickness. Moreover, as the temperature increased, ion transportation through the membrane was facilitated, leading to reduced membrane resistance or even the inversion of membrane potential.

Several temperature-responsive ion channels have been identified throughout the years[287]. However, one of the most extensively characterized and widely utilized for biomedical applications is the transient receptor potential vanilloid member 1 (TRPV1). TRPV1 is an ion channel permeable to calcium ions (Ca^{2+}) that opens in response to noxious heat (> 43 °C), capsaicin, and acidic pH[288,289]. Targeting TRPV1 selectively can augment the effectiveness of photothermal stimulation, as illustrated by Lyu et al. (2016), who functionalized their poly(cyclopentadithiophene-alt-diketopyrrolopyrrole) SPNs with an anti-TRPV1 antibody[290]. Often, comparing the cellular electrical response to photo-stimulation in the absence and presence of TRPV1 blockers is employed to validate or dismiss the photothermal mechanism[247,291]. HEK-293 cells were stably transfected with the human TRPV1 channel in order to investigate a possible channel control by means of conjugated polymer illumination-mediated temperature increase[292]. While the typical depolarization-hyperpolarization response pattern was confirmed in untreated HEK-293 cells cultured on P3HT, transfected cells showed a different response. A depolarizing outward current attributed to TRPV1 activation (the current is completely suppressed in the presence of TRPV1 blockers like Ruthenium Red or Capsazepine), in fact, overruled the expected hyperpolarization. Nevertheless, despite the extremely high light intensities used (up to 350 mW/mm^2), the bath temperature never reached the reported activation threshold for TRPV1 channels (43 °C). TRPV1 activation temperature can be indeed lowered by several factors, such as protons[293]. Low pH[294], in fact, can both lower the activation threshold of the channel, as well as activate it independently. In the presence of a strong buffer solution, lower voltage changes could be recorded. When the P3HT film is illuminated, the accumulation of photo-generated electrons at the surface is progressively balanced by acidification of the solution and localizing specifically where the light is hitting the film. Since both the temperature increase and the pH decrease are extremely localized, in view of possible applications in retinal prosthetics, this offers the P3HT films a spatial resolution that far exceeds that achieved by electrode-based devices currently on the market. This peculiar mechanism could therefore be classified as a synergetic action of mild capacitive and mild photochemical mechanisms.

Photochemical mechanism

Intersystem crossing is an exciton decay mechanism, where a transition in spin multiplicity from a singlet excited state to a triplet excited state within the polymer facilitates the transfer of energy from the photoexcited polymer to molecular oxygen, which holds a triplet ground state. This interaction results in the creation of singlet oxygen. Nevertheless, a more straightforward Förster resonance energy transfer (FRET) mechanism has been proposed as the primary route for reactive oxygen species generation upon the photoexcitation of OCPs within an aqueous environment (**Figure** 27). The energy levels of the model polymer P3HT and other OCPs with low band gaps[295] align well with the reduction potential of molecular oxygen in neutral physiological conditions. This alignment facilitates the efficient reduction of molecular oxygen into superoxide (O_2^-) in less than a millisecond. Subsequent redox reactions can lead to the formation of hydrogen peroxide (H_2O_2) and hydroxyl radicals (OH^-)[296–298]. Particularly in

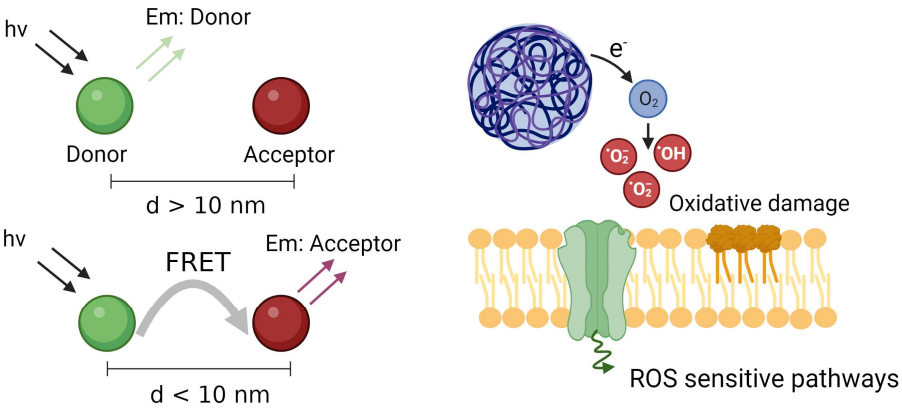

Figure 27. Schematic of cell optoelectronic stimulation mediated by organic conjugated polymers via the photochemical mechanism.

biological contexts, the generation of reactive oxygen species should be minimized since excessive oxidative stress, once it surpasses a certain threshold, could lead to cell lethality. Nonetheless, at lower concentrations, these molecules naturally participate in essential biological processes, implying that they could potentially influence membrane characteristics by temporarily altering ionic conductivity, interacting with extracellular proteins, or affecting neurotransmitter uptake and stability. Thus, conjugated polymers operating at sufficiently low light intensities may manage to avert any undesirable reactive oxygen species production. Various strategies, rooted in either interface manipulation or meticulous design of the stimulation protocol, have been suggested to curb irreversible faradaic reactions and the production of reactive oxygen species at the electrode/electrolyte interface[299,300].

While excessive reactive oxygen species indeed contribute to oxidative stress and resultant damage[301], lower levels play a crucial role in cellular physiology. In recent years, there has been a growing interest in controlled production of non-harmful quantities of reactive oxygen species to regulate cell physiology. For instance, Tortiglione et al. proposed controlled reactive oxygen species generation as the primary mechanism underlying the observed effects following the photoexcitation of P3HT NPs

in the freshwater polyp Hydra Vulgaris, a small freshwater hydroid. The researchers speculated that P3HT NPs, located near mitochondria after being internalized by cells, activated flavins, and cytochrome, thus enhancing the respiratory chain and ATP production. This, in turn, bolstered the activity of ATP-driven Ca^{2+} ion pumps, leading to changes in Ca^{2+} dynamics that triggered both muscle contraction and the activation of specific transcription factors[302]. This mechanism was further substantiated through more detailed mechanistic investigations conducted both *in vitro*[303,304] and *in vivo*[305] by the same research group.

Photovoltaic mechanism

The photovoltaic effect involves the separation of excitons into electrons and holes. In organic optoelectronic devices, this separation of charges is often enhanced through internal interfaces between materials with aligned energy levels, like conducting/semiconducting OCPs[174,185], organic PN junctions[306,307], and donor-acceptor blends[184]. This process has also been observed in single polymer systems, albeit with lower efficiency. Charge separation occurs due to the semiconducting polymer surface's polarization, which is a result of asymmetric diffusion of positive and negative charge carriers and interfacial phenomen[308]. The direction of incident light creates a concentration gradient of charge carriers according to the Lambert-Beer law[309]. Holes diffuse rapidly through the polymer bulk, while electrons remain localized, leading to negative charging of the illuminated polymer surface. This polarization induces ion rearrangement at the polymer-cell interface, as shown in **Figure 28;** positive ions gather at the polymer surface, and negative ions accumulate on the external side of the cell membrane, causing cellular depolarization. This capacitive electrode-cell coupling is a safe and reversible mechanism for cell stimulation, which is highly desirable in

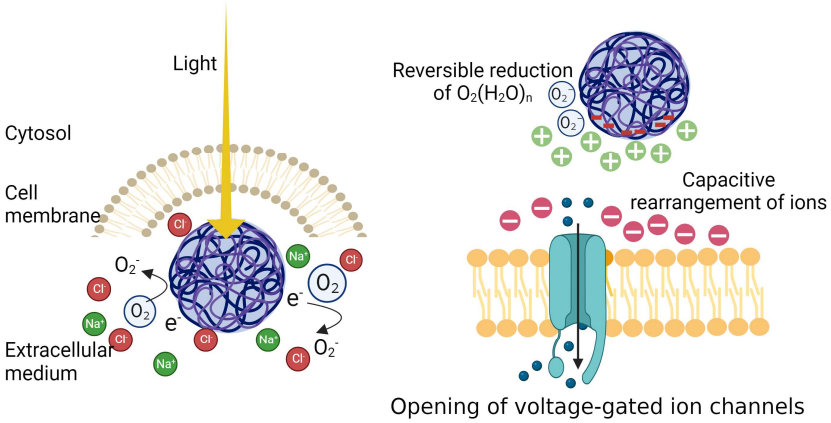

Figure 28. Schematic of cell optoelectronic stimulation mediated by organic conjugated polymers via the photovoltaic mechanism.

bioelectronic medicine[299]. However, achieving efficient purely capacitive stimulation is uncommon and often involves complex multilayer devices, sometimes including a metal electrode[306,307]

A proposed "pseudocapacitive" mechanism for charge transfer at the interface between the polymer and the electrolyte takes into consideration the intricate, diffuse, and

dynamic nature of the interface between OCP and electrolytes[282]
The polymer matrix allows for the penetration of both water and ions, and this permeability is enhanced by the light-induced polarization of the polymer, resulting in increased hydrophilicity[310]. A significant component found at this interface is hydrated oxygen ($O_2(H_2O)_n$). This hydrated oxygen has a higher electron affinity compared to molecular oxygen and when electrons accumulate at the polymer's surface due to light-induced polarization, transient charge transfer complexes are formed between the polymer and the hydrated oxygen. This leads to the reversible oxidation of the polymer and the reversible formation and accumulation of O_2 at the interface between the polymer and the electrolyte. The accumulation of O_2 helps stabilize charge separation within the polymer, thus promoting efficient electrical coupling with the cell[311]. This stabilization of O_2 is facilitated by the polarized solvation layer, which limits its irreversible further reduction and the generation of reactive oxygen species. Once the light stimulus ends, electrons are released from the oxygen complexes, restoring the polymer's electroneutrality[310].

Another consequence of the build-up of negative charges at the surface of the polymer is the acidification of the interface due to the creation of an electron-deficient localized environment. In their comprehensive study to dissect the photoinduced processes occurring at the interface between P3HT and the electrolyte, Mosconi et al. employed CdSe/CdS nanocrystals as pH sensors to demonstrate the reduction in local pH upon illumination[308,310]. This change in pH holds significance for various ion channels, including glutamate receptors, voltage-gated ion channels, and TRPV-1, which exhibit substantial dependence on pH[292,312,313]. Additionally, specialized ion channels that are sensitive to acidity are also present on the neural membrane[314].

1.4.2 GRAPHENE AND ITS APPLICATION WITH CONJUGATED POLYMERS

Graphene was first isolated and characterized in 2004 as a two-dimensional lattice consisting of a single or a few layers of carbon atoms, bonded in a honeycomb pattern through Sp^2-bonds. Each carbon atom in graphene forms three μ-bonds and one out-of-plane π-bond that enables it to connect with adjacent atoms[315]. This unique structure renders graphene the thinnest material ever identified, with a thickness of just one atom, and makes it the strongest compound known. Graphene exhibits a low weight/surface ratio, an extremely high electrical conductivity and high flexibility, although preserving resistance to stretch and lateral deformations, and a compatibility with live cells and tissues.

Graphene has been employed, among many other applications, in photovoltaics for example as cathode[316], anode[317], or charge transport layer[318], owing to its excellent optical transparency and favourable work function, which enhances charge separation. A significant challenge in P3HT:PCBM solar cells, which are widely used in organic blends, is the insufficient hole transport. This is primarily because the electron-donating polymer's hole mobility is notably lower than the electron mobility exhibited by commonly used acceptors, thus limiting charge collection at the photoanode. The disparity in mobility leads to the accumulation of a positive space charge at the photoanode, resulting in the

entrapment of electrons near the rear electrode. The synergy between graphene-based materials interfaced with organic donor-acceptor semiconductors leads to enhanced collection of photons, generation of excitons and separation of charges[319,320]. Due to its affordability, abundance, non-toxic nature, and comparable electrical conductivity, it can be employed as substitute for indium in indium tin oxide anodes in bulk heterojunction OSCs. Koo and coworkers (2020) reported that the integration of graphene-based materials into OSCs resulted in a substantial enhancement of power conversion efficiency (15.2%)[321].

Recently, different graphene-based prototypes have been engineered for a variety of purposes in the biomedical field[215,322–324]. A study by Zhang et al. (2022) demonstrated the potential of graphene-based electrodes to directly record electrical activity of stimulated RGCs (including distinction in ON, OFF, ON-OFF responses) under light stimulation[325]. Kshirsagar et al. (2019) documented use of transparent graphene/PEDOT:PSS microelectrodes for optical imaging and electrophysiology[326]. Yan and co-workers (2016) synthesized polypyrrole/graphene nanofibers which enabled guided growth and electrical stimulation of RGCs. Following electrical stimulation, there was a notable improvement in the survival, growth of neurites, and anti-aging capacity of RGCs, indicating a potential for optic nerve regeneration[327]. Furthermore, NoroozOliaei and his team (2022) designed an electromagnetic model for human retinal photoreceptors, utilizing graphene-based resonators. Multifocal electroretinogram clinical and experimental results confirm the efficacy of the model in stimulating photoreceptor cells, leading to the generation of electrochemical voltage and current[328]. A flexible microprobe constructed with graphene using microelectromechanical system technology has demonstrated excellent resolution in detecting electrophysiological signals from diverse biological entities. The high signal-to-noise ratio during recording makes it a promising candidate for extended *in vivo* recordings and utilization in retinal prosthetics[329]. In a recent study, Nguyen and colleagues (2021) investigated the biocompatibility of graphene coated polyimide implants in blind P23H rats. Following a three-month period of *in vivo* monitoring, the implant's stability was confirmed through OCT and examination of the eye fundus. Confocal imaging revealed that graphene had reduced the presence of microglial cells, thereby promoting microglial reconstruction within the retina, indicating a high biocompatibility[330]. A benchmarking study by Cruz et al. (2022) utilized graphene-based microelectrode arrays for multisite corneal recordings. They exploited the flexibility and transparency of graphene to develop electroretinography electrodes which could accurately record signals across a broad spectrum of conditions[331]. Kireev et al (2018) reported a facile, straight-forward wafer-scale production of ultra-flexible graphene/polyamide-based probes, with potential application in retinal and cortical neuroprosthetics[332].

To obtain enhanced neuronal photo stimulation, DiFrancesco et al. (2020) tailored a fully organic P3HT-graphene based planar interface with improved phototransduction, while preserving biocompatibility and flexibility[333]. After assessing the preservation of the viability of primary hippocampal neurons cultured on the graphene-based devices, light-induced membrane voltage modulation was investigated by patch-clamp experiments. All experiments were performed comparing the graphene-based device with a prototype

with PEDOT:PSS instead of graphene and with a sham control of PET (polyethylene terephthalate) alone, as a non-photoactive control. During light stimulation the neurons cultured on P3HT-based devices showed a hyperpolarizing response when no current was injected, while a depolarizing effect was shown when holding the voltage at -70 mV. No activity modulation was detected in neurons in contact with the PET control device. Under all recording conditions, the presence of graphene resulted in a significantly enhanced light-dependent membrane voltage modulation. These results confirmed the higher modulation of the neuronal activity given by the graphene-based devices with respect to the previous ones designed with PEDOT:PSS. The same group also evaluated the effectiveness of this device on the recovery of light-sensitivity in dystrophic retinal explants. Firing activity was evaluated by MEA experiments on the explanted dystrophic retinas from 12 to 14 months-old dystrophic RCS rats, while preserving the choroid in place. In control retinas or in the presence of PET only control devices there was no significant photostimulation, while with P3HT-based prototypes there was a significant firing modulation in response to light stimulation. Furthermore, devices with graphene triggered a higher light-dependent modulation of the RGCs firing rate that was more intense than that observed in presence of the PEDOT:PSS devices, confirming the results obtained in vitro on primary neurons. Given the promising results of the combination of P3HT and graphene *in vitro* and *ex vivo*, the device has been characterized *in vivo* after a subretinal implantation in 5 months-old blind RCS rats, using as sham control a PET substrate of the same size[334] (**Figure 29**). OCT carried out 30 days after subretinal surgery revealed no relevant damage of the retina in all the animals, demonstrating the safety of the procedure and the biocompatibility of the devices. Immunohistochemical characterization confirmed absence of inflammatory reactions and pupillary light reflex analysis demonstrated that rats implanted with P3HT-graphene devices had a significantly larger pupillary constriction than sham-implanted control groups. Moreover, P3HT-graphene implanted rats showed a smaller relaxation of the pupil, indicating that the involvement of intrinsically sensitive RGCs was also rescued to the level of healthy control rats. In addition, the light-dark box test showed that rats implanted with P3HT-graphene devices recovered the dark preference and a short escape latency from the illuminated chamber. Finally, the recording of pattern VEPs demonstrated the rescue of visual acuity in P3HT-graphene implanted animals.

Overall, these results proved the P3HT and graphene photovoltaic device to be a suitable strategy for visual restoration at cortical and subcortical level, inspiring the engineering of the NPs described in this thesis.

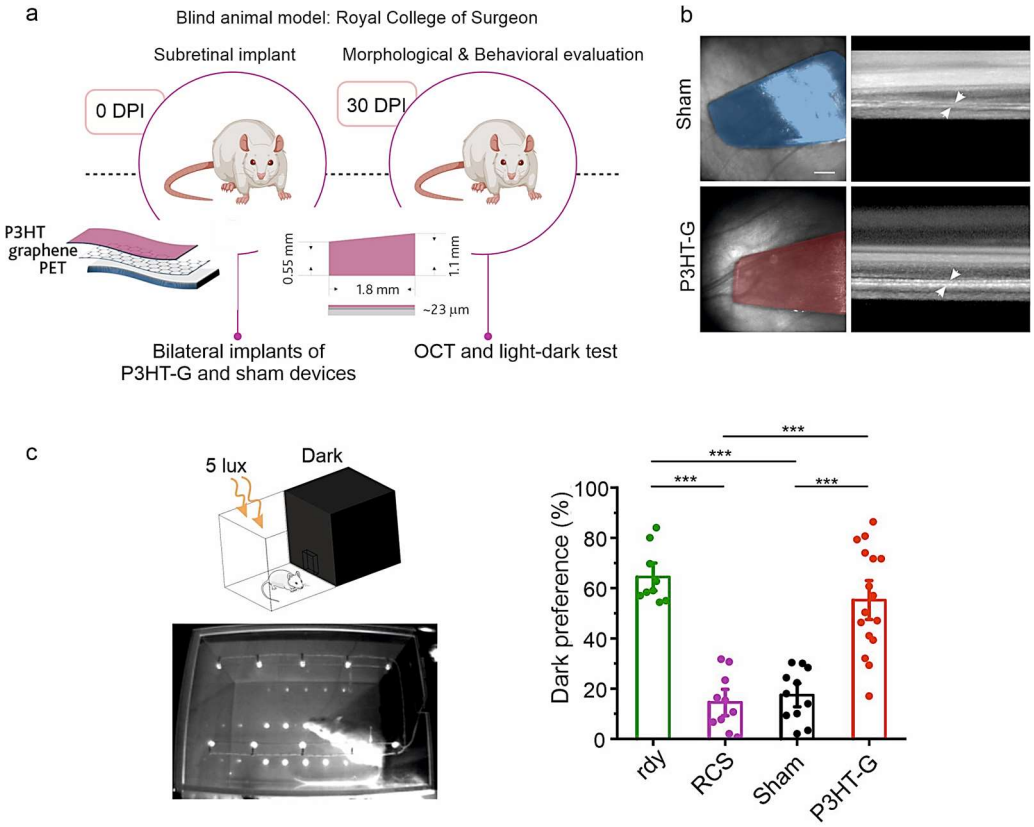

Figure 29. P3HT-Graphene device for restoring visual function in a rat model of RP. (a) Schematic representation of the retinal prosthesis architecture and timeline of the *in vivo* experiments; (b) Representative fundus images of the retina of Sham (light blue) and P3HT-G- (magenta) implanted rats showing the sagittal view of the prosthetic placement at 30 DPI (left; scale bar, 1 mm), along with the corresponding OCT images displaying the transversal section of the retinas and the devices positioned subretinally (right, white arrowheads; scale bar, 200 µm); (c) Left: Schematic representation of a light-dark box setup (top) and stop-frame video recording of an experiment conducted at 30 DPI. Right: Percent time sent in the dark compartment. RCS rats subretinally implanted with P3HT-G show a significantly increased dark preference for Sham-implanted or non-implanted blind RCS rats. Data are means ± sem with superimposed individual points. $^{**}p < 0.01$, $^{***}p < 0.001$, one-way ANOVA followed by Bonferroni's post hoc test (Sample size: 9, 10, 11, 16 for rdy, RCS, Sham, and P3HT-G, respectively). Image adapted from Francia et al. 2023.

1.5 RATIONALE OF THE RESEARCH

Conjugated polymers display optoelectronic properties, which makes their incorporation a central idea in the new age organic bioelectronics. The positive outcomes achieved with the organic retinal prosthesis created previously, served as motivation for the objective of this thesis to enhance the performance of the subretinal prosthetic approach. Some obstacles that the existing approaches face, include inability to efficiently modulate retinal activity at low light intensity and sub-optimal spatial resolution. In an effort to tackle these shortcomings, the goal of this thesis has been to characterize new prototypes of NPs that combine the idea of the "liquid" retina technology and the potential of P3HT and graphene coupling. This thesis will address the above-mentioned problems by providing a system with higher phototransduction efficiency, owing to improved electrochemical properties of graphene entrapped conjugated polymer system. In addition, nanoscale stimulation will allow a spatial confinement of the desired effect, with a resolution which is comparable to the characteristic size of the cellular membrane.

NPs were synthesized as a heterojunction of P3HT:PCBM and blended with graphene to investigate the possible improvement of charge separation upon illumination in dystrophic retinal explants. This thesis shows the synthesis and characterization of these novel P3HT:PCBM:GO NPs, and their comparison with P3HT and P3HT:PCBM NPs fabricated under sterility. This is followed by evaluating various purification protocols and assessing NP concentration. Subsequently, viability analysis of the NPs cultured with mouse primary hippocampal neurons, as well as co-localization analysis of the nanomaterials with neuronal membrane was performed. Finally, an *ex vivo* electrophysiological study showing the effect of P3HT:PCBM:GO NPs under light stimulation compared with the previously engineered P3HT:PCBM NPs in dystrophic retinal explants was carried out. A brief overview of the experiments performed *in vivo,* and future applications of the NPs is also provided.

2 RESULTS

2.1 ENGINEERING OF INJECTABLE POLYMERIC NANOPARTICLE PROTOTYPES

2.1.1 P3HT NANOPARTICLES

As highlighted earlier, conjugated polymers possess optoelectronic characteristics that position them as a pivotal element in modern organic bioelectronics. Their utilization in the production of subretinal prosthetics presents numerous benefits when compared to previously reported methods. Recent works[247,248] demonstrate the potential of conjugated polymeric NPs to be employed as a "liquid" retina prosthesis for vision restoration in blind animal models with RP. Despite marking a significant achievement in the field, open questions about their working mechanism remain. In view of addressing as well as understanding this complex interaction, the following section details the synthesis of P3HT NPs and their proposed coupling mechanism with the neuronal membrane.

SYNTHESIS OF P3HT NANOPARTICLES

As discussed in the introduction, once the polymer is synthesized, NPs can be formulated with two main different methods: mini emulsion and reprecipitation[262]. More recently,

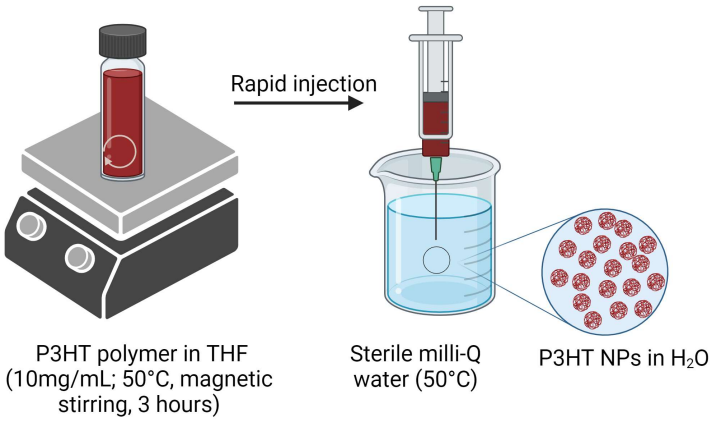

Figure 30. P3HT NPs synthesized using the reprecipitation method. Synthesis protocol of the NPs, including the preparation of polymeric solution in THF followed by a rapid injection into water leading to the formation of P3HT NPs.

there has been increased interest in microfluidic-based NP synthesis[335], which is arguably a technical evolution of the previous methods. After a quick screening of the possible formulation routes, reprecipitation was chosen as the best trade-off between reproducibility and ease of execution[336]. In addition, the method is devoid of surfactant use which is crucial when considering potential biological application. The NPs were synthesized (**Figure 30**) from commercial P3HT solution in tetrahydrofuran (THF) at a concentration of 10 mg/ml. The polymer was dissolved in the organic solvent at 50 °C under magnetic stirring (3 hours). The NPs were then obtained wherein a rapid, single injection of the polymeric solution was dropped in sterile Milli-Q water (1 part injection

in 9 parts water). Different optimization conditions were tested by varying the temperature of the Milli-Q water (room temperature v/s elevated temperature), the presence of mechanical action (sonication or stirring of aqueous phase) and different injection heights (syringe touching water surface v/s immersed mid height into water at the time of injection). The most reproducible results were obtained with maintaining the water at 50 °C at the time of injection, using no mechanical action and immersion of syringe at mid-water level while making the injection. The obtained colloidal suspension of P3HT NPs was filtered through a sterile 0.45 µm polyvinylidene fluoride (PVDF) syringe filter to remove the aggregates and obtain homogeneity.

PROPOSED MECHANISM OF CHARGE SEPARATION

Recent works from our group show that an injection of organic photovoltaic P3HT NPs into the subretinal space of RCS rats can partially restore light sensitivity. Upon injection in the subretinal space, the NPs establish tight contacts with second order retinal neurons in the inner layers, effectively substituting the degenerated photoreceptors. When exposed to light, these NPs convert light into a bioelectrical signal that stimulates bipolar cells, thus reactivating the visual pathway. The mechanism behind this phototransduction has been proposed and discussed in recent scientific

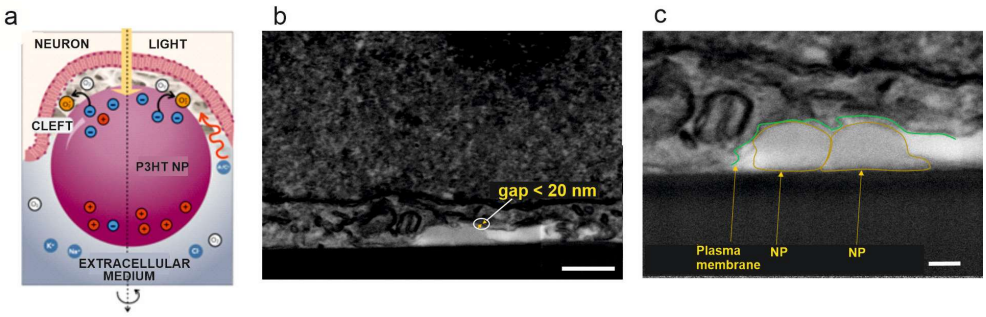

Figure 31. Characterization of the cleft between P3HT-NPs and cell membrane. (a) Cross-section of the 3D neuronal membrane engulfing the P3HT NP, surrounded by a proteinic cleft region and by the extra-junctional electrolytic solution; (b, c) Low and high magnification images of the NP-neuron contact obtained from FIB/SEM analysis. The junctional neuronal membrane wraps the NP forming a quasi-virtual cleft (scale bar 500 nm and 200 nm

literature[174,247,248,286,337].

In this study, the mechanism of charge separation in P3HT NPs and their photo stimulation action were investigated by simulating the evolution of the electrical potential in three domains of interest: the intracellular compartment, the NP itself, and the cleft between the neuron and the particle (**Figure 31**). The essential physics is well-captured by the 1D-numerical solution of the drift-diffusion model in the NP, coupled to Poisson-Nernst-Planck equations for the ions in the cleft and extracellular medium. In the crystalline regions of the P3HT NP, long-lived separated charge pairs are formed[338]. The initial Lambert-Beer profile within the NP instigates the diffusion of carriers, resulting in an accumulation of negative charges on the illuminated surface and a surplus of positive charges on the opposite side. This charge separation phenomenon arises due to the well-documented asymmetry in carrier mobility: holes disperse evenly throughout the film, whereas electrons (known as negative polarons) exhibit limited mobility. The

spatial separation of these photo-induced charge carriers leads to the electrical polarization of the NP.

The model was constructed to simulate the interface between the NP and its aqueous environment, making two key assumptions: (i) oxygen reduction occurs at the negatively charged surface[308,311], and (ii) the cleft between the NP and the neuronal membrane[247] is composed of a highly resistant protein medium. This model predicts the distribution of reduced oxygen ions and indicates the generation of a substantial electrical potential. It's important to note that this model does not account for the complex interactions at the neuron interface. However, the models suggest that the electrostatic depolarization of the second-order retinal neurons is driven by the pseudo capacitive charging of the NP.

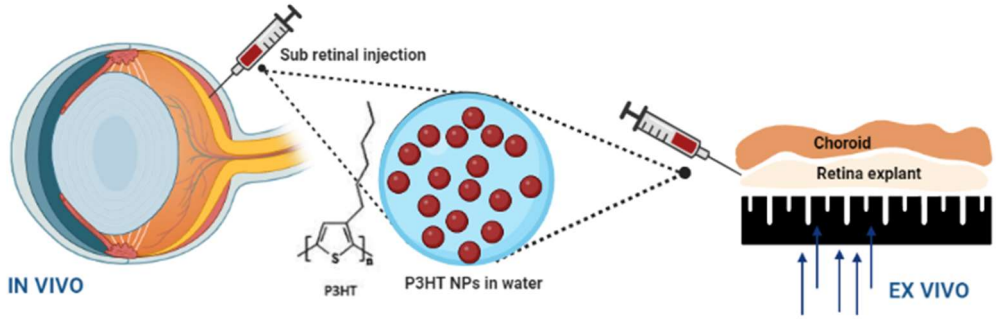

Figure 32. Schematic representation of acute v/s chronic NP exposure. Excised retinas from 15-month-old RCS rats were employed, in which P3HT-NPs were either subretinally injected *in vivo* or acutely administered to the retinal explant via microinjections between the outer nuclear layer and the choroid.

To assess the validity of the model, electrophysiological experiments were performed on dystrophic retinal explants of RCS rats, a model of RP[339]. P3HT NPs were either injected in the subretinal space of acute RCS retinal explants or injected *in vivo* in RCS rats to explant the retinas one month later and allow for a complete formation of the NP-bipolar cell interface **(Figure 32).** The extracellular activity of dystrophic retinas was investigated by multi-electrode array (MEA) experiments. The explants were layered in epiretinal configuration on the devices and subjected to illumination. As reported in **Figure 33,** the Peristimulus Time Histograms (PSTH) of the different experimental groups show a clear enhancement of the modulation of RGCs firing activity when NPs are administered *in vivo* with respect to an acute microinjection in the retina explant before the recordings. The comparison between firing rate (normalized to the baseline firing in the dark) of the RGCs in acute v/s chronic configurations results in a significant increase of the firing for the i*n vivo* injected retinas. These results indicate that, to fully elicit the maximum physiological effects, a prolonged NP-neuronal membrane contact is necessary *in vivo.*

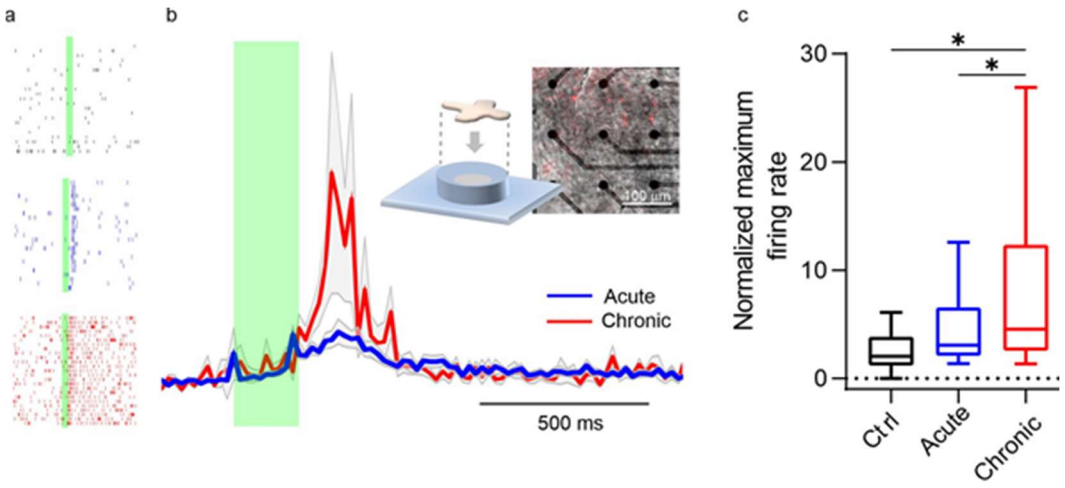

Figure 33. Chronic exposure to P3HT NPs *in vivo* exerts a stronger photostimulation in dystrophic retinal explants. (a) Representative raster plots of the time stamps of retinal ganglion cells firing upon light stimulation in control retinas (top) and retinas acutely and chronically treated with NPs (middle and bottom). The green bar depicts the duration of the light stimulation; (b) Time histogram (20 ms bin) of the normalized firing rate of acutely and chronically injected retina explants when illuminated for 200 ms at a light power density of 20 mW/mm^2 (λ = 530 nm). The inset shows a schematic representation of the experimental setup and the superimposition of a bright-field and fluorescence image of an explant on the MEA and the fluorescent NPs; (c) Quantification of the normalized maximum firing rate in ctrl, acutely and chronically injected explants showing an increased effect upon long-lasting contact of the particles with the retinal neurons in vivo (n = 19, 105, and 38 neurons for Ctrl, Acute and Chronic respectively from at least 5 animals; *p<0.05, one-way ANOVA/Tuckey's multiple comparisons test).

2.1.2 P3HT:PCBM NANOPARTICLES

SYNTHESIS AND PHYSICAL CHARACTERIZATION

Following the production of photosensitive P3HT NPs for direct neuronal stimulation described in the above section, efforts were directed towards enhancing the photo-transduction efficiency of these NPs by combining P3HT with a fullerene-derivative PCBM (P3HT:PCBM NPs), in order to achieve a donor-acceptor blend normally employed in organic photovoltaics technology[340]. The blending ratio between P3HT and PCBM was chosen to be 1:1, based on previous studies which highlight highest efficiency, driven by optimal balance between charge generation and separation at this ratio[341]. The co-polymer NPs were produced using reprecipitation method, wherein commercial polymers P3HT and PCBM were dissolved in THF at 10 mg/ml each (1:1 w/v) at 50 °C under magnetic stirring overnight. As described previously, a rapid injection of the polymers dissolved in THF was employed into sterile Milli-Q water, previously heated to 50 °C (1 parts in 9 parts). The obtained colloidal suspension was filtered through a sterile 0.45 µm PVDF syringe filter to remove the aggregates and obtain homogeneity.

A key step towards the clinical translation of NPs is fully understanding the interaction of the nanomaterial with biological systems. The nature of this interaction, in turn, depends heavily on the physicochemical properties of the NPs: such as hydrodynamic size, shape, roughness, surface charge, presence of targeting or bioactive moieties etc. In this regard, P3HT:PCBM NPs were characterized and compared to previously synthesised P3HT NPs in terms of size, polydispersity, morphology, and molecular signature (**Figure 34**). Since size evaluation is a critical parameter to determine the fate of the NP once in contact with neurons, the NPs were first characterized by transmission electron microscopy (TEM) for their size ad morphology. The TEM images confirm that the colloidal suspensions consist of discrete NPs which have smooth, spherical, and homogeneous populations. As P3HT is structurally heavier than PCBM, the areas containing the polymer exhibit increased electron scattering, resulting in a darker appearance in the TEM images[342,343], suggesting that the fabricated NPs have a P3HT rich core and PCBM rich shell[257,344]. The formation of PCBM around P3HT NPs aligns with a

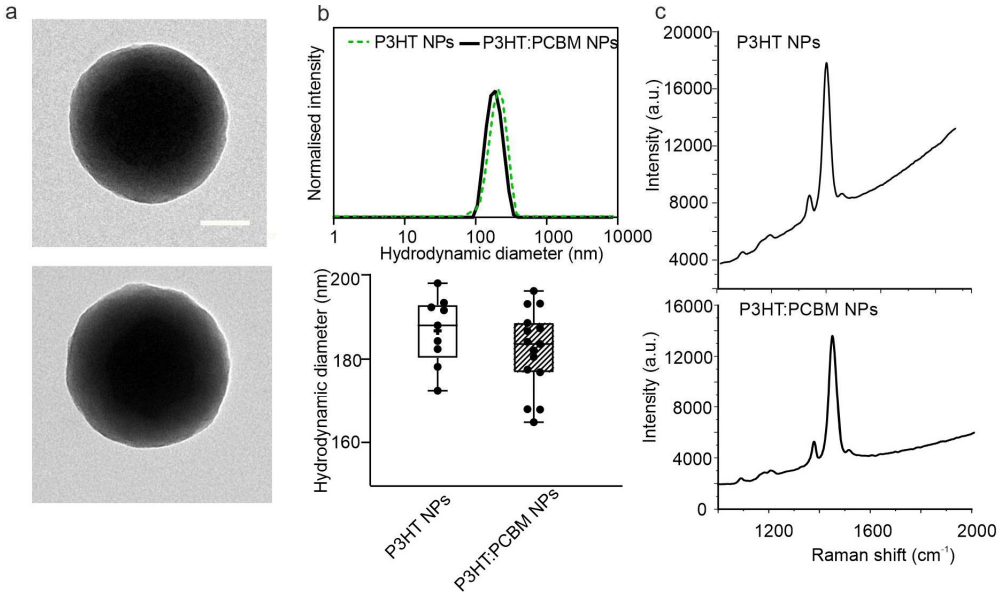

Figure 34. Polymeric NPs from P3HT and P3HT:PCBM show comparable size, polydispersity and stability. (a) Representative images of P3HT NPs (top), P3HT:PCBM NPs (bottom) acquired at the TEM (scale bar 50 nm); (b) Representative size distribution (top) and box plot diagrams (bottom) of the hydrodynamic diameter of the NPs acquired via DLS. (n = 9, 15 independent batches for P3HT and P3HT:PCBM NPs respectively); (c) Representative Raman spectra of both NPs acquired at 514 nm excitation.

nucleation and growth process consistent with the principles outlined in literature[345].

Consistent with TEM imaging, the evaluation done by Dynamic Light Scattering (DLS) technique, reveals that the P3HT and P3HT:PCBM NPs have comparable average hydrodynamic diameters (180 – 200 nm). Polydispersity index (pdI) gives a measure of particle size range distribution, i.e., degree of non-uniformity of a size distribution of particles. pdI closer to 1 suggests the presence of polydispersity, indicating the existence of multiple particle sizes within the populations (ISO 22412:2017)[346], while values lower than 0.4 are generally deemed suitable for monodisperse polymer-based NPs[347]. Both NPs synthesized show pdI values less than 0.08. Zeta potential is a measure of the

magnitude of electrostatic or charge repulsion/attraction between particles and is one of the fundamental parameters known to affect stability. A zeta potential of ±30 mV is generally chosen to deduce NP stability, with an absolute value greater than 30 mV indicates a stable solution whereas a low zeta potential value indicates a condition towards aggregation, instability, or coagulation. The average zeta potential measurements obtained were as follows: P3HT NPs -38 mV, P3HT:PCBM NPs -40 mV, thus indicating a stable colloidal suspension.

To complete the characterization process, the molecular spectra of the two NPs were obtained using Raman spectrometer (514 nm laser). P3HT yields a Raman spectrum with a sharp peak at 1375 cm^{-1} and the very intense and broad peak at 1450 cm^{-1} which are assigned to the C-C and the C=C skeletal stretching vibration respectively[348,349]. Other less intense peaks are observed at 1090 cm^{-1} (C-H bending), 1170 cm^{-1} (C_α-C_α symmetric stretching mode), 1210 cm^{-1} (a combination of C_α-C_α stretching and C_β-H stretching mode) and 1515 cm^{-1} (C_α=C_β antisymmetric stretch mode). The main peaks in the P3HT:PCBM spectra were observed at 1378, 1458 and 1516 cm^{-1}, as expected from literature[350].

INFLUENCE OF SYNTHESIS PARAMETERS ON NANOPARTICLE MORPHOLOGY

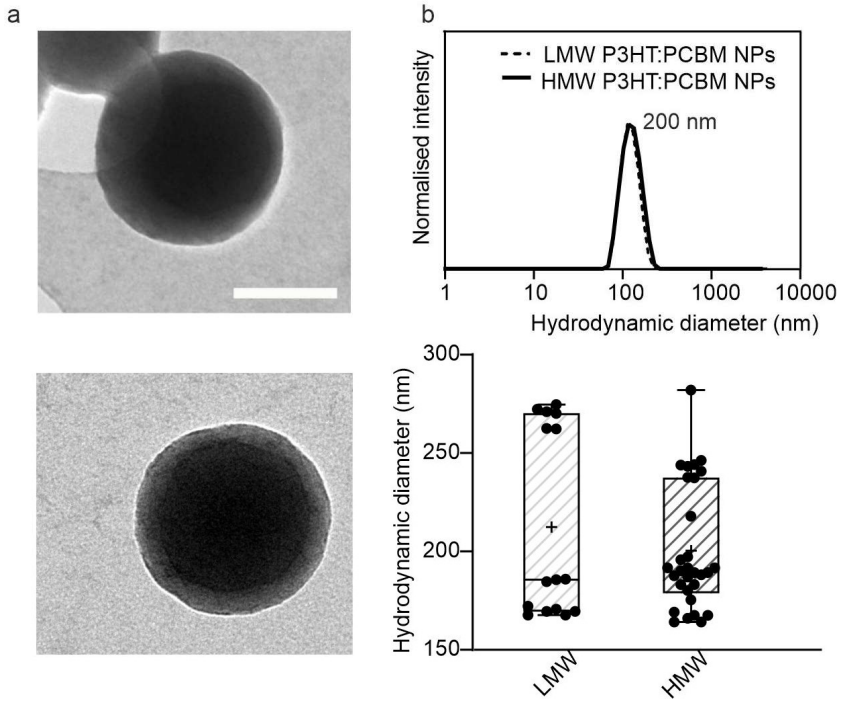

Figure 35. Impact of fabrication parameters: Varying molecular weight does not impact NP size. (a) Representative TEM images of P3HT:PCBM NPs synthesized with low molecular weight (top) and high molecular weight (bottom) P3HT, (scale bar 100 nm); (b) Representative size distribution (top) and box plot diagrams (bottom) of the hydrodynamic diameter of the NPs acquired via DLS (n = 5, 10 independent batches of LMW and HMW P3HT:PCBM NPs respectively).

a) Molecular weight

Extensive research has been conducted on the impact of P3HT molecular weight on surface morphology and charge transport[351–353]. It has been observed that the molecular weight of P3HT influences the structure of the active layer. This effect is partly due to solubility[354], with the solubility of P3HT declining as its molecular weight increases. Furthermore, molecular weight plays a role in the crystallization behavior, which also has a significant impact on morphology[355]. Higher molecular weights of P3HT result in increased crystallization behavior due to elevated π→π interactions, and this factor can strongly determine the ultimate nanomaterial morphology. On the other hand, low molecular weight (LMW) P3HT supports higher diffusion of PCBM, thereby allowing better formation of donor acceptor domains[356].

To assess if changing the molecular weight of P3HT, while keeping that of PCBM fixed, affects the physical characteristics, a prototype of P3HT:PCBM NPs was fabricated. For this preparation, LMW P3HT polymer (Mw: 16-20k g/mol) was utilized. The NP preparation was carried out under identical conditions, as followed for high molecular weight (HMW) P3HT:PCBM NPs (MW: 20-45k g/mol) and the two populations were tested through TEM and DLS. **Figure 35** shows no difference in the hydrodynamic diameter of the NPs prepared with LMW or HMW P3HT polymer. The NPs created from the 1:1 P3HT:PCBM blend using different molecular weights of P3HT all display similar size distributions (180 – 250 nm) with a pdI lower than 0.1. This indicates that, in the context of this study, molecular weight has minimal impact on NP size.

b) Polymer concentration

Amongst other fabrication parameters, influence of starting polymer concentration on organic photovoltaic device performance has also been investigated[341,357]. However, direct correlation studies between polymer concentration and NP morphology are limited[358]. In order to test the correlation of polymer starting concentration and NP morphology, P3HT:PCBM NPs were synthesized with the following concentrations of both polymers: 5, 10, 15 and 20 mg/ml. Bulk organization was analysed using TEM imaging and complementary information on size was tested using DLS. **Figure 36** shows varying polymer starting concentration does not cause a change in NP size. All populations have an average hydrodynamic diameter in the same range of previously reported results, showing little impact of starting polymer concentration on final NP size.

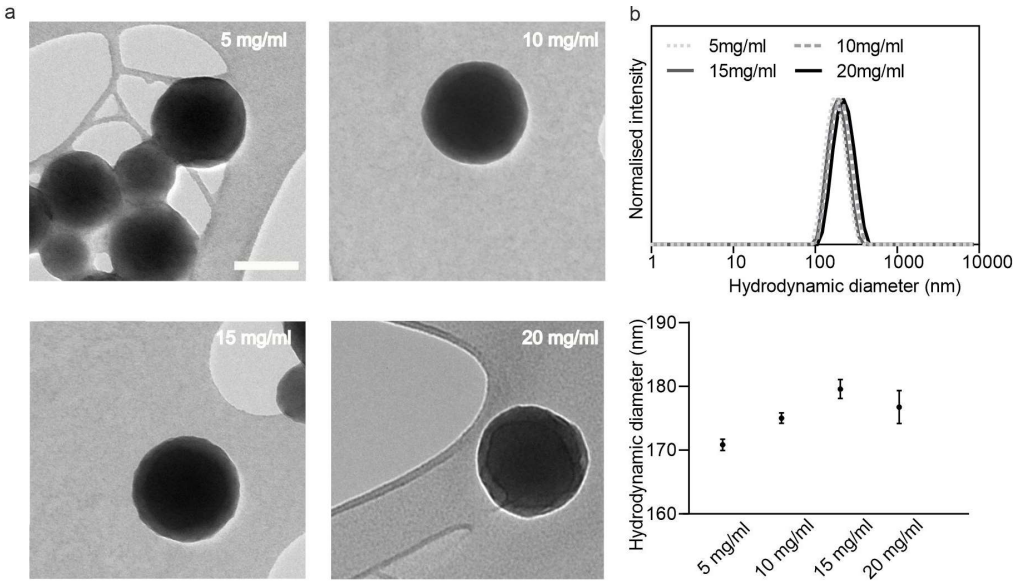

Figure 36. Impact of fabrication parameters: Varying polymer starting concentration does not influence NP size. (a) Representative TEM images of P3HT:PCBM NPs at different ratios of the two polymers: 5, 10, 15, 20 mg/ml (scale bar 100 nm); (b) Representative size distribution acquired via DLS as a function of the co-polymer starting concentration (n = 3). Data are the means ± sem. Increasing trend of NP size observed with a peak at 15 mg/ml polymer concentration.

2.1.3 P3HT:PCBM:GO NANOPARTICLES

SYNTHESIS AND PHYSICAL CHARACTERIZATION

Major efforts of this thesis were dedicated to characterizing new prototypes of NPs that combine the idea of the "liquid" retina technology and the potential of P3HT and graphene coupling. NPs were synthesized as a heterojunction of P3HT:PCBM and blended with graphene to investigate the possible improvement of charge separation upon illumination in dystrophic retinal explants.

As described previously, graphene-based materials, when blended with conjugated polymers, can be utilized for effective exciton separation and charge transport, owing to the large surface area available for donor-acceptor interface and continuous pathway for electron transfer. The work function of Graphene oxide (GO) (-4.5 eV) falls within the band gap of P3HT, and the inherent potential difference at the interface can enhance carrier mobility and photoinduced charge extraction[319,320]. P3HT:PCBM:GO NPs were fabricated by the reprecipitation method, as described by the following steps (**Figure 37**) 1) P3HT and PCBM were co-dissolved in THF at a concentration of 10 mg/ml each at 50°C under magnetic stirring overnight; 2) GO powder was dissolved in THF (10 mg/ml) and sonicated in a bath sonicator (100% power, 37 Hz, 20 °C, 2 hours). The sonicated sample was transferred to an Eppendorf tube, ultracentrifuged (12,700 rpm, 20 °C, 1 hour) in order to extract the graphene flakes with suitable dimensions (< 200 nm) to be encapsulated in the NPs, and the supernatant was collected; 3) an equal volume of supernatant was then mixed with the colloidal P3HT:PCBM mixture in THF at 50 °C (3-

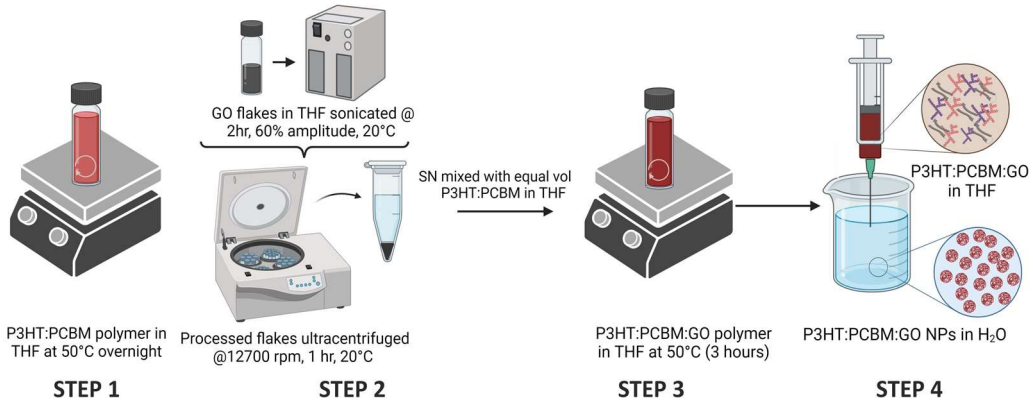

Figure 37. Pre-processing of GO flakes and synthesis of P3HT:PCBM:GO NPs via reprecipitation method. Synthesis protocol of the NPs, from the preparation of the co-polymer in THF (Step 1) to the sonication of the GO flakes and ultracentrifugation (Step 2) followed by the blend of flakes supernatant (SN) and co-polymer (Step 3), to the final reprecipitation in sterile water (Step 4).

hour, magnetic stirring); 4) the P3HT:PCBM:GO solutions were finally reprecipitated in sterile water to obtain the P3HT:PCBM:GO NPs colloids. The obtained suspension was filtered through sterile 0.45 µm PVDA syringe filter to remove the aggregates and obtain homogeneity.

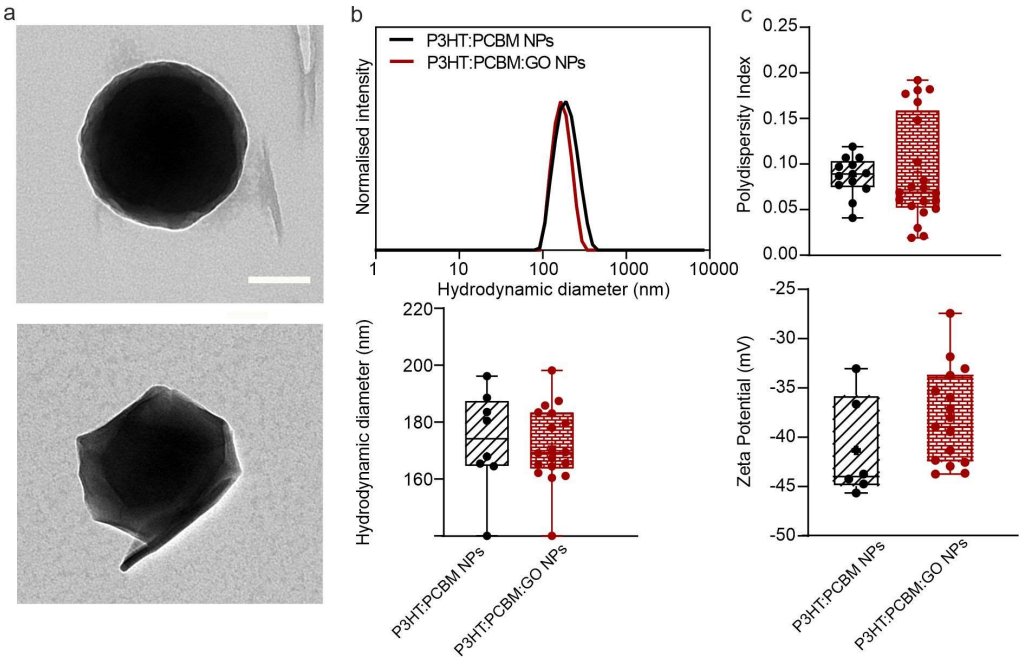

Figure 38. Characterization of hybrid graphene-enhanced conjugated polymer NPs. (a) Representative TEM images of P3HT:PCBM (top) and P3HT:PCBM:GO (bottom) NPs respectively (scale bar 100 nm) (b) Representative size distribution (top) and box plot diagrams (bottom) of the hydrodynamic diameter of the NPs acquired via DLS; (c) Polydispersity index (top) and zeta potential distribution (bottom) of the NPs. (n = 6, 15 independent batches of P3HT:PCBM and P3HT:PCBM:GO NPs respectively). The two kinds of NPs show comparable size and stability.

The NPs were subsequently characterized via TEM to assess the surface morphology and evaluate the success of GO encapsulation. When comparing the two NP suspensions, GO-enhanced NPs showed the typical polygonal shape of graphene flakes embedded in the NPs **(Figure 38 a)** with respect to the NPs without graphene. DLS measurements **(Figure 38 b, c)** indicate that both the NPs have comparable size (average hydrodynamic diameter 180 nm), pdI (average value <0.09) and stability (average zeta potential value -40 mV). This suggests that the NP population is relatively homogeneous in dispersity and shows high colloidal stability in aqueous media. Several batches of NPs with and without graphene were fabricated and analysed by TEM. Results confirm that the NPs tend to lose their sphericity upon graphene entrapment. This difference in overall NP shape was to be statistically significant **(Figure 39).**

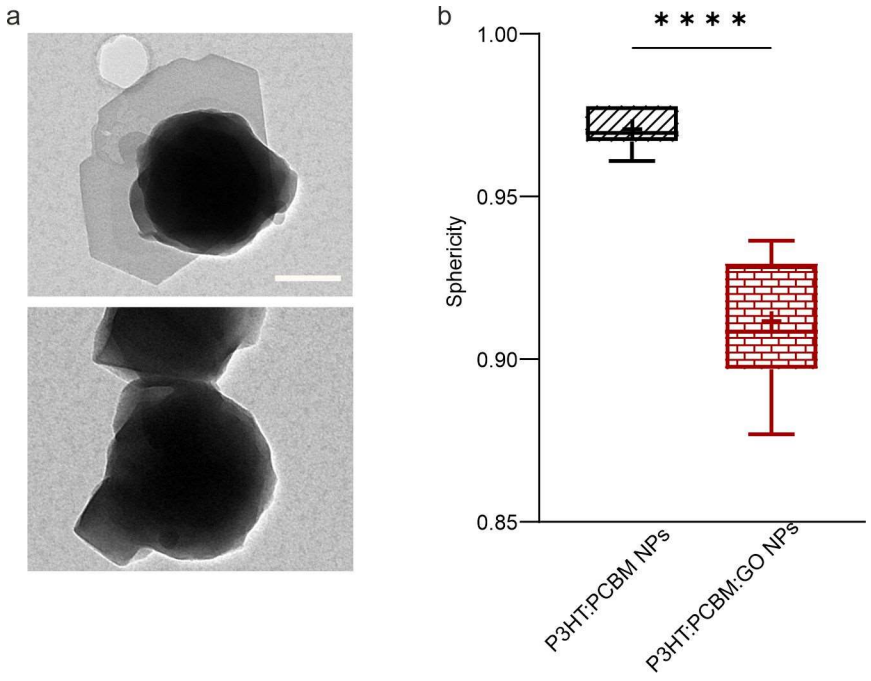

Figure 39. Graphene-enhanced NPs show typical polygonal shape and statistically significant loss of sphericity. (a) Representative TEM images of P3HT:PCBM NPs entrapping graphene flakes (scale bar 50 nm); (b) Sphericity analysis representing the differences in sphericity index between P3HT:PCBM and P3HT:PCBM:GO NPs (n = 7 for P3HT:PCBM and P3HT:PCBM:GO NPs from at least 7 independent batches, ****p<0.0001, Unpaired Student's *t*-test).

CONCENTRATION EVALUATION

Nanoparticle Tracking Analysis (NTA) is a complementary characterization technique to DLS, since both techniques measure same physical property[359,360]. This method operates by analysing individual particles separately, linking their displacement (due to Brownian motion) to their equivalent hydrodynamic diameter. As a result, it enables the rapid determination of high-resolution particle size distribution. In the following experiments, NTA was employed to assess the concentration of P3HT:PCBM and P3HT:PCBM:GO NPs **(Figure 40).** Both the NP populations had comparable concentration (5 x 10^9 particles/mL) and these results were consistent throughout different batches of

production. In addition, the size distribution of NPs closely resembled the results obtained from DLS.

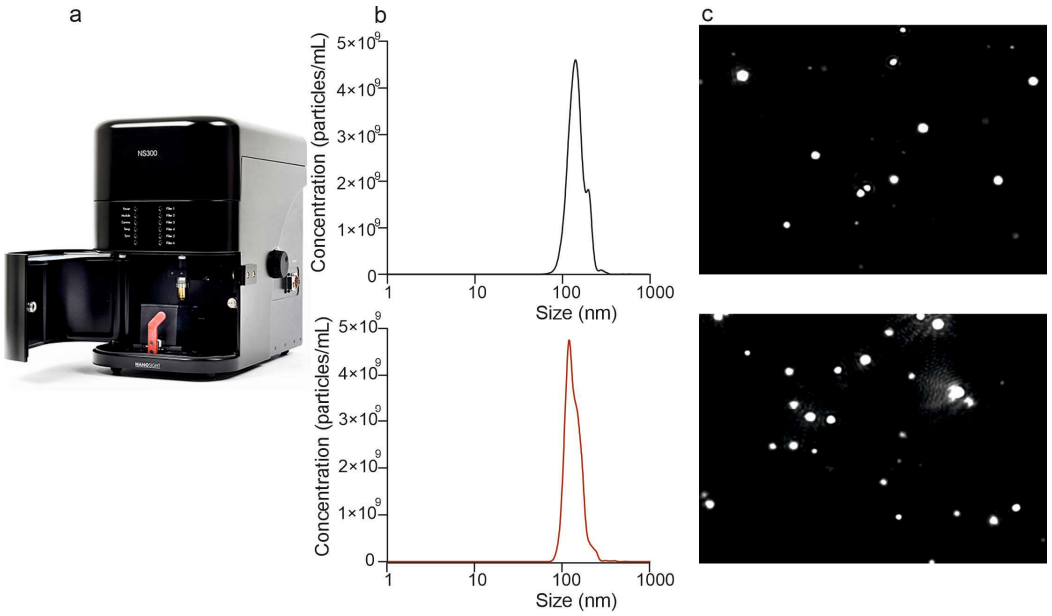

Figure 40. NPs with and without GO show comparable concentration. (a) Illustration of the Nanosight NS300, Nanoparticle Tracking Analysis device (Malvern Instruments Ltd, Worcestershire, UK); (b) Representative concentration plot against size for P3HT:PCBM NPs (top) and P3HT:PCBM:GO NPs (bottom) acquired with a 488 nm laser; (c) Corresponding NTA representative video frames for P3HT:PCBM NPs (top) and P3HT:PCBM:GO NPs (bottom).

NANOPARTICLE PURIFICATION

The polymers used in NP fabrication are recognized as safe considering their biocompatibility. It is necessary to ensure that the formulation contains low residual amounts of organic solvents, well within the safe concentration range according to International Council for Harmonisation guidelines[361]. For the purpose of quantifying THF content in synthesized NPs, Nuclear magnetic resonance (NMR) was employed. Different procedures were evaluated to assess the one allowing for the lowest amount of residual THF. The tested processes were the following: (i) a batch of NPs as it was produced to be used as a control; (ii) a batch of NPs left under the sterile hood evaporating overnight; (iii) a similar condition leaving the NPs overnight under a mild vacuum pumping system; (iv) a dialysed batch. The purification conditions were all similar in the final quantity of residual THF **(Figure 41)**. We finally chose the 'evaporation overnight under the sterile hood' as purification process for the future experiments, being the cheapest and most efficient. To assess the concentration of residual THF also after longer periods of purification, we evaluated the NPs solutions evaporated overnight up to 14 days, demonstrating that the residual THF can be considered completely exhausted after one week of purification.

a

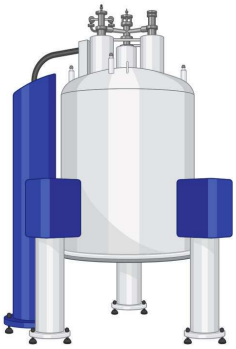

b

c

Treatment	Residual THF content (normalized to ctrl)
Open overnight	0.001 mM
Vacuum overnight	0.042 mM
Dialysed overnight	0.002 mM

Figure 41. NPs purified of organic solvent are safe for experiments in vitro. (a) Schematic representation of the Nuclear Magnetic Resonance spectroscopy machine for the analysis of the NPs. THF was quantified by PULCON method using the NMR standard dimethyl malonic acid as an external reference compound; (b) Schematic representation of the various conditions. (n = 3 independent NP batches); (c) Table showing the amount of residual THF remaining in the NPs batch after the overnight application of the 3 different treatments.

NANOPARTICLE STABILITY OVER TIME

Colloidal stability refers to the NP capacity to stay uniformly dispersed without forming aggregates. This aspect is critical at every stage: from design and production to storage, subsequent modifications, *in vitro* and *in vivo* evaluations, and eventual application[340]. The occurrence of aggregates, which are irregular NP clusters, can significantly alter the characteristics of the system and potentially result in the misinterpretation and inconsistency of experimental findings[341]. Colloidal stability of P3HT:PCBM and P3HT:PCBM NPs in complete medium was investigated by DLS and TEM. Good colloidal stability translates into potential prolonged circulation half-life *in vivo.* To investigate the NP behavior in biological medium, freshly prepared and filtered NPs were diluted 1:10 with sterile complete medium (Neurobasal media with supplements). The resulting samples were stored at 4 °C for over a month. At the time points of 1 day, 1 week and 1 month, aliquots were transferred and characterized. As a control, they were compared with NPs incubated in water. Size and zeta potential characterization was carried out using DLS and morphology was assessed using TEM. As can be seen in **Figure 42**, DLS intensity distribution remains virtually unchanged over time, indicating that the P3HT:PCBM and P3HT:PCBM:GO NPS are stable for at least 1 month at room temperature, both in water and biological media.

2.2 *IN VITRO* STUDIES WITH PRIMARY NEURONS

NEURONAL VIABILITY IN CONTACT WITH NANOPARTICLES

After the characterization of the newly synthesized NPs, cell viability assays were performed to test their biocompatibility with mouse primary hippocampal neurons. At 14 days *in vitro* (DIV), neurons were incubated with SiO_2 NPs, a sham non-photosensitive control particle of the same size of the photoactive ones, P3HT:PCBM, and P3HT:PCBM:GO NPs using different incubation intervals (1 day, 3 days, and 7 days). After the incubation phase, cell preparations were live-stained with (i) Calcein-AM, to label the cell bodies of viable cells; (ii) Propidium Iodide (PI), a non-membrane permeable marker

to mark dead or non-intact cells; and (iii) Hoechst, to stain the DNA of all the nuclei and thereby to count the total number of cells in the culture. The images were then acquired with an upright fluorescent microscope in the three fluorescence channels plus a bright field acquisition to further evaluate the morphology of the cultures **(Figure 43).** The cell viability was found to be comparable in all experimental incubation conditions and for all the experimental groups, control neurons, sham particles, P3HT:PCBM and P3HT:PCBM:GO NPs. These results demonstrate an excellent biocompatibility of the nanomaterials up to 7 DIV, paving the way towards their application *in vivo.*

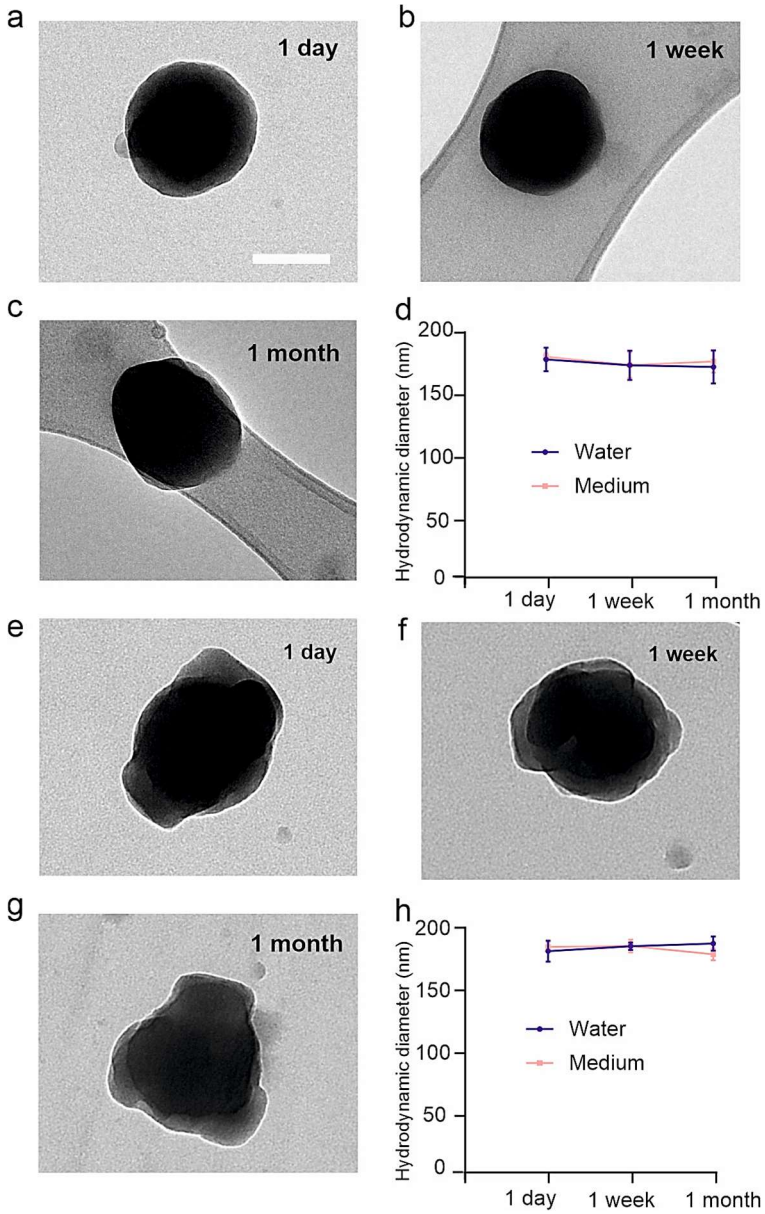

Figure 42. Conjugated polymeric NPs show colloidal stability in biological medium for at least 1 month. Representative TEM images of P3HT:PCBM (a,b,c) and P3HT:PCBM:GO NPs (e,f.g) acquired in biological medium at 1 day, 1 week and 1 month respectively (scale bar, 100 nm); Representative size distribution of the hydrodynamic diameter of the P3HT:PCBM (d) and P3HT:PCBM:GO NPs (h) acquired via DLS over time in water v/s biological medium (n = 3 independent batches).

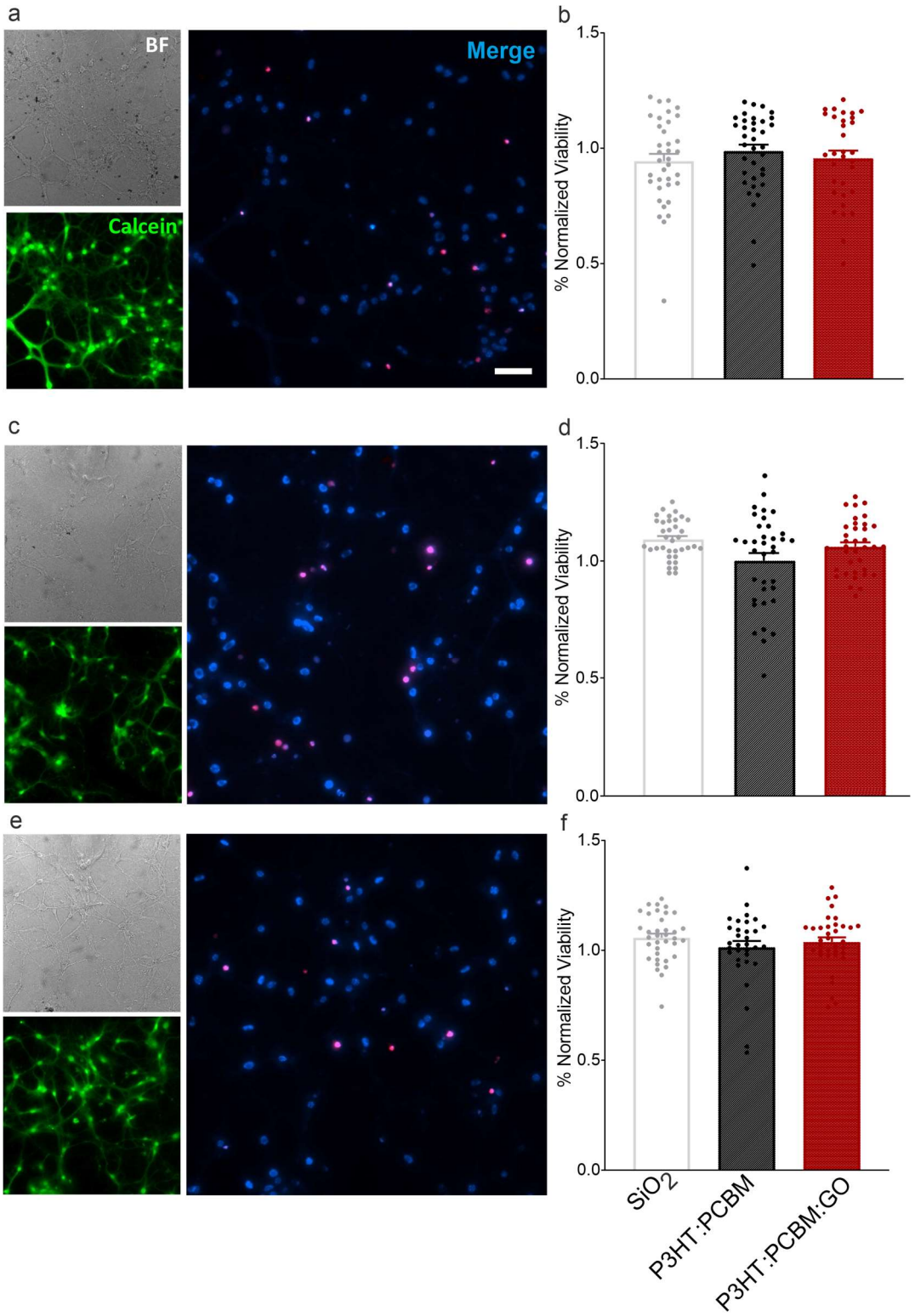

Figure 43. NPs do not interfere with neuronal viability up to 7 DIV. (a,c,e) Representative images of hippocampal neurons incubated for (a) 1, (c) 3 and (e) 7 days respectively with P3HT:PCBM:GO NPs. Each image triplet is composed by a Bright Field acquisition (grey), neurons stained with Calcein-AM (green), and the merge between the Hoechst staining for the nuclei (blue) and the PI staining for the dead cells (red) (scale bar 50 mm); (b,d,f) Bar graphs showing the percentage of normalized viability (normalized to the untreated control neurons) of primary neurons incubated with the different NPs at the three time points (1, 3 and 7 DIVs). The quantification in all conditions does not show significant interference of the nanomaterials with the viability of the neuronal cultures (n= 36, 36, 32 from 3 independent preparations).

NANOPARTICLES CO-LOCALIZE WITH NEURONAL MEMBRANE

An important feature of the NPs of the P3HT-based "liquid" retina is their ability to decorate the neuronal membrane without being internalized and by virtue of this localization, exert their photo-effect[247]. Therefore, the co-localization of the copolymeric NPs with the neuronal membranes was tested by live confocal imaging. Hippocampal neurons were incubated with P3HT:PCBM and P3HT:PCBM:GO NPs for different periods

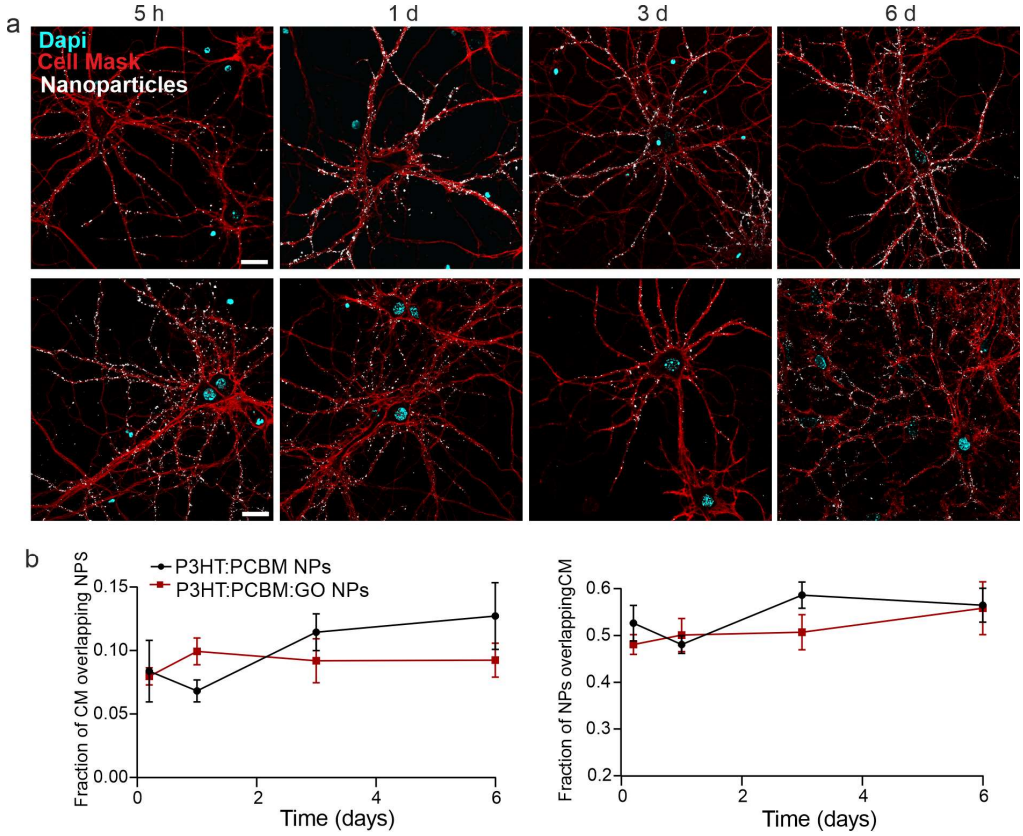

Figure 44. NPs decorate neuronal membranes without being up taken up to 6 DIV. (a) Representative confocal microscopy images showing primary hippocampal neurons grown on poly L-lysine coated glass (12 DIV) incubated with P3HT:PCBM NPS (top) and P3HT:PCBM:GO NPs (bottom), live-stained with Cell Mask (red) to label cell membrane and Hoechst (cyan) to stain cell nucleus. The NPs intrinsic fluorescence is shown in white. The images were acquired at different time points of 5 hours, 1, 3, and 6 days after incubation (scale bar 20 µm, n = 5 fields of view from at least 3 independent cultures); (b) Manders' coefficients analysis confirms that both NPs decorate the neuronal membrane without internalization up to 6 DIV.

of time (5 hours, 1 day, 3 days, and 6 days) and imaged upon Hoechst staining (cyan) and Cell Mask labelling for the membrane (red). The NPs were visible owing to the intrinsic fluorescence of the P3HT (white). The acquisition of z-stack images of the incubated neurons under all conditions allowed for the evaluation of Manders coefficients quantitating the fraction of NPs decorating the membrane and the fraction of membrane covered by NPs. As shown by the time course of the two coefficients in **Figure 44,** NPs are not internalized by neurons at any time-point, but instead they remain docked to the membrane, confirming their potential for photostimulation analogously to the P3HT NPs of the previous prototype of "liquid" retina.

2.3 NEURAL ACTIVITY MODULATION *EX VIVO*

MULTI-ELECTRODE ARRAY RECORDINGS ON DYSTROPHIC RETINAL EXPLANTS

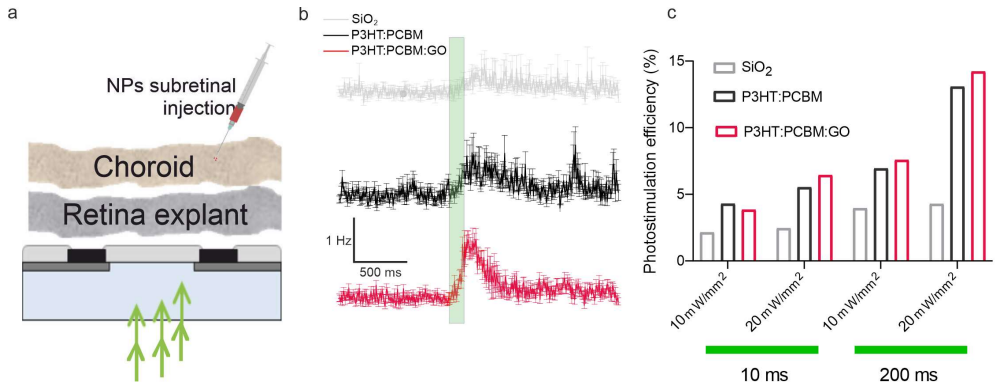

Figure 45. Effects of NPs on the light-evoked firing activity of RGCs from dystrophic rats. (a) Schematic representation of the NPs injection performed in aged RCS rats (12-15 months of age) between the choroid and the outer retina. Subsequently the retinal explant was positioned in epiretinal MEA configuration, with RGCs contacting the microelectrodes. Green arrows represent the direction of the light stimuli; (b) PSTH of the extracellular recordings of light-evoked multiunit activity of dystrophic retinal explants treated with the three NPs upon illumination at 200 ms and 20 mW/mm^2 and 540 nm. The vertical green bar represents the light stimulus (n= 600-700 neurons from at least 8 animals for each experimental group); (c) Photostimulation efficiency for all illumination conditions and NP types. The efficiency is calculated as the number of photoactivated electrodes with respect to the total number of electrodes active in the dark.

To examine the effect of NPs on the firing activity of the neurons upon illumination, the distinct NP preparations (P3HT:PCBM, P3HT:PCBM:GO, and SiO_2 that was used as control) were acutely injected in the subretinal space of retinal explants from 12-15-month-old rats, an age when the retina is already completely depleted of photoreceptors. Retinal explants were placed with RGCs on the surface of the MEA in strict contact with the microelectrodes. NPs were injected in the space between the bipolar cell layer at the level of the outer nuclear layer and the choroid. Using this injection method and thus maintaining the choroid during the dissection, NPs remain confined in the subretinal space, mimicking the NP distribution that would be achieved by a subretinal injection *in vivo* **(Figure 45 a).** The retinas were exposed to pulsed light at 0.25 Hz at different intensities (10 and 20 mW/mm^2, 540 nm LED source) and duration of the stimulation (10 and 200 ms). The overall multiunit firing activity recorded from RGCs upon illumination shows a peak of the activity right after the light stimulus in the case of P3HT:PCBM and P3HT:PCBM:GO NPs. No relevant effects are detected when sham particles are employed, if not a physiological residual response from intrinsically photosensitive RGCs that is always present independently of the treatment **(Figure 45 b).** Comparing the light-evoked responses from retinas treated with P3HT:PCBM and P3HT:PCBM:GO NPs, a clearly higher firing modulation is present in the time histogram of **Figure 45 b** in the case of NPs embedded with GO, giving a first clue that these NPs could represent a better photostimulation strategy with respect to the previous “liquid” retina. These results are confirmed by the efficiency of photo-evoked responses under the different

conditions **(Figure 45 c**). Photo stimulation efficiency was calculated as the percentage of *photoactive electrodes* with respect to *active electrodes*. Clearly, GO-embedded NPs show a trend of increased efficiency under all tested illumination conditions.

The firing modulation upon illumination was then compared among the experimental groups for each stimulation condition considering only the neurons with a firing modulation increase statistically different with the baseline in the dark. The weighted

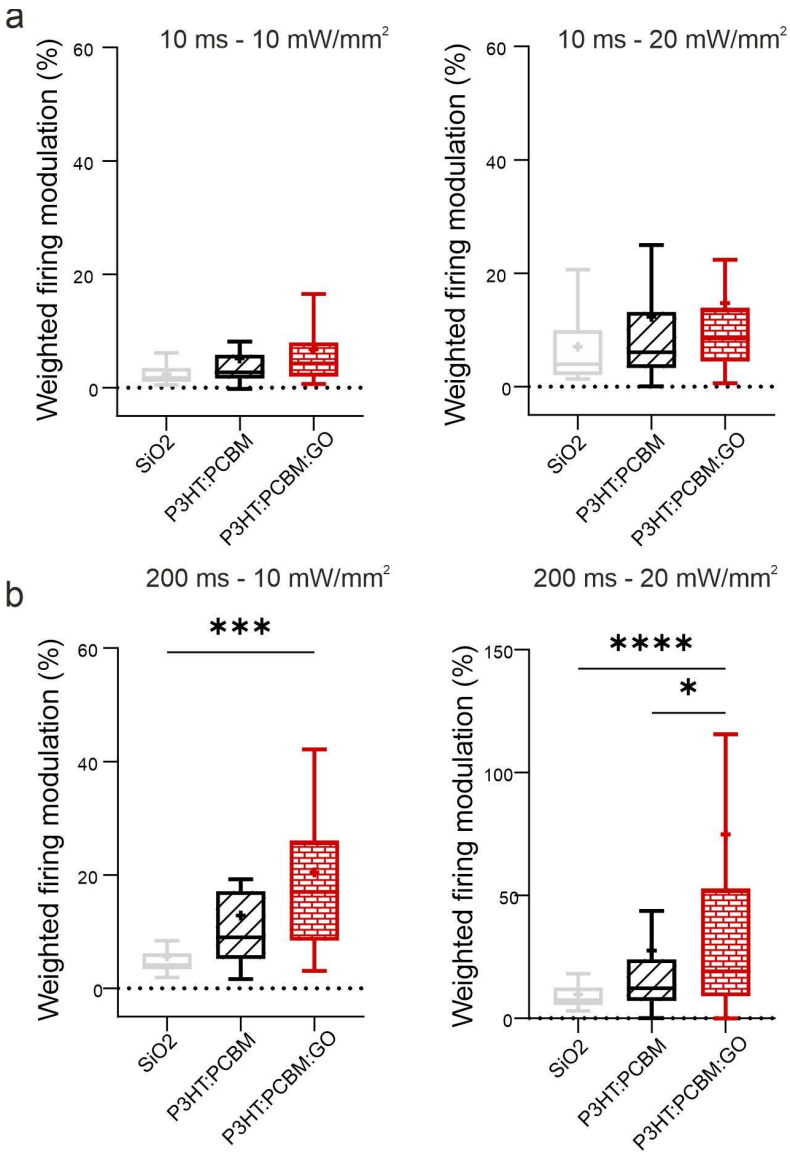

Figure 46. GO-embedded NPs mediate a stronger photostimulation of dystrophic retinal explants with respect to P3HT:PCBM NPs and controls. The firing modulation was calculated from the neurons having a statistically significant firing increase in the interval of time 1.73-2.33 s after the light onset with respect to the baseline firing. The so calculated modulation was further weighted on the number of active electrodes for each condition. (a) Weighted firing modulation evoked by 10 ms pulses at both 10 mW/mm^2 (left) and 20 mW/mm^2 (right) for the three types of NPs; (b) Weighted firing modulation evoked by 200 ms pulses at both 10 mW/mm^2 (left) and 20 mW/mm^2 (right) for the three types of NPs. (n=neurons from at least 8 animals for SiO_2, P3HT:PCBM, and P3HT;PCBM:GO respectively; 10 ms, 10 mW/mm^2, n=13, 24, 34; 10 ms, 20 mW/mm^2, n=14, 25, 50; 200 ms, 10 mW/mm^2, n=14, 22, 25; 200 ms, 20 mW/mm^2, n=26, 64, 118, *p<0.05, ***p<0.001, ****p<0001; one-way ANOVA/Tuckey's multiple comparison tests).

firing modulation is defined as the firing modulation with respect to the baseline in the dark, weighted on the number of active electrodes for each condition. This analysis strategy allows for the extension of the comparison to SiO_2 treated retinas, consisting of a very low number of photoactivated electrodes with respect to the other NPs treatments.

Figure 46 a shows that for 10 ms light pulses both P3HT- based NPs present an increase with respect to the sham NPs at both illumination intensities, while resulting in no statistical difference (one-way ANOVA). Although a trend of increasing firing modulation can already be seen in all tested conditions, a 200 ms light pulse duration causes a clear difference of firing modulation in favor of GO-embedded NPs, when compared to sham NPs (**Figure 46 b**). Additionally, at higher illumination duration and intensities, P3HT:PCBM:GO NPs also mediate a stronger, statistically significant photostimulation as compared to P3HT:PCM NPs.

This evidence represents a very important breakthrough for the development of an enhanced "liquid" retina, giving a first proof of an *ex vivo* light-evoked response at low light power and stimulus duration. The results in this section were performed in collaboration with other group members, and I curated the data analysis.

EXPERIMENTS IN PROGRESS IN VIVO

The following results have been adapted from the work of other group members (unpublished data), utilizing the NPs synthesized and characterized by me. An overview of the experiments provides important proof that NPs were well suited to rescue visual functions in an *in vivo* model of blindness as well as gives an insight into the future direction of work.

To evaluate the translational potential of the "liquid'' retina strategy, 10-month-old RCS rats with advanced stage RP were bilaterally injected with P3HT:PCBM:GO and sham NPs subretinally. This stage of the disease is characterized by complete retinal rewiring, drastic thinning, and absence of cortical responses to light, closely resembling late-stage RP patients. *In vivo* evaluation was carried out 30- or 60-days post subretinal injection, to allow complete recovery and integration of the NPs with the retinal tissue. Evaluation of the Pupillary Light Reflex, a subcortical response that can be considered an index of light sensitivity, and the light-dark box test, evaluating visually driven motor behavior, was performed. In the following section, results from the classical cue conditioning test, which show the reinstatement of cortical visual information processing, are presented. Classical cue conditioning involves linking the unconditioned stimulus (US) and conditioned stimulus (CS) through neural integration in higher brain centers that converge on the amygdala. Light-shock pairing engages more intricate and indirect fear conditioning pathways, including connections from the lateral geniculate nucleus to the V1/V2 cortex, visual association area TE2, perirhinal cortex, and ultimately, the amygdala[362] . During the conditioning session, the animals were initially placed in a dark chamber of the apparatus for a 2-minute habituation period. They were then exposed to a combination of a CS (represented by a light flash), and US (a mild foot shock). Following this training, the animals underwent a cue/perception test, where their

freezing behavior in response to the CS presentation was recorded (**Figure 47 b**). There were no noticeable differences in the acquisition of a conditioned fear response to the light stimulus, as the freezing response gradually increased during each CS + US pairing in all experimental groups. In the subsequent cued test, it was observed that healthy rdy rats displayed an increase in light-induced freezing behavior, indicating the establishment of implicit memory. However, untreated or SiO_2-NP injected rats did not exhibit any freezing response. Importantly, RCS rats that received P3HT:PCBM:GO NP injections showed a significant increase in light-induced freezing behavior, resembling the response of healthy rdy rats (**Figure 47 c**). The freezing behavior observed during the context test session, which served as a negative control, did not differ significantly among the experimental groups (**Figure 47 d**). In summary, the results demonstrate that conditioned responses, specifically light-induced freezing, which were present in healthy rdy rats and absent in sham-injected RCS rats, were restored to the level seen in healthy controls in RCS rats treated with P3HT:PCBM:GO NPs.

Taken together, these results show the feasibility of use of the newly synthesized co-polymeric NPs with GO flakes as subretinal therapeutic tool for vision restoration.

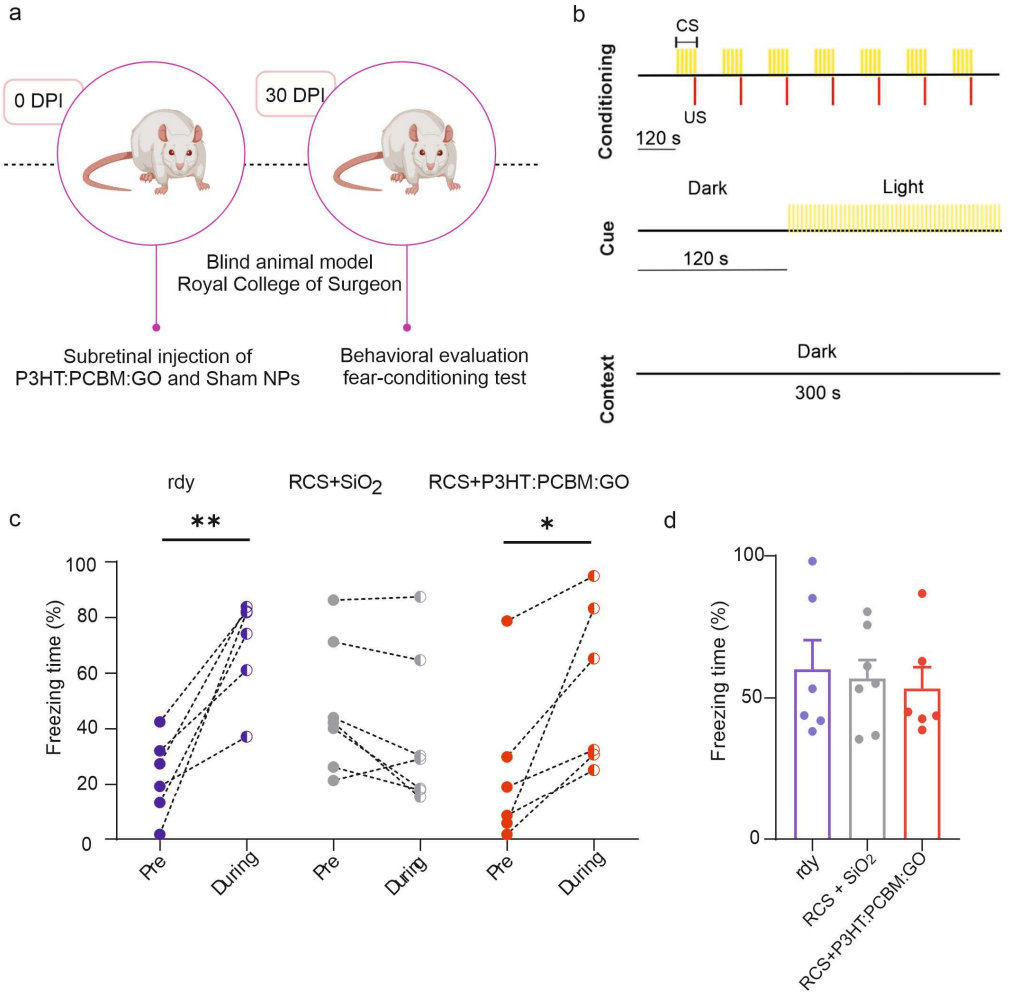

Figure 47. Recovery of light perception in aged RCS rats injected with P3HT:PCBM:GO NPs as assessed through classical conditioning. Schematic representation of (a) Experimental timeline of injection and behavioral analysis; (b) Protocols for conditioning cue and context. Top: During the conditioning session, rats were introduced in the dark chamber for a 2-minute habituation period, followed by 9 minutes of exposure to seven combinations of a conditioned stimulus (CS; light flashes at 5 Hz, see Methods) paired with an unconditioned stimulus (US; mild foot shock). Middle: During the cue test session, rats underwent 2-minute habituation in the dark to explore the novel context, after which they were presented with 3 minutes of CS. Bottom: During the context session, rats were placed in the dark for 5 minutes to explore the same context of the conditioning session without the presentation of the CS-US; (c) The light conditioned freezing behavior observed during the cue test session increased in healthy rdy and P3HT:PCBM:GO NPs injected RCS rats, while sham-injected RCS rats did not show any freezing response. ***p < 0.001, paired Student's *t*-test; (d) Freezing behavior recorded in the context test session did not differ among the experimental groups; sample size: n = 6, 7, 6 for rdy, RCS + SiO_2 and RCS + P3HT:PCBM:GO, respectively; one-way ANOVA/Tukey's tests.

3 DISCUSSION

Degenerative retinal pathologies, RP and AMD, share a common output: the progressive deterioration of retinal photoreceptors, ultimately resulting in blindness. Although extensive research has been conducted, a definitive cure for these conditions remains elusive. Therapeutic strategies can be classified into two main categories: preventive and restorative, each with its specific objectives and difficulties.

Preventive approaches, which include interventions like nutritional supplements, careful management of individual risk factors, anti-VEGF therapy for wet AMD and gene or cell therapies, are most effective when administered during the early stages of the disease. Their aim is to slow down photoreceptor degeneration or preserve the remaining functional photoreceptors. However, RP and AMD tend to present significant symptoms only in the advanced stages when most photoreceptors are already lost, rendering preventive strategies less practical.

In the later stages of these conditions, restorative approaches become the therapeutic gold standard. These strategies aim to replace the lost photoreceptor function through methods such as retinal cell transplantation, optogenetics, cell-based therapies, or surgical implantation of artificial retinal prostheses. However, retinal cell transplantation has encountered challenges including circuit rewiring and abnormal connections between graft and host tissue, resulting in limited success in terms of restored vision. Commercially available gene therapy is now accessible for RPE65-linked retinal dystrophies, and clinical trials are currently underway for a selected group of other RP-associated genes[363]. However, it is improbable that gene replacement therapy could comprehensively address the extensive genetic diversity of RP, which likely encompasses over 200 genes[364]. Optogenetics provides an alternative mutation-independent gene therapy approach that has been extensively evaluated in preclinical models. Recent reports have highlighted its effectiveness in one RP patient participating in an ongoing clinical trial[47]. The key benefit of optogenetic ion channel-based therapies is their temporal sensitivity and the potential for sequential high-frequency stimulation, crucial for normal vision in humans. However, this temporal sensitivity comes at the cost of light sensitivity. Most channels require intense light activation (10^{14} - 10^{17} photons cm^{-2} s^{-1})[365,366], which, particularly for certain opsins activated by shorter wavelengths, might surpass the safety limit of artificial radiation for the human retina (International Commission on Non-Ionizing Radiation Protection, 2013[367]). To address this, "red shifting" these ion channels to safer, longer wavelengths could be of interest, in addition to engineering precisely targeting optogenetic tools to distinct subcellular regions and specific subsets of cells. In parallel, various cell-based strategies are in the experimental stages or in the early phases of human trials, demonstrating the continued exploration of innovative solutions for retinal dystrophies[368,369].

Among restorative approaches, retinal prosthetics hold the most promise. They are designed to stimulate the inner retinal neurons that are not primarily affected by the degeneration and are typically utilized during the later stages of the disease. These involve the surgical insertion of prosthetic devices within the eye, employing different configurations like epiretinal, subretinal, or suprachoroidal placements. Presently,

majority of systems rely on electrical stimulation, while a limited number, emerging in recent years, employ photovoltaic stimulation.

In this context, organic prosthetics utilizing conjugated polymers offer a promising avenue to address the shortcomings of existing market devices like the ARGUS II® or Alpha AMS. Owing to their inherent light-sensitivity, photovoltaic functionality, unique biocompatibility, flexibility and easy surface functionalization, photosensitive semiconducting polymers have proven to be efficient neuromodulation tools for the recovery of neural diseases. The utilization of organic materials eliminates the need for inorganic components, external power sources, cameras, and bulky eyewear. Invasive surgical interventions become unnecessary with the adoption of a fully organic, self-contained, and photosensitive device lacking traditional pixel limitations. Rapid and straightforward administration directly into the patient's eye becomes feasible, marking a significant leap forward in the field. The use of conjugated polymers presents a promising avenue to enhance the effectiveness of retinal prosthetic devices, potentially leading to significant vision restoration outcomes.

Among the several conjugated polymers available, the most studied and used in the field of retinal prostheses is thiophene and its derivatives, in particular P3HT. Over the past decade, research groups at the IIT in Genoa and Milan have conducted a series of experiments involving the interaction of P3HT with cells and tissues. These experiments have predominantly focused on electrophysiology, wherein neurons or cell lines were cultivated on P3HT-only layers or layers consisting of P3HT mixed with electron-acceptor materials. These investigations have explored various parameters such as biocompatibility, cellular viability, physiological responses, and effects of photostimulation upon illumination. The outcomes of these studies have indicated a high level of biocompatibility associated with P3HT, as well as modulation of cellular firing in response to light stimulation, with a notable level of spatial and temporal precision able to restore light sensitivity and visual acuity in a rat model of RP *in vivo*.

Building upon these promising findings, a nanoscale version of the organic prosthetics has been proposed and successfully tested for visual restoration both in early and late stages of photoreceptor degeneration and retinal rewiring *in vivo*. However, light-sensitivity and the power intensities in play needed to achieve a reasonable photomodulation of the residual inner neurons still represent a challenge. In an attempt to address this challenge, this work aims to exploit and enhance the potential of the “liquid” retina technology.

In this framework, this thesis provides an account of design and synthesis of semiconducting conjugated polymeric NPs and proposes a novel approach to couple them with graphene to improve the phototransduction process. The experiments provide a detailed synthesis of NPs via reprecipitation method and characterization using dynamic light scattering technique, electron microscopy, and nanoparticle tracking analysis.

The mechanism of charge separation in P3HT NPs and their photo stimulation action were investigated by 1-D and 2-D simulations. The model suggests that the spatial range

of the electrical potential generated at NP surface is capable of capacitively depolarizing the membrane of second-order retinal neurons. It was found that the pseudo-capacitive charging of the NPs responsible for the electrostatic coupling is appreciable only in the presence of a highly resistive cleft, where ionic screening is negligibly small. If this condition is verified, even physiological light intensities (0.2 W/m^2) can induce appreciable depolarization of the neurons. The highly resistive medium filling the cleft is ascribed to the presence of adhesion proteins extruding the membrane or coating the NP. Therefore, the formation of "proteinic islands" is suggested by the model as a fundamental ingredient to ensure the coupling among neurons and NPs at low light intensities. This introduces the concept of a diffuse soft interface at variance with the sharp boundary brought about by a metal electrode, validating the use of an organic semiconductor. The photoexcited NPs facilitate space charge-induced polarization, which is detectable by the surrounding environment because of the decreased dielectric screening in the cleft. This allows them to function as a floating element in an open circuit.

The difference in the response of chronic and acute implants can be ascribed to the distinct interface conditions which are established at the NP/bipolar cell contacts. When the injection is performed *in vivo* one month before the explant, in addition to the complete formation of the tight NP-cell interface, different environmental and bio-physical conditions lead to the formation of a protein corona on the surface of the NPs which enhances the resistive nature of the cleft. These results support the model described above, particularly the role of the proteins in the cleft, and are consistent with the observed difference in light sensitivity between *in vivo* and *ex vivo* testing. A prolonged *in vivo* contact between NPs and neurons is thus necessary to build up a functional hybrid interface and fully elicit the physiological effects.

To enhance the NP photo-transduction efficiency, donor-acceptor copolymeric P3HT:PCBM NPs were synthesized under sterility. The physical characterization performed using TEM and DLS demonstrate a spherical, monodisperse population sized ≈ 180 – 200 nm, with a core-shell like morphology. The impact of polymer molecular weight and starting concentration on NP morphology was tested. Fabricated NPs show no significant differences in terms of size, polydispersity, and zeta potential. This can be ascribed to overlapping and wide molecular weight distribution of polymer batches used. Moreover, studies showing significant impact of the polymer starting concentration on NP size have previously employed concentrations varying by factor of tens[358].

Operational functionality of conjugated polymers strongly depends on efficient charge transport and charge separation characteristics with high carrier mobility. In photovoltaic systems, excitons generated upon photon absorption need to be disassociated into free electrons and free holes at the donor-acceptor interface. Addition of optimum graphene content to the polymer mix can achieve effective exciton separation and charge transport, owing to the large surface area available for donor-acceptor interface and continuous pathway for electron transfer. With the aim of synthesizing optimized NPs with enhanced photovoltaic properties, P3HT:PCBM:GO NPs were fabricated using

reprecipitation method and characterized. TEM images confirm the embedding of GO flakes in the NPs and subsequent analysis indicate that the loss of NP sphericity was statistically significant. The nano tracking analysis revealed the NPs to have an average concentration of 5 x 10^9 NPs/mL.

Furthermore, in order to ensure removal of the organic solvent in the obtained NP aqueous suspension, various purification techniques were adopted, and the most time and cost-efficient solution was chosen (leaving the eppendorf open overnight under sterile hood). Short- and long-term stability of the NPs was assessed in cellular medium for up to 1 month. The results showed that the nanomaterials do not show any significant increase in size over time, both in aqueous and biological media.

Cell viability tests were carried out with primary neurons incubated with P3HT:PCBM or P3HT:PCBM:GO NPs for 1, 3, 7 days post incubation. Comparison with sham NPs (Silica), demonstrated minimal interaction of the novel materials with physiological cell viability, and no induction of stress, damage, or death. Additionally, a co-localization test indicated that the NPs predominantly adhered to the cellular membrane without being endocytosed, a fundamental feature for the photostimulation to occur efficiently.

Ex vivo experiments on dystrophic retinal explants using MEAs demonstrated that an acute subretinal injection of P3HT:PCBM:GO NPs resulted in a sustained increase of firing modulation upon illumination with respect to P3HT NPs (alone or in combination with PCBM) or control particles, even at low stimulus durations and power intensities. This confirms the higher performance of graphene entrapped NPs as compared to the NPs without graphene.

The translational potential of the “liquid’’ retina strategy was evaluated by subretinally injection of the P3HT:PCBM:GO NPs in 10-month-old RCS rats with advanced stage RP, exhibiting a fully degenerated and aged retina. This experimental model proves to be very interesting for evaluating the potential translatability of this strategy in treating patients with advanced stages of RP, when natural vision is replaced by total blindness. When compared to the early stages of photoreceptor degeneration, 10-month-old RCS rats exhibited intricate morphological and circuit rearrangements in the inner retina, including significant displacement and misorientation of bipolar cells and horizontal cells, despite maintaining a substantially preserved molecular phenotype in the inner retina. Although there was profound remodeling observed in the aged dystrophic retina, the visual activities in RCS rats were found to recover drastically. Preliminary results show that the NPs demonstrate the capacity to partially recover visual acuity and reactivate the creation of light-induced implicit memory traces that are integrated across multiple cortical levels. In addition to this, various parameters, including light sensitivity assessed through the subcortical pupillary reflex, light-escape behavior, and VEP amplitude, were all restored to the levels observed in age-matched healthy rats.

In conclusion, the graphene-based co-polymeric NPs showcased a good biocompatibility with neurons and kept their localization in the proximity of the cell membrane up to 7 days *in vitro*. The photo-modulation induced by the novel NPs on dystrophic retinal explants is stronger in presence of graphene and is enhanced in terms of sensitivity with

respect to the previous prototype of “liquid” retina prosthesis. These results suggest that these novel NPs could offer greater efficiency in therapeutic approaches targeting degenerative retinal conditions like RP and AMD, paving the way towards more effective strategies in the field of restorative retinal therapies.

4 MATERIALS AND METHODS

4.1 NANOPARTICLE SYNTHESIS

P3HT/P3HT:PCBM NPs

P3HT (Mw: 20-45k g/mol, Sigma-Aldrich) was dissolved in THF (Sigma-Aldrich) (10mg/ml) at 50°C under magnetic stirring (3 hours). The P3HT NPs were obtained using reprecipitation method, where a rapid, single injection of the polymeric solution was dropped in sterile Milli-Q water (previously heated to 50°C) in 1:10 v/v ratio. The resultant colloidal solution was filtered through a 0.45 µm pore filter to remove the aggregates and obtain homogeneity. In case of P3HT:PCBM NPs, a 1:1 (w/v) solution of both the polymers was co-dissolved in THF, followed by the same method for synthesis as for P3HT NPs. The NP preparation was carried out in identical conditions also for the low molecular weight prototype of P3HT:PCBM NPs (P3HT Mw: 16-20k, Rieki Metals).

P3HT:PCBM:GO NPs

Reprecipitation method was followed wherein P3HT and PCBM were co-dissolved in THF at a concentration of 10 mg/ml each at 50°C under magnetic stirring overnight. Meanwhile, graphene oxide powder (Sigma-Aldrich) was dissolved in THF (10 mg/ml) and sonicated in a bath sonicator (100% power, 37 Hz, 20°C, 2 hours). The sonicated sample was transferred to an Eppendorf tube, ultracentrifuged (12700 rpm, 20°C, 1 hour), and the supernatant containing the fraction of GO with a size compatible with NPs encapsulation was collected. The supernatant was then added to the co-polymeric blend in a 1:1 v/v ratio. The P3HT:PCBM:GO suspension was kept at 50 °C under magnetic stirring for 2-3 hours and the NPs were reprecipitated in sterile water (milli-Q) in 1:10 v/v ratio and finally vacuum filtered (0.45 µm filter pores). Before use with biological preparation the NPs were subjected to a further centrifugation step in order to achieve the desired concentration. As a sham control, SiO_2 NPs (Microparticles GmbH) of comparable size were used.

4.2 NANOPARTICLE CHARACTERIZATION

Transmission electron microscopy

TEM is undoubtedly the most versatile characterization technique for NPs[370]. Upon interaction with the sample, the high-energy electron beam is diffracted from the axis at certain angles and transmitted at other angles. The obtained signal provides images allowing detailed visualization of the sample with atomic resolution. TEM enables investigation of shape, size and crystal structure at single particle level, down to 0.05 – 0.1 nm, by reducing image distortion. For TEM imaging, a 5 µL drop of the NP suspension was placed on Cu grid, 150 mesh coated with ultrathin holey carbon film (Sigma-Aldrich) and imaged using the JEOL 1011 transmission electron microscope operated at 100 kV.

Dynamic light scattering

DLS measures particle size based on Tyndall scattering and Brownian diffusion. The measurement cell contains the diluted NP suspension, which is subjected to coherent monochromatic radiation from a laser source[371]. Owing to their inherent Brownian motion, the NPs move randomly in space with a diffusion coefficient that depends on their hydrodynamic diameter. The detected scatter intensity fluctuates over time depending on NP size. The degree of autocorrelation of these signals is used to infer the NP size distribution[372], which can be represented in terms of intensity, volume, or number. Intensity distribution is the most common representation. However, the scattering intensity of a particle is proportional to its size to the sixth power; this means that the resulting size distribution is strongly biased toward larger particles and aggregates. Volume and, to a greater degree, number distributions rely on mathematical functions that partially correct for this bias. This often results in smaller particle sizes for volume and number distribution derived measurements, compared to those calculated from intensity distribution.

DLS measurements were performed with Zetasizer NanoZS (Malvern Instruments, Ltd., United Kingdom) on freshly prepared NPs suspension further diluted 1:10 in Milli-Q water and transferred into a single-use polystyrene half-micro cuvettes (Fisher Emergo, Landsmeer, The Netherlands) with a pathlength of 10 mm. The measurements were made at a position of 4.65 mm from the cuvette wall with an automatic attenuator and at a controlled temperature of 25°, using a 50-mW laser at 638 nm wavelength as a light source. For each sample, measurements were recorded at 173° (backscatter) detection angle and carried out in automatic mode. The results are reported as a mean of three runs, where each mean represents the average value of 10 measurements per run. The intensity size distribution, the Z-average diameter and the polydispersity index (PdI, measure of particle size range distribution) were obtained from the autocorrelation function using the “general purpose mode”. The error bars displayed on the DLS graphs were obtained by the standard deviation (SD) of three measurements of the same sample.

Electrophoretic light scattering

The surface charge of NPs is a key determinant of their interaction with biological systems. In complex biological fluids surface charge influences both the rate of formation and the identity of the protein corona. Once the NPs are in contact with cells, surface charge affects their interaction with the cell membrane and their internalization[373]. Z-potential is often used as an approximation for NPs surface charge, and it is commonly measured via ELS. ELS is based on dynamic light scattering, but during ELS the movement of the NPs in the detection volume is due to the electrophoretic flow of the NPs rather than their Brownian motion. A suspension of NPs in a solvent of known refractive index is subjected to electric field. The NPs move randomly and acquire a net surface charge. This attracts an increased concentration of oppositely charged ions near the NP surface, leading to the formation of two layers; stern (strongly bound ions) and diffuse (loosely bound ions) layer. Z-potential is the potential at the slipping plane, which is the interface between the double layer that forms around solvated nanoparticles and the bulk of the

electrolyte. It depends on the net charge and the size of all that is included within the slipping plane. The Z-potential of NPs depends therefore on many factors: temperature, viscosity of the solvent, ionic strength, and composition of the electrolyte. Determination of Z-potential gives a measure of electrostatic attraction or repulsion between NPs, and it is considered a crucial indicator for stability. NPs with a Z-potential value between -10 to +10 mV are considered neutral (hence prone to aggregation) while NPS with a Z-potential value of greater than +30 or less than -30 mV are considered strongly cationic and anionic respectively, thus possessing a high degree of physical stability. Z-potential measurements were carried out using the DLS (Zetasizer NanoZS Malvern Instruments, Ltd., United Kingdom) on freshly prepared NPs suspension diluted 1:10 in Milli-Q water and transferred into disposable cells (DTS 1070, Malvern). After visual inspection for absence of air bubbles, a measurement cell was placed in the apparatus and an equilibration time of 120 seconds was chosen. The measurements were made at a controlled temperature of 25 °C, using a 633 nm wavelength laser source at a scattered angle of 13°.

Nanoparticle Tracking Analysis

Similar to DLS, NTA provides a non-destructive size characterization based on measuring particle diffusion[360]. It employs a camera to record videos of particles moving under Brownian motion, thus analysing several particles individually as well as simultaneously. NTA provides an account of high-resolution hydrodynamic diameter, count-based concentration as well as aggregation measurement. It is particularly useful for characterization of highly polydisperse samples. All NTA measurements were performed on a Nanosight NS300 (Malvern Instruments Ltd, Worcestershire, UK), equipped with a 488 nm laser and a scientific CMOS camera. NTA 3.2 software was used for instrument control and data analysis. The data was collected in the form of 60-second videos captured by the camera. The sample chamber was maintained at 25 °C and a syringe pump was used to keep a continuous flow of sample through the flow cell at 300 µL/min for the duration of measurement. For each individual sample, settings (screen gain, camera level, and focus) were manually adjusted to optimize visualization of the particles and thereafter kept identical for all video repetitions of the same sample. The detection threshold, which determined the minimal brightness of pixels to be considered for tracking, was also adjusted post-acquisition to minimize noise as well as to maintain a particle-per-frame count appropriate for analysis (10–120 particles per frame). Settings were kept consistent for all video repetitions of the same sample.

4.3 NANOPARTICLES IN PRIMARY HIPPOCAMPAL NEURONS

PRIMARY NEURON CULTURES

WT C57BL/6 J (Charles River) mice were sacrificed by CO_2 inhalation and cervical dislocation, and 17/18-day embryos were promptly removed by cesarean section. Briefly, hippocampi were dissociated and incubated in 0.125% trypsin for 15 min at 37 °C for enzymatic digestion. Cells were then mechanically dissociated with a fire-polished

Pasteur pipette. Trypsin activity was inhibited by adding Neurobasal medium (ThermoFisher Scientific) supplemented with 2 % B27, 1 % GlutaMax, 1 % penicillin/streptomycin (complete medium), and 10 % fetal bovine serum. After digestion, neurons were washed in complete medium, centrifuged at 700 RPM for 5 minutes, and resuspended in complete medium at the desired concentration. Cell viability was determined by Trypan Blue exclusion assay. All animal manipulations comply with European and Italian regulations (Directive 2010/63/EU of March 4, 2014).

NEURONAL VIABILITY

NPs underwent concentration and solvent removal before incubation with primary neurons. Multiple Eppendorf tubes, each containing 1 mL suspension of NPs, were kept overnight under sterile hood to ensure THF evaporation. The following day, remaining 800 µL of suspension was ultracentrifuged for 20 minutes at 12,700 RPM, 20 °C. 50 µL of the concentrated pellet was retrieved which was used for further experiments *in vitro*.

Mouse primary hippocampal neurons were incubated at 14 DIV with SiO_2, P3HT:PCBM, and P3HT:PCBM:GO NPs (5 µL/2 mL), each NP in different incubation intervals (1 day, 3 days, and 7 days). The cells were then live stained for 3 minutes at room temperature with a solution made by different markers: propidium iodide (PI, 1 µM, ThermoFisher Scientific), Hoechst 33342 (Hoechst, 1 µM, ThermoFisher Scientific) and Calcein AM (2 µM, ThermoFisher Scientific). PI was employed to stain the dead cells, Hoechst facilitated the visualization of the cell and Calcein (permeant to live cells) was used to both to cross-check whether cells were alive and to detect, from morphology, any astrocytes in culture. Quantification of cell viability was performed at 10x magnification using a Nikon Eclipse Ni-U upright epifluorescence microscope (Nikon, Tokyo, Japan), with random sampling of 3 non-overlapping regions of interest (430 x 430 µm) per sample (3 samples per culture, n = 3 independent cultures). The number of PI-positive cells with respect to the total number of Hoechst-positive cells, was calculated for each sample as a cell viability index. Image analysis was performed using the ImageJ/ Fiji (NIH, USA) Analyze Particle tool.

CO-LOCALIZATION STUDY

Primary mouse hippocampal neurons were seeded at density 25000 cells/well in 12 well plates (Corning Inc.) and incubated in standard conditions. At 12 DIV, neurons were incubated with P3HT:PCBM or P3HT:PCBM:GO NPs (5 µL/ 2 mL) for 5 hours, 1-, 3- or 6 days before checking for NP distribution and co-localization. Cells were live stained for 5 minutes at room temperature with CellMask™ Deep Red (1 µL/mL, Life Technologies), an amphipathic molecule providing a lipophilic moiety for membrane loading, and Hoechst (3.33 µL/mL) for nuclei visualization. After incubation at 37 °C at the different experimental time points, neurons were live imaged with the help of the intrinsic P3HT fluorescence (λ_{ex}, 514 nm; λ_{em}, 600-650 nm). Distribution and co-localization of NPs with neuronal cells was acquired at 40x (NA 1.3) magnification, via Z-stacking at 1024 × 1024 resolution, using a Leica SP8 inverted confocal microscope (SP8, Leica Microsystems GmbH, Wetzlar, Germany) with the Leica Las X software. For each sample, five fixed regions of interest were selected per sample (5 samples per culture, n = at least 3

independent cultures). The representative images shown in this thesis were obtained through the projection of each z-stack fluorescence value on a single plane (z-max projection). Images were elaborated with ImageJ/Fiji (NIH, USA) and the JACoP plugin for colocalization studies. Overlap of NPs with neuronal cell membrane as a function of time was evaluated using Manders M1 and M2 coefficients.

4.4 RETINAL EXPLANTS

Following 30 minutes of dark adaptation, 12-15 months old RCS rats were euthanized by means of high-dose carbon dioxide (CO_2) inhalation. All the procedures were carried out in dim red light since rats are known to lack photoreceptors responding to this wavelength. Both eyeballs were surgically enucleated and quickly placed in oxygenated (95% O_2, 5% CO_2) Ames' Medium solution (Sigma-Aldrich), minimizing the time in which retinal tissue was left deoxygenated. Dissection of the eyeball was performed first on a dry surface and then in liquid. The procedure is performed as follows: (i) a first hole through the eyeball at the level of the *ora serrata* is obtained by means of the tip of a scalpel blade, (ii) dissecting scissors are passed through the hole and used to cut and dissect the cornea from the sclera, choroid and retina, (iii) lens and vitreous body are removed, (iv) residual tissues are cut in half in order to facilitate the following steps and then moved into a separate Ames' solution petri dish in order to continue the dissection under the microscope. In liquid, the two hemiretinas are gently dissected from the sclera by means of dissecting forceps, avoiding pointing or grasping, in order to minimize the stress on the tissue. The choroid was left in place to allow for a subretinal injection of the NPs and to mimic an in vivo configuration. Each hemiretina is divided into smaller pieces prior to the subretinal injection and further settling onto the MEAs. The injection in performed under the stereoscopic microscope with an insulin gauge syringe (approximatively 2 µl injection).

Multielectrode Array Recordings

Recording of extracellular activity from RGCs of RCS rats injected with NPs was carried out on 60-electrodes planar MEA devices. Electrodes of 10 µm in diameter are disposed in a 8 x 8 matrix, with an inter-electrodes distance of 100 µm; one of the electrodes works as an internal reference (iR) (MEA 100/10iR-ITO-gr, Multi-Channel Systems GmbH). The devices were also provided with a 1.5 mL capacity glass ring/culture chamber that allowed to perfuse the experimental sample with oxygenated solution. Pieces of retina to be tested were cut out from the previously isolated hemiretinas in Ames' Medium, with arbitrary dimensions matching as closely as possible the electrodes surface on the MEA (~1 mm^2). Experimental samples were placed onto the MEA with the RGCs layer facing the electrodes surface (face down on the plate). To keep the tissue oxygenated, the MEA chamber was continuously perfused by a peristaltic pump (ISMATEC) with oxygenated (95% O_2 5% CO_2) Ames' Medium.

Electrical activity was recorded using the MEA1060-INV BC by Multichannel Systems (MCS GmbH, Reutlingen, Germany), with a total amplification of 1200 (two stage amplification). MC Rack software (MCS GmbH) was used for the recording, detection and sorting of the data. To distinguish action potentials from background noise (~15 µV,

peak-to-peak), we arbitrarily chose a threshold of detection equal to 4.5 times the SD of the signal (automatically calculated by the acquisition system for each electrode). MCS system was optically coupled with light stimulation by means of the inverted microscope Nikon Eclipse Ti, using a VSD IR filter and a 20x objective which produces an illumination spot on the sample of 0.93 mm^2 .

For the experiments comparing acute and chronic exposure of the NPs, control RCS retinal tissue was employed to perform an injection of P3HT-NPs solution between the choroid and the inner retina under a stereomicroscope to achieve the acute condition, allowing for the sandwich configuration to limit the diffusion of the photoactive compound out of the subretinal space. Light-evoked extracellular activity recordings were obtained with a fiber-coupled Lumencor LED system, composed of 6 independent solid-state light sources which can be individually activated (Spectra X) peaking at 530 nm fed to an inverted Nikon Eclipse Ti microscope, with a power density of 20 mW/mm^2. Light pulses of 200 ms duration were administered at 0.25 Hz, 25 times for each condition. Only retinal explants where P3HT-NPs intrinsic fluorescence was detected concomitantly with the recording were included in the analysis, to ensure a correlation between the injection (either chronic or acute) of the photoactive material and the firing modulation. Data was acquired at 25 kHz and high pass filtered at 200 Hz. Spike detection was performed using MC Rack software (Multi Channel Systems) and the analysis of the firing frequency performed with OriginPro2020 and GraphPad Prism 9.1.2. MC-Rack recordings and Spectra X stimulations were synchronized by the Stimulus Generator STG4008 (MCS GmbH). By means of the MC-Stimulus II software it is possible to drive TTL signals (Transistor-Transistor Logic) that synchronize MEA recordings with an external device, in this case, the Spectra X light source. PSTH were realized for each electrode with a threshold activity of 0.8 Hz basal firing, given a spike detection threshold set at 4 SDs from the noise. Light-evoked firing activity was assessed by selecting those electrodes showing a statistically significant modulation of firing time locked to the light stimulus with respect to the baseline. For the experiments to test the light-dependent activity of dystrophic retinal explants, light stimulation was performed at 530 nm with pulses of 10 or 200 ms at 0.25 Hz and intensities of 10 and 20 mW/mm^2. Total number of electrodes for SiO_2, P3HT:PCBM, and P3HT;PCBM:GO respectively; 10 ms, 10 mW/mm^2, = 608, 558, 886; 10 ms, 20 mW/mm^2, = 569, 530, 776; 200 ms, 10 mW/mm^2, = 606, 547, 818; 200 ms, 20 mW/mm^2, = 608, 558, 886.

4.5 LIGHT-CUED CLASSICAL CONDITIONING

The classical conditioning experiment took place in an environmental chamber that included a grid for administering the shocks (Med Associated Inc.). Test sessions were recorded by a camera installed on the chamber's front door, and behavioral freezing was identified and quantified automatically using the integrated software. The protocol used in this experiment consisted of 3 phases[374].

I. The Conditioning session began with a 2-minute period for habituation, during which the animals freely explored their surrounding environment. Following this, a sequence of seven repetitions of white light flashes (22 lux at frequency of 5 Hz; 2 s on /2 s off repeated for 5 times) served as the conditioning stimulus (CS) with 60 s off between

each CS. During the final 2 s of each light flash, a mild foot shock (0.5 mA) was administered as the unconditioned stimulus (US). Each mouse underwent seven CS-US pairings, separated by intervals of variable duration[374]. To assess the associative learning between the US and CS, we measured the freezing behavior during each US-CS pairing.

II. The Cue test was conducted on the day following the conditioning session, using the same apparatus. To prevent the association of the chamber with the US and to exclusively assess the CS-US association, changes were made to the environment. This included covering the grid floor with a smooth white plastic sheet, replacing the arena with walls featuring black and white stripes, introducing, a new aromatic odor (Vanillin, Sigma-Aldrich) and placing two wired cups within the chamber. After allowing the animals to acclimate to the modified chamber for 5 minutes, the test commenced. First, the animals spent 2 minutes in the dark without any stimulation, and then each animal was exposed to continuous 3-minute CS. To determine whether the rats could perceive the light stimulus, we measured the freezing behavior during the 2 minutes of darkness and the 3 minutes of CS.

III. The Context session was held the day after the Cue test session, within the same chamber used during the conditioning session. During this session, each rat spent 5 minutes in the chamber without any CS or US presentation, and their freezing behavior was assessed and scored.

Before each test session, rats were dark-adapted for 1 hour and all experiments were carried out in the dark. For each test session, the freezing behavior was quantified as a percentage, calculated by dividing the time spent freezing (in seconds) by the total time (in seconds) of the session.

4.6 STATISTICS

Box plots represent the median (centre line), 25^{th}-75^{th} percentiles (box) and limit of three times the interquartile range, the cross indicates the mean of the population. Data are given as mean ± SEM for n = sample size. The statistical analysis used is described in the figure legends. To assess for normal distribution of data, the D'Agostino-Pearson's normality test was used, before subjecting the data to further parametric or non-parametric statistical tests. To compare two normally distributed sample groups, either the Student's *t*-test or the Mann–Whitney's *U*-test was used. To compare more than two normally distributed sample groups: one-way ANOVA followed by Tukey's test was used. The statistical significance is considered at $p<0.05$. The Manders coefficients M1 was defined as the fraction of neuronal cell membrane colocalizing with the NPs and M2 as the fraction of NPs colocalizing with neuronal membrane. Statistical analysis was carried out using OriginPro2020, and GraphPad Prism 6.07 & 9.

5 REFERENCES

(1) Enoch, J.; McDonald, L.; Jones, L.; Jones, P. R.; Crabb, D. P. Evaluating Whether Sight Is the Most Valued Sense. *JAMA Ophthalmol* **2019**, *137* (11), 1317. https://doi.org/10.1001/jamaophthalmol.2019.3537.

(2) Burton, M. J.; Ramke, J.; Marques, A. P.; Bourne, R. R. A.; Congdon, N.; Jones, I.; Ah Tong, B. A. M.; Arunga, S.; Bachani, D.; Bascaran, C.; Bastawrous, A.; Blanchet, K.; Braithwaite, T.; Buchan, J. C.; Cairns, J.; Cama, A.; Chagunda, M.; Chuluunkhuu, C.; Cooper, A.; Crofts-Lawrence, J.; Dean, W. H.; Denniston, A. K.; Ehrlich, J. R.; Emerson, P. M.; Evans, J. R.; Frick, K. D.; Friedman, D. S.; Furtado, J. M.; Gichangi, M. M.; Gichuhi, S.; Gilbert, S. S.; Gurung, R.; Habtamu, E.; Holland, P.; Jonas, J. B.; Keane, P. A.; Keay, L.; Khanna, R. C.; Khaw, P. T.; Kuper, H.; Kyari, F.; Lansingh, V. C.; Mactaggart, I.; Mafwiri, M. M.; Mathenge, W.; McCormick, I.; Morjaria, P.; Mowatt, L.; Muirhead, D.; Murthy, G. V. S.; Mwangi, N.; Patel, D. B.; Peto, T.; Qureshi, B. M.; Salomão, S. R.; Sarah, V.; Shilio, B. R.; Solomon, A. W.; Swenor, B. K.; Taylor, H. R.; Wang, N.; Webson, A.; West, S. K.; Wong, T. Y.; Wormald, R.; Yasmin, S.; Yusufu, M.; Silva, J. C.; Resnikoff, S.; Ravilla, T.; Gilbert, C. E.; Foster, A.; Faal, H. B. The Lancet Global Health Commission on Global Eye Health: Vision beyond 2020. *The Lancet Global Health* **2021**, *9* (4), e489–e551. https://doi.org/10.1016/S2214-109X(20)30488-5.

(3) Court, H.; McLean, G.; Guthrie, B.; Mercer, S. W.; Smith, D. J. Visual Impairment Is Associated with Physical and Mental Comorbidities in Older Adults: A Cross-Sectional Study. *BMC Med* **2014**, *12* (1), 181. https://doi.org/10.1186/s12916-014-0181-7.

(4) *World Health Organization 2019 World Report on Vision Https://Www.Who.Int/Publications/i/Item/9789241516570*.

(5) Bourne, R.; Steinmetz, J. D.; Flaxman, S.; Briant, P. S.; Taylor, H. R.; Resnikoff, S.; Casson, R. J.; Abdoli, A.; Abu-Gharbieh, E.; Afshin, A.; Ahmadieh, H.; Akalu, Y.; Alamneh, A. A.; Alemayehu, W.; Alfaar, A. S.; Alipour, V.; Anbesu, E. W.; Androudi, S.; Arabloo, J.; Arditi, A.; Asaad, M.; Bagli, E.; Baig, A. A.; Bärnighausen, T. W.; Battaglia Parodi, M.; Bhagavathula, A. S.; Bhardwaj, N.; Bhardwaj, P.; Bhattacharyya, K.; Bijani, A.; Bikbov, M.; Bottone, M.; Braithwaite, T.; Bron, A. M.; Butt, Z. A.; Cheng, C.-Y.; Chu, D.-T.; Cicinelli, M. V.; Coelho, J. M.; Dagnew, B.; Dai, X.; Dana, R.; Dandona, L.; Dandona, R.; Del Monte, M. A.; Deva, J. P.; Diaz, D.; Djalalinia, S.; Dreer, L. E.; Ehrlich, J. R.; Ellwein, L. B.; Emamian, M. H.; Fernandes, A. G.; Fischer, F.; Friedman, D. S.; Furtado, J. M.; Gaidhane, A. M.; Gaidhane, S.; Gazzard, G.; Gebremichael, B.; George, R.; Ghashghaee, A.; Golechha, M.; Hamidi, S.; Hammond, B. R.; Hartnett, M. E. R.; Hartono, R. K.; Hay, S. I.; Heidari, G.; Ho, H. C.; Hoang, C. L.; Househ, M.; Ibitoye, S. E.; Ilic, I. M.; Ilic, M. D.; Ingram, A. D.; Irvani, S. S. N.; Jha, R. P.; Kahloun, R.; Kandel, H.; Kasa, A. S.; Kempen, J. H.; Keramati, M.; Khairallah, M.; Khan, E. A.; Khanna, R. C.; Khatib, M. N.; Kim, J. E.; Kim, Y. J.; Kisa, S.; Kisa, A.; Koyanagi, A.; Kurmi, O. P.; Lansingh, V. C.; Leasher, J. L.; Leveziel, N.; Limburg, H.; Majdan, M.; Manafi, N.; Mansouri, K.; McAlinden, C.; Mohammadi, S. F.; Mohammadian-Hafshejani, A.; Mohammadpourhodki, R.; Mokdad, A. H.; Moosavi, D.; Morse, A. R.; Naderi, M.; Naidoo, K. S.; Nangia, V.; Nguyen, C. T.; Nguyen, H. L. T.; Ogundimu, K.; Olagunju, A. T.; Ostroff, S. M.; Panda-Jonas, S.; Pesudovs, K.; Peto, T.; Quazi Syed, Z.; Rahman, M. H. U.; Ramulu, P. Y.; Rawaf, S.; Rawaf, D. L.; Reinig, N.; Robin, A. L.; Rossetti, L.; Safi, S.; Sahebkar, A.; Samy, A. M.; Saxena, D.; Serle, J. B.; Shaikh, M. A.; Shen, T. T.; Shibuya, K.; Shin, J. I.; Silva, J. C.; Silvester, A.; Singh, J. A.; Singhal, D.; Sitorus, R. S.; Skiadaresi, E.; Skirbekk, V.; Soheili, A.; Sousa, R. A. R. C.; Spurlock, E. E.; Stambolian, D.; Taddele, B. W.; Tadesse, E. G.; Tahhan, N.; Tareque, M. I.; Topouzis, F.; Tran, B. X.; Travillian, R. S.; Tsilimbaris, M. K.; Varma, R.; Virgili, G.; Wang, Y. X.; Wang, N.; West, S. K.; Wong, T. Y.; Zaidi, Z.; Zewdie, K. A.; Jonas, J. B.; Vos, T. Trends in Prevalence of

Blindness and Distance and near Vision Impairment over 30 Years: An Analysis for the Global Burden of Disease Study. *The Lancet Global Health* **2021**, *9* (2), e130–e143. https://doi.org/10.1016/S2214-109X(20)30425-3.

(6) *World Health Organization 2021 Vision Impairment and Blindness Int. Https://Www.Who.Int/News-Room/Fact-Sheets/Detail/Blindness-and-Visual-Impairment.*

(7) Marc, R. E.; Jones, B. W.; Watt, C. B.; Strettoi, E. Neural Remodeling in Retinal Degeneration. *Progress in Retinal and Eye Research* **2003**, *22* (5), 607–655. https://doi.org/10.1016/S1350-9462(03)00039-9.

(8) Cuenca, N.; Fernández-Sánchez, L.; Campello, L.; Maneu, V.; De La Villa, P.; Lax, P.; Pinilla, I. Cellular Responses Following Retinal Injuries and Therapeutic Approaches for Neurodegenerative Diseases. *Progress in Retinal and Eye Research* **2014**, *43*, 17–75. https://doi.org/10.1016/j.preteyeres.2014.07.001.

(9) Marc, R. E.; Jones, B. W.; Anderson, J. R.; Kinard, K.; Marshak, D. W.; Wilson, J. H.; Wensel, T.; Lucas, R. J. Neural Reprogramming in Retinal Degeneration. *Invest. Ophthalmol. Vis. Sci.* **2007**, *48* (7), 3364. https://doi.org/10.1167/iovs.07-0032.

(10) Stasheff, S. F.; Shankar, M.; Andrews, M. P. Developmental Time Course Distinguishes Changes in Spontaneous and Light-Evoked Retinal Ganglion Cell Activity in *Rd1* and *Rd10* Mice. *Journal of Neurophysiology* **2011**, *105* (6), 3002–3009. https://doi.org/10.1152/jn.00704.2010.

(11) Santos, A. Preservation of the Inner Retina in Retinitis Pigmentosa: A Morphometric Analysis. *Arch Ophthalmol* **1997**, *115* (4), 511. https://doi.org/10.1001/archopht.1997.01100150513011.

(12) Stone, J. L. Morphometric Analysis of Macular Photoreceptors and Ganglion Cells in Retinas With Retinitis Pigmentosa. *Arch Ophthalmol* **1992**, *110* (11), 1634. https://doi.org/10.1001/archopht.1992.01080230134038.

(13) Sekirnjak, C.; Jepson, L. H.; Hottowy, P.; Sher, A.; Dabrowski, W.; Litke, A. M.; Chichilnisky, E. J. Changes in Physiological Properties of Rat Ganglion Cells during Retinal Degeneration. *Journal of Neurophysiology* **2011**, *105* (5), 2560–2571. https://doi.org/10.1152/jn.01061.2010.

(14) Stasheff, S. F. Emergence of Sustained Spontaneous Hyperactivity and Temporary Preservation of OFF Responses in Ganglion Cells of the Retinal Degeneration (*Rd1*) Mouse. *Journal of Neurophysiology* **2008**, *99* (3), 1408–1421. https://doi.org/10.1152/jn.00144.2007.

(15) Telias, M.; Denlinger, B.; Helft, Z.; Thornton, C.; Beckwith-Cohen, B.; Kramer, R. H. Retinoic Acid Induces Hyperactivity, and Blocking Its Receptor Unmasks Light Responses and Augments Vision in Retinal Degeneration. *Neuron* **2019**, *102* (3), 574-586.e5. https://doi.org/10.1016/j.neuron.2019.02.015.

(16) Tochitsky, I.; Helft, Z.; Meseguer, V.; Fletcher, R. B.; Vessey, K. A.; Telias, M.; Denlinger, B.; Malis, J.; Fletcher, E. L.; Kramer, R. H. How Azobenzene Photoswitches Restore Visual Responses to the Blind Retina. *Neuron* **2016**, *92* (1), 100–113. https://doi.org/10.1016/j.neuron.2016.08.038.

(17) Kramer, R. H. Suppressing Retinal Remodeling to Mitigate Vision Loss in Photoreceptor Degenerative Disorders. *Annu. Rev. Vis. Sci.* **2023**, *9* (1), 131–153. https://doi.org/10.1146/annurev-vision-112122-020957.

(18) Hartong, D. T.; Berson, E. L.; Dryja, T. P. Retinitis Pigmentosa. *The Lancet* **2006**, *368* (9549), 1795–1809. https://doi.org/10.1016/S0140-6736(06)69740-7.

(19) Fahim, A. Retinitis Pigmentosa: Recent Advances and Future Directions in Diagnosis and Management. *Current Opinion in Pediatrics* **2018**, *30* (6), 725–733. https://doi.org/10.1097/MOP.0000000000000690.

(20) Ripps, H. Cell Death in Retinitis Pigmentosa: Gap Junctions and the 'Bystander' Effect. *Experimental Eye Research* **2002**, *74* (3), 327–336. https://doi.org/10.1006/exer.2002.1155.

(21) Roque, R. S.; Imperial, C. J.; Caldwell, R. B. Microglial Cells Invade the Outer Retina as Photoreceptors Degenerate in Royal College of Surgeons Rats. *Investigative ophthalmology & visual science* **1996**, *37* (1), 196–203.

(22) Peng, B.; Xiao, J.; Wang, K.; So, K.-F.; Tipoe, G. L.; Lin, B. Suppression of Microglial Activation Is Neuroprotective in a Mouse Model of Human Retinitis Pigmentosa. *Journal of Neuroscience* **2014**, *34* (24), 8139–8150. https://doi.org/10.1523/JNEUROSCI.5200-13.2014.

(23) Léveillard, T.; Mohand-Saïd, S.; Lorentz, O.; Hicks, D.; Fintz, A.-C.; Clérin, E.; Simonutti, M.; Forster, V.; Cavusoglu, N.; Chalmel, F.; Dollé, P.; Poch, O.; Lambrou, G.; Sahel, J.-A. Identification and Characterization of Rod-Derived Cone Viability Factor. *Nat Genet* **2004**, *36* (7), 755–759. https://doi.org/10.1038/ng1386.

(24) Campochiaro, P. A.; Mir, T. A. The Mechanism of Cone Cell Death in Retinitis Pigmentosa. *Progress in Retinal and Eye Research* **2018**, *62*, 24–37. https://doi.org/10.1016/j.preteyeres.2017.08.004.

(25) Menghini, M.; Cehajic-Kapetanovic, J.; MacLaren, R. E. Monitoring Progression of Retinitis Pigmentosa: Current Recommendations and Recent Advances. *Expert Opinion on Orphan Drugs* **2020**, *8* (2–3), 67–78. https://doi.org/10.1080/21678707.2020.1735352.

(26) Dias, M. F.; Joo, K.; Kemp, J. A.; Fialho, S. L.; Da Silva Cunha, A.; Woo, S. J.; Kwon, Y. J. Molecular Genetics and Emerging Therapies for Retinitis Pigmentosa: Basic Research and Clinical Perspectives. *Progress in Retinal and Eye Research* **2018**, *63*, 107–131. https://doi.org/10.1016/j.preteyeres.2017.10.004.

(27) Daiger, S. P.; Sullivan, L. S.; Bowne, S. J. Genes and Mutations Causing Retinitis Pigmentosa: Genes and Mutations Causing Retinitis Pigmentosa. *Clin Genet* **2013**, *84* (2), 132–141. https://doi.org/10.1111/cge.12203.

(28) Hamel, C. Retinitis Pigmentosa. *Orphanet J Rare Dis* **2006**, *1* (1), 40. https://doi.org/10.1186/1750-1172-1-40.

(29) Bittner, A. K.; Diener-West, M.; Dagnelie, G. A SURVEY OF PHOTOPSIAS IN SELF-REPORTED RETINITIS PIGMENTOSA: Location of Photopsias Is Related to Disease Severity. *Retina* **2009**, *29* (10), 1513–1521. https://doi.org/10.1097/IAE.0b013e3181af0d57.

(30) Bittner, A. K.; Diener-West, M.; Dagnelie, G. Characteristics and Possible Visual Consequences of Photopsias as Vision Measures Are Reduced in Retinitis Pigmentosa. *Invest. Ophthalmol. Vis. Sci.* **2011**, *52* (9), 6370. https://doi.org/10.1167/iovs.11-7195.

(31) Pinckers, A.; Van Aarem, A.; Keunen, J. E. E. Colour Vision in Retinitis Pigmentosa: Influence of Cystoid Macular Edema. *Int Ophthalmol* **1993**, *17* (3), 143–146. https://doi.org/10.1007/BF00942928.

(32) Bensinger, E.; Rinella, N.; Saud, A.; Loumou, P.; Ratnam, K.; Griffin, S.; Qin, J.; Porco, T. C.; Roorda, A.; Duncan, J. L. Loss of Foveal Cone Structure Precedes Loss of Visual Acuity in Patients With Rod-Cone Degeneration. *Invest. Ophthalmol. Vis. Sci.* **2019**, *60* (8), 3187. https://doi.org/10.1167/iovs.18-26245.

(33) Delori, F. C.; Dorey, C. K.; Staurenghi, G.; Arend, O.; Goger, D. G.; Weiter, J. J. In Vivo Fluorescence of the Ocular Fundus Exhibits Retinal Pigment Epithelium Lipofuscin Characteristics. *Invest Ophthalmol Vis Sci* **1995**, *36* (3), 718–729.

(34) Forrester, J. V.; Lois., N. *Fundus Autofluorescence*; 2015.

(35) Greenstein, V. C.; Duncker, T.; Holopigian, K.; Carr, R. E.; Greenberg, J. P.; Tsang, S. H.; Hood, D. C. STRUCTURAL AND FUNCTIONAL CHANGES ASSOCIATED WITH NORMAL

AND ABNORMAL FUNDUS AUTOFLUORESCENCE IN PATIENTS WITH RETINITIS PIGMENTOSA. *Retina* **2012**, *32* (2), 349–357. https://doi.org/10.1097/IAE.0b013e31821dfc17.

(36) Liu, G.; Liu, X.; Li, H.; Du, Q.; Wang, F. Optical Coherence Tomographic Analysis of Retina in Retinitis Pigmentosa Patients. *Ophthalmic Res* **2016**, *56* (3), 111–122. https://doi.org/10.1159/000445063.

(37) Hood, D. C.; Lazow, M. A.; Locke, K. G.; Greenstein, V. C.; Birch, D. G. The Transition Zone between Healthy and Diseased Retina in Patients with Retinitis Pigmentosa. *Invest. Ophthalmol. Vis. Sci.* **2011**, *52* (1), 101. https://doi.org/10.1167/iovs.10-5799.

(38) Tee, J. J. L.; Carroll, J.; Webster, A. R.; Michaelides, M. Quantitative Analysis of Retinal Structure Using Spectral-Domain Optical Coherence Tomography in RPGR - Associated Retinopathy. *American Journal of Ophthalmology* **2017**, *178*, 18–26. https://doi.org/10.1016/j.ajo.2017.03.012.

(39) Sun, L. W.; Johnson, R. D.; Langlo, C. S.; Cooper, R. F.; Razeen, M. M.; Russillo, M. C.; Dubra, A.; Connor, T. B.; Han, D. P.; Pennesi, M. E.; Kay, C. N.; Weinberg, D. V.; Stepien, K. E.; Carroll, J. Assessing Photoreceptor Structure in Retinitis Pigmentosa and Usher Syndrome. *Invest. Ophthalmol. Vis. Sci.* **2016**, *57* (6), 2428. https://doi.org/10.1167/iovs.15-18246.

(40) Sajovic, J.; Meglič, A.; Glavač, D.; Markelj, Š.; Hawlina, M.; Fakin, A. The Role of Vitamin A in Retinal Diseases. *IJMS* **2022**, *23* (3), 1014. https://doi.org/10.3390/ijms23031014.

(41) Berson, E. L. A Randomized Trial of Vitamin A and Vitamin E Supplementation for Retinitis Pigmentosa. *Arch Ophthalmol* **1993**, *111* (6), 761. https://doi.org/10.1001/archopht.1993.01090060049022.

(42) Berson, E. L. Further Evaluation of Docosahexaenoic Acid in Patients With RetinitisPigmentosa Receiving Vitamin A Treatment: Subgroup Analyses. *Arch Ophthalmol* **2004**, *122* (9), 1306. https://doi.org/10.1001/archopht.122.9.1306.

(43) Berson, E. L.; Rosner, B.; Sandberg, M. A.; Weigel-DiFranco, C.; Brockhurst, R. J.; Hayes, K. C.; Johnson, E. J.; Anderson, E. J.; Johnson, C. A.; Gaudio, A. R.; Willett, W. C.; Schaefer, E. J. Clinical Trial of Lutein in Patients with Retinitis Pigmentosa Receiving Vitamin A. *Arch Ophthalmol* **2010**, *128* (4), 403–411. https://doi.org/10.1001/archophthalmol.2010.32.

(44) Solinís, M. Á.; Del Pozo-Rodríguez, A.; Apaolaza, P. S.; Rodríguez-Gascón, A. Treatment of Ocular Disorders by Gene Therapy. *European Journal of Pharmaceutics and Biopharmaceutics* **2015**, *95*, 331–342. https://doi.org/10.1016/j.ejpb.2014.12.022.

(45) Rodrigues, G. A.; Shalaev, E.; Karami, T. K.; Cunningham, J.; Slater, N. K. H.; Rivers, H. M. Pharmaceutical Development of AAV-Based Gene Therapy Products for the Eye. *Pharm Res* **2019**, *36* (2), 29. https://doi.org/10.1007/s11095-018-2554-7.

(46) Russell, S.; Bennett, J.; Wellman, J. A.; Chung, D. C.; Yu, Z.-F.; Tillman, A.; Wittes, J.; Pappas, J.; Elci, O.; McCague, S.; Cross, D.; Marshall, K. A.; Walshire, J.; Kehoe, T. L.; Reichert, H.; Davis, M.; Raffini, L.; George, L. A.; Hudson, F. P.; Dingfield, L.; Zhu, X.; Haller, J. A.; Sohn, E. H.; Mahajan, V. B.; Pfeifer, W.; Weckmann, M.; Johnson, C.; Gewaily, D.; Drack, A.; Stone, E.; Wachtel, K.; Simonelli, F.; Leroy, B. P.; Wright, J. F.; High, K. A.; Maguire, A. M. Efficacy and Safety of Voretigene Neparvovec (AAV2-hRPE65v2) in Patients with RPE65 -Mediated Inherited Retinal Dystrophy: A Randomised, Controlled, Open-Label, Phase 3 Trial. *The Lancet* **2017**, *390* (10097), 849–860. https://doi.org/10.1016/S0140-6736(17)31868-8.

(47) Sahel, J.-A.; Boulanger-Scemama, E.; Pagot, C.; Arleo, A.; Galluppi, F.; Martel, J. N.; Esposti, S. D.; Delaux, A.; De Saint Aubert, J.-B.; De Montleau, C.; Gutman, E.; Audo, I.; Duebel, J.; Picaud, S.; Dalkara, D.; Blouin, L.; Taiel, M.; Roska, B. Partial Recovery of

Visual Function in a Blind Patient after Optogenetic Therapy. *Nat Med* **2021**, *27* (7), 1223–1229. https://doi.org/10.1038/s41591-021-01351-4.

(48) Jones, M. K.; Lu, B.; Girman, S.; Wang, S. Cell-Based Therapeutic Strategies for Replacement and Preservation in Retinal Degenerative Diseases. *Progress in Retinal and Eye Research* **2017**, *58*, 1–27. https://doi.org/10.1016/j.preteyeres.2017.01.004.

(49) Shen, Y. Stem Cell Therapies for Retinal Diseases: From Bench to Bedside. *J Mol Med* **2020**, *98* (10), 1347–1368. https://doi.org/10.1007/s00109-020-01960-5.

(50) Sharma, A.; Jaganathan, B. G. Stem Cell Therapy for Retinal Degeneration: The Evidence to Date. *BTT* **2021**, *Volume 15*, 299–306. https://doi.org/10.2147/BTT.S290331.

(51) Wang, Z.; Gao, F.; Zhang, M.; Zheng, Y.; Zhang, F.; Xu, L.; Cao, L.; He, W. Intravitreal Injection of Human Retinal Progenitor Cells for Treatment of Retinal Degeneration. *Med Sci Monit* **2020**, *26*. https://doi.org/10.12659/MSM.921184.

(52) Tu, H.-Y.; Watanabe, T.; Shirai, H.; Yamasaki, S.; Kinoshita, M.; Matsushita, K.; Hashiguchi, T.; Onoe, H.; Matsuyama, T.; Kuwahara, A.; Kishino, A.; Kimura, T.; Eiraku, M.; Suzuma, K.; Kitaoka, T.; Takahashi, M.; Mandai, M. Medium- to Long-Term Survival and Functional Examination of Human iPSC-Derived Retinas in Rat and Primate Models of Retinal Degeneration. *EBioMedicine* **2019**, *39*, 562–574. https://doi.org/10.1016/j.ebiom.2018.11.028.

(53) Zhu, D.; Xie, M.; Gademann, F.; Cao, J.; Wang, P.; Guo, Y.; Zhang, L.; Su, T.; Zhang, J.; Chen, J. Protective Effects of Human iPS-Derived Retinal Pigmented Epithelial Cells on Retinal Degenerative Disease. *Stem Cell Res Ther* **2020**, *11* (1), 98. https://doi.org/10.1186/s13287-020-01608-8.

(54) Surendran, H.; Nandakumar, S.; Reddy K, V. B.; Stoddard, J.; Mohan K, V.; Upadhyay, P. K.; McGill, T. J.; Pal, R. Transplantation of Retinal Pigment Epithelium and Photoreceptors Generated Concomitantly via Small Molecule-Mediated Differentiation Rescues Visual Function in Rodent Models of Retinal Degeneration. *Stem Cell Res Ther* **2021**, *12* (1), 70. https://doi.org/10.1186/s13287-021-02134-x.

(55) Salas, A.; Duarri, A.; Fontrodona, L.; Ramírez, D. M.; Badia, A.; Isla-Magrané, H.; Ferreira-de-Souza, B.; Zapata, M. Á.; Raya, Á.; Veiga, A.; García-Arumí, J. Cell Therapy with hiPSC-Derived RPE Cells and RPCs Prevents Visual Function Loss in a Rat Model of Retinal Degeneration. *Molecular Therapy - Methods & Clinical Development* **2021**, *20*, 688–702. https://doi.org/10.1016/j.omtm.2021.02.006.

(56) Tuekprakhon, A.; Sangkitporn, S.; Trinavarat, A.; Pawestri, A. R.; Vamvanij, V.; Ruangchainikom, M.; Luksanapruksa, P.; Pongpaksupasin, P.; Khorchai, A.; Dambua, A.; Boonchu, P.; Yodtup, C.; Uiprasertkul, M.; Sangkitporn, S.; Atchaneeyasakul, L. Intravitreal Autologous Mesenchymal Stem Cell Transplantation: A Non-Randomized Phase I Clinical Trial in Patients with Retinitis Pigmentosa. *Stem Cell Res Ther* **2021**, *12* (1), 52. https://doi.org/10.1186/s13287-020-02122-7.

(57) Zarbin, M. Cell-Based Therapy for Retinal Disease: The New Frontier. In *Retinal Degeneration*; Weber, B. H. F., Langmann, T., Eds.; Methods in Molecular Biology; Springer New York: New York, NY, 2019; Vol. 1834, pp 367–381. https://doi.org/10.1007/978-1-4939-8669-9_23.

(58) Siqueira, R. C.; Messias, A.; Messias, K.; Arcieri, R. S.; Ruiz, M. A.; Souza, N. F.; Martins, L. C.; Jorge, R. Quality of Life in Patients with Retinitis Pigmentosa Submitted to Intravitreal Use of Bone Marrow-Derived Stem Cells (Reticell -Clinical Trial). *Stem Cell Res Ther* **2015**, *6* (1), 29. https://doi.org/10.1186/s13287-015-0020-6.

(59) Sugita, S.; Mandai, M.; Kamao, H.; Takahashi, M. Immunological Aspects of RPE Cell Transplantation. *Progress in Retinal and Eye Research* **2021**, *84*, 100950. https://doi.org/10.1016/j.preteyeres.2021.100950.

(60) Singh, M. S.; Park, S. S.; Albini, T. A.; Canto-Soler, M. V.; Klassen, H.; MacLaren, R. E.; Takahashi, M.; Nagiel, A.; Schwartz, S. D.; Bharti, K. Retinal Stem Cell Transplantation: Balancing Safety and Potential. *Progress in Retinal and Eye Research* **2020**, *75*, 100779. https://doi.org/10.1016/j.preteyeres.2019.100779.

(61) Apte, R. S. Age-Related Macular Degeneration. *N Engl J Med* **2021**, *385* (6), 539–547. https://doi.org/10.1056/NEJMcp2102061.

(62) Wong, W. L.; Su, X.; Li, X.; Cheung, C. M. G.; Klein, R.; Cheng, C.-Y.; Wong, T. Y. Global Prevalence of Age-Related Macular Degeneration and Disease Burden Projection for 2020 and 2040: A Systematic Review and Meta-Analysis. *The Lancet Global Health* **2014**, *2* (2), e106–e116. https://doi.org/10.1016/S2214-109X(13)70145-1.

(63) Deng, Y.; Qiao, L.; Du, M.; Qu, C.; Wan, L.; Li, J.; Huang, L. Age-Related Macular Degeneration: Epidemiology, Genetics, Pathophysiology, Diagnosis, and Targeted Therapy. *Genes & Diseases* **2022**, *9* (1), 62–79. https://doi.org/10.1016/j.gendis.2021.02.009.

(64) Brody, B. L.; Gamst, A. C.; Williams, R. A.; Smith, A. R.; Lau, P. W.; Dolnak, D.; Rapaport, M. H.; Kaplan, R. M.; Brown, S. I. Depression, Visual Acuity, Comorbidity, and Disability Associated with Age-Related Macular Degeneration. *Ophthalmology* **2001**, *108* (10), 1893–1900. https://doi.org/10.1016/S0161-6420(01)00754-0.

(65) Mitchell, J.; Bradley, C. Quality of Life in Age-Related Macular Degeneration: A Review of the Literature. *Health Qual Life Outcomes* **2006**, *4* (1), 97. https://doi.org/10.1186/1477-7525-4-97.

(66) Gopinath, B.; Liew, G.; Burlutsky, G.; Mitchell, P. Age-Related Macular Degeneration and 5-Year Incidence of Impaired Activities of Daily Living. *Maturitas* **2014**, *77* (3), 263–266. https://doi.org/10.1016/j.maturitas.2013.12.001.

(67) Wood, J. M.; Lacherez, P.; Black, A. A.; Cole, M. H.; Boon, M. Y.; Kerr, G. K. Risk of Falls, Injurious Falls, and Other Injuries Resulting from Visual Impairment among Older Adults with Age-Related Macular Degeneration. *Invest. Ophthalmol. Vis. Sci.* **2011**, *52* (8), 5088. https://doi.org/10.1167/iovs.10-6644.

(68) Klein, R.; Meuer, S. M.; Myers, C. E.; Buitendijk, G. H. S.; Rochtchina, E.; Choudhury, F.; De Jong, P. T. V. M.; McKean-Cowdin, R.; Iyengar, S. K.; Gao, X.; Lee, K. E.; Vingerling, J. R.; Mitchell, P.; Klaver, C. C. W.; Wang, J. J.; Klein, B. E. K. Harmonizing the Classification of Age-Related Macular Degeneration in the Three-Continent AMD Consortium. *Ophthalmic Epidemiology* **2014**, *21* (1), 14–23. https://doi.org/10.3109/09286586.2013.867512.

(69) Klein, R.; Knudtson, M. D.; Lee, K. E.; Gangnon, R. E.; Klein, B. E. K. Age–Period–Cohort Effect on the Incidence of Age-Related Macular Degeneration. *Ophthalmology* **2008**, *115* (9), 1460–1467. https://doi.org/10.1016/j.ophtha.2008.01.026.

(70) Hallak, J. A.; De Sisternes, L.; Osborne, A.; Yaspan, B.; Rubin, D. L.; Leng, T. Imaging, Genetic, and Demographic Factors Associated With Conversion to Neovascular Age-Related Macular Degeneration: Secondary Analysis of a Randomized Clinical Trial. *JAMA Ophthalmol* **2019**, *137* (7), 738. https://doi.org/10.1001/jamaophthalmol.2019.0868.

(71) Smith, W.; Assink, J.; Klein, R.; Mitchell, P.; Klaver, C. C. W.; Klein, B. E. K.; Hofman, A.; Jensen, S.; Wang, J. J.; De Jong, P. T. V. M. Risk Factors for Age-Related Macular Degeneration. *Ophthalmology* **2001**, *108* (4), 697–704. https://doi.org/10.1016/S0161-6420(00)00580-7.

(72) Harris, A.; Wirostko. Age-Related Macular Degeneration and the Aging Eye. *CIA* **2008**, *Volume 3*, 473–482. https://doi.org/10.2147/CIA.S2777.

(73) Jonasson, F.; Fisher, D. E.; Eiriksdottir, G.; Sigurdsson, S.; Klein, R.; Launer, L. J.; Harris, T.; Gudnason, V.; Cotch, M. F. Five-Year Incidence, Progression, and Risk Factors for

Age-Related Macular Degeneration. *Ophthalmology* **2014**, *121* (9), 1766–1772. https://doi.org/10.1016/j.ophtha.2014.03.013.

(74) Mitchell, P. Smoking and the 5-Year Incidence of Age-Related Maculopathy: The Blue Mountains Eye Study. *Arch Ophthalmol* **2002**, *120* (10), 1357. https://doi.org/10.1001/archopht.120.10.1357.

(75) Merle, B. M. J.; Colijn, J. M.; Cougnard-Grégoire, A.; De Koning-Backus, A. P. M.; Delyfer, M.-N.; Kiefte-de Jong, J. C.; Meester-Smoor, M.; Féart, C.; Verzijden, T.; Samieri, C.; Franco, O. H.; Korobelnik, J.-F.; Klaver, C. C. W.; Delcourt, C.; Ajana, S.; Arango-Gonzalez, B.; Armento, A.; Arndt, V.; Bhatia, V.; Bhattacharya, S. S.; Biarnés, M.; Borrell, A.; Bühren, S.; Calado, S. M.; Colijn, J. M.; Cougnard-Grégoire, A.; Dammeier, S.; De Jong, E. K.; De La Cerda, B.; Delcourt, C.; Den Hollander, A. I.; Diaz-Corrales, F. J.; Diether, S.; Emri, E.; Endermann, T.; Ferraro, L. L.; Garcia, M.; Heesterbeek, T. J.; Honisch, S.; Hoyng, C. B.; Kersten, E.; Kilger, E.; Klaver, C. C. W.; Langen, H.; Lengyel, I.; Luthert, P.; Maugeais, C.; Meester-Smoor, M.; Merle, B. M. J.; Monés, J.; Nogoceke, E.; Peto, T.; Pool, F. M.; Rodríguez, E.; Ueffing, M.; Ulrich Bartz-Schmidt, K. U.; Van Leeuwen, E. M.; Verzijden, T.; Zumbansen, M.; Vasiliev, V. Mediterranean Diet and Incidence of Advanced Age-Related Macular Degeneration. *Ophthalmology* **2019**, *126* (3), 381–390. https://doi.org/10.1016/j.ophtha.2018.08.006.

(76) Tan, J. S. L. Dietary Fatty Acids and the 10-Year Incidence of Age-Related Macular Degeneration: The Blue Mountains Eye Study. *Arch Ophthalmol* **2009**, *127* (5), 656. https://doi.org/10.1001/archophthalmol.2009.76.

(77) Parekh, N. Association Between Dietary Fat Intake and Age-Related Macular Degeneration in the Carotenoids in Age-Related Eye Disease Study (CAREDS): An Ancillary Study of the Women's Health Initiative. *Arch Ophthalmol* **2009**, *127* (11), 1483. https://doi.org/10.1001/archophthalmol.2009.130.

(78) Adams, M. K. M.; Chong, E. W.; Williamson, E.; Aung, K. Z.; Makeyeva, G. A.; Giles, G. G.; English, D. R.; Hopper, J.; Guymer, R. H.; Baird, P. N.; Robman, L. D.; Simpson, J. A. 20/20--Alcohol and Age-Related Macular Degeneration: The Melbourne Collaborative Cohort Study. *American Journal of Epidemiology* **2012**, *176* (4), 289–298. https://doi.org/10.1093/aje/kws004.

(79) Cougnard-Grégoire, A.; Delyfer, M.-N.; Korobelnik, J.-F.; Rougier, M.-B.; Malet, F.; Le Goff, M.; Dartigues, J.-F.; Colin, J.; Barberger-Gateau, P.; Delcourt, C. Long-Term Blood Pressure and Age-Related Macular Degeneration: The ALIENOR Study. *Invest. Ophthalmol. Vis. Sci.* **2013**, *54* (3), 1905. https://doi.org/10.1167/iovs.12-10192.

(80) Rudolf, M.; Clark, M. E.; Chimento, M. F.; Li, C.-M.; Medeiros, N. E.; Curcio, C. A. Prevalence and Morphology of Druse Types in the Macula and Periphery of Eyes with Age-Related Maculopathy. *Invest. Ophthalmol. Vis. Sci.* **2008**, *49* (3), 1200. https://doi.org/10.1167/iovs.07-1466.

(81) Li, C.-M.; Clark, M. E.; Rudolf, M.; Curcio, C. A. Distribution and Composition of Esterified and Unesterified Cholesterol in Extra-Macular Drusen. *Experimental Eye Research* **2007**, *85* (2), 192–201. https://doi.org/10.1016/j.exer.2007.04.002.

(82) Curcio, C. A.; Johnson, M.; Huang, J.-D.; Rudolf, M. Aging, Age-Related Macular Degeneration, and the Response-to-Retention of Apolipoprotein B-Containing Lipoproteins. *Progress in Retinal and Eye Research* **2009**, *28* (6), 393–422. https://doi.org/10.1016/j.preteyeres.2009.08.001.

(83) Green, R. W. Histopathology of Age-Related Macular Degeneration. *Molecular Vision* **1999**, *5*, 27.

(84) Sarks, S.; Cherepanoff, S.; Killingsworth, M.; Sarks, J. Relationship of Basal Laminar Deposit and Membranous Debris to the Clinical Presentation of Early Age-Related

Macular Degeneration. *Invest. Ophthalmol. Vis. Sci.* **2007**, *48* (3), 968. https://doi.org/10.1167/iovs.06-0443.

(85) Khan, K. N.; Mahroo, O. A.; Khan, R. S.; Mohamed, M. D.; McKibbin, M.; Bird, A.; Michaelides, M.; Tufail, A.; Moore, A. T. Differentiating Drusen: Drusen and Drusen-like Appearances Associated with Ageing, Age-Related Macular Degeneration, Inherited Eye Disease and Other Pathological Processes. *Progress in Retinal and Eye Research* **2016**, *53*, 70–106. https://doi.org/10.1016/j.preteyeres.2016.04.008.

(86) Abdelfattah, N. S.; Zhang, H.; Boyer, D. S.; Rosenfeld, P. J.; Feuer, W. J.; Gregori, G.; Sadda, S. R. Drusen Volume as a Predictor of Disease Progression in Patients With Late Age-Related Macular Degeneration in the Fellow Eye. *Invest. Ophthalmol. Vis. Sci.* **2016**, *57* (4), 1839. https://doi.org/10.1167/iovs.15-18572.

(87) Fleckenstein, M.; Mitchell, P.; Freund, K. B.; Sadda, S.; Holz, F. G.; Brittain, C.; Henry, E. C.; Ferrara, D. The Progression of Geographic Atrophy Secondary to Age-Related Macular Degeneration. *Ophthalmology* **2018**, *125* (3), 369–390. https://doi.org/10.1016/j.ophtha.2017.08.038.

(88) Spaide, R. F.; Jaffe, G. J.; Sarraf, D.; Freund, K. B.; Sadda, S. R.; Staurenghi, G.; Waheed, N. K.; Chakravarthy, U.; Rosenfeld, P. J.; Holz, F. G.; Souied, E. H.; Cohen, S. Y.; Querques, G.; Ohno-Matsui, K.; Boyer, D.; Gaudric, A.; Blodi, B.; Baumal, C. R.; Li, X.; Coscas, G. J.; Brucker, A.; Singerman, L.; Luthert, P.; Schmitz-Valckenberg, S.; Schmidt-Erfurth, U.; Grossniklaus, H. E.; Wilson, D. J.; Guymer, R.; Yannuzzi, L. A.; Chew, E. Y.; Csaky, K.; Monés, J. M.; Pauleikhoff, D.; Tadayoni, R.; Fujimoto, J. Consensus Nomenclature for Reporting Neovascular Age-Related Macular Degeneration Data. *Ophthalmology* **2020**, *127* (5), 616–636. https://doi.org/10.1016/j.ophtha.2019.11.004.

(89) Manjunath, V.; Goren, J.; Fujimoto, J. G.; Duker, J. S. Analysis of Choroidal Thickness in Age-Related Macular Degeneration Using Spectral-Domain Optical Coherence Tomography. *American Journal of Ophthalmology* **2011**, *152* (4), 663–668. https://doi.org/10.1016/j.ajo.2011.03.008.

(90) Cicinelli, M. V.; Rabiolo, A.; Sacconi, R.; Carnevali, A.; Querques, L.; Bandello, F.; Querques, G. Optical Coherence Tomography Angiography in Dry Age-Related Macular Degeneration. *Survey of Ophthalmology* **2018**, *63* (2), 236–244. https://doi.org/10.1016/j.survophthal.2017.06.005.

(91) Cicinelli, M. V.; Cavalleri, M.; Consorte, A. C.; Rabiolo, A.; Sacconi, R.; Bandello, F.; Querques, G. SWEPT-SOURCE AND SPECTRAL DOMAIN OPTICAL COHERENCE TOMOGRAPHY ANGIOGRAPHY VERSUS DYE ANGIOGRAPHY IN THE MEASUREMENT OF TYPE 1 NEOVASCULARIZATION. *Retina* **2020**, *40* (3), 499–506. https://doi.org/10.1097/IAE.0000000000002452.

(92) Kermany, D. S.; Goldbaum, M.; Cai, W.; Valentim, C. C. S.; Liang, H.; Baxter, S. L.; McKeown, A.; Yang, G.; Wu, X.; Yan, F.; Dong, J.; Prasadha, M. K.; Pei, J.; Ting, M. Y. L.; Zhu, J.; Li, C.; Hewett, S.; Dong, J.; Ziyar, I.; Shi, A.; Zhang, R.; Zheng, L.; Hou, R.; Shi, W.; Fu, X.; Duan, Y.; Huu, V. A. N.; Wen, C.; Zhang, E. D.; Zhang, C. L.; Li, O.; Wang, X.; Singer, M. A.; Sun, X.; Xu, J.; Tafreshi, A.; Lewis, M. A.; Xia, H.; Zhang, K. Identifying Medical Diagnoses and Treatable Diseases by Image-Based Deep Learning. *Cell* **2018**, *172* (5), 1122-1131.e9. https://doi.org/10.1016/j.cell.2018.02.010.

(93) Treder, M.; Lauermann, J. L.; Eter, N. Automated Detection of Exudative Age-Related Macular Degeneration in Spectral Domain Optical Coherence Tomography Using Deep Learning. *Graefes Arch Clin Exp Ophthalmol* **2018**, *256* (2), 259–265. https://doi.org/10.1007/s00417-017-3850-3.

(94) Age-Related Eye Disease Study Research Group. A Randomized, Placebo-Controlled, Clinical Trial of High-Dose Supplementation with Vitamins C and E, Beta Carotene, and Zinc for Age-Related Macular Degeneration and Vision Loss: AREDS Report No.

8. *Arch Ophthalmol* **2001**, *119* (10), 1417–1436. https://doi.org/10.1001/archopht.119.10.1417.

(95) Chew, E. Y.; Clemons, T. E.; SanGiovanni, J. P.; Danis, R. P.; Ferris, F. L.; Elman, M. J.; Antoszyk, A. N.; Ruby, A. J.; Orth, D.; Bressler, S. B.; Fish, G. E.; Hubbard, G. B.; Klein, M. L.; Chandra, S. R.; Blodi, B. A.; Domalpally, A.; Friberg, T.; Wong, W. T.; Rosenfeld, P. J.; Agrón, E.; Toth, C. A.; Bernstein, P. S.; Sperduto, R. D. Secondary Analyses of the Effects of Lutein/Zeaxanthin on Age-Related Macular Degeneration Progression: AREDS2 Report No. 3. *JAMA Ophthalmol* **2014**, *132* (2), 142. https://doi.org/10.1001/jamaophthalmol.2013.7376.

(96) Evans, J. Antioxidant Vitamin and Mineral Supplements for Age-Related Macular Degeneration. In *The Cochrane Database of Systematic Reviews (Complete Reviews)*; The Cochrane Collaboration, Ed.; John Wiley & Sons, Ltd: Chichester, UK, 2002; p CD000254. https://doi.org/10.1002/14651858.CD000254.

(97) Yehoshua, Z.; Alexandre De Amorim Garcia Filho, C.; Nunes, R. P.; Gregori, G.; Penha, F. M.; Moshfeghi, A. A.; Zhang, K.; Sadda, S.; Feuer, W.; Rosenfeld, P. J. Systemic Complement Inhibition with Eculizumab for Geographic Atrophy in Age-Related Macular Degeneration. *Ophthalmology* **2014**, *121* (3), 693–701. https://doi.org/10.1016/j.ophtha.2013.09.044.

(98) Holz, F. G.; Sadda, S. R.; Busbee, B.; Chew, E. Y.; Mitchell, P.; Tufail, A.; Brittain, C.; Ferrara, D.; Gray, S.; Honigberg, L.; Martin, J.; Tong, B.; Ehrlich, J. S.; Bressler, N. M.; Chroma and Spectri Study Investigators. Efficacy and Safety of Lampalizumab for Geographic Atrophy Due to Age-Related Macular Degeneration: Chroma and Spectri Phase 3 Randomized Clinical Trials. *JAMA Ophthalmol* **2018**, *136* (6), 666–677. https://doi.org/10.1001/jamaophthalmol.2018.1544.

(99) Wong, W. T.; Dresner, S.; Forooghian, F.; Glaser, T.; Doss, L.; Zhou, M.; Cunningham, D.; Shimel, K.; Harrington, M.; Hammel, K.; Cukras, C. A.; Ferris, F. L.; Chew, E. Y. Treatment of Geographic Atrophy With Subconjunctival Sirolimus: Results of a Phase I/II Clinical Trial. *Invest. Ophthalmol. Vis. Sci.* **2013**, *54* (4), 2941. https://doi.org/10.1167/iovs.13-11650.

(100) Liao, D. S.; Grossi, F. V.; El Mehdi, D.; Gerber, M. R.; Brown, D. M.; Heier, J. S.; Wykoff, C. C.; Singerman, L. J.; Abraham, P.; Grassmann, F.; Nuernberg, P.; Weber, B. H. F.; Deschatelets, P.; Kim, R. Y.; Chung, C. Y.; Ribeiro, R. M.; Hamdani, M.; Rosenfeld, P. J.; Boyer, D. S.; Slakter, J. S.; Francois, C. G. Complement C3 Inhibitor Pegcetacoplan for Geographic Atrophy Secondary to Age-Related Macular Degeneration. *Ophthalmology* **2020**, *127* (2), 186–195. https://doi.org/10.1016/j.ophtha.2019.07.011.

(101) Ellis, S.; Buchberger, A.; Holder, J.; Orhan, elise; Hughes, J. GT005, a Gene Therapy for the Treatment of Dry Age-Related Macular Degeneration (AMD). *Investigative Ophthalmology & Visual Science* **2020**, *61* (7), 2295–2295.

(102) Schwartz, S. D.; Regillo, C. D.; Lam, B. L.; Eliott, D.; Rosenfeld, P. J.; Gregori, N. Z.; Hubschman, J.-P.; Davis, J. L.; Heilwell, G.; Spirn, M.; Maguire, J.; Gay, R.; Bateman, J.; Ostrick, R. M.; Morris, D.; Vincent, M.; Anglade, E.; Del Priore, L. V.; Lanza, R. Human Embryonic Stem Cell-Derived Retinal Pigment Epithelium in Patients with Age-Related Macular Degeneration and Stargardt's Macular Dystrophy: Follow-up of Two Open-Label Phase 1/2 Studies. *The Lancet* **2015**, *385* (9967), 509–516. https://doi.org/10.1016/S0140-6736(14)61376-3.

(103) Kubota, R.; Boman, N. L.; David, R.; Mallikaarjun, S.; Patil, S.; Birch, D. SAFETY AND EFFECT ON ROD FUNCTION OF ACU-4429, A NOVEL SMALL-MOLECULE VISUAL CYCLE MODULATOR. *Retina* **2012**, *32* (1), 183–188. https://doi.org/10.1097/IAE.0b013e318217369e.

(104) Mata, N. L.; Lichter, J. B.; Vogel, R.; Han, Y.; Bui, T. V.; Singerman, L. J. INVESTIGATION OF ORAL FENRETINIDE FOR TREATMENT OF GEOGRAPHIC ATROPHY IN AGE-RELATED MACULAR DEGENERATION. *Retina* **2013**, *33* (3), 498–507. https://doi.org/10.1097/IAE.0b013e318265801d.

(105) Wong, W. T.; Kam, W.; Cunningham, D.; Harrington, M.; Hammel, K.; Meyerle, C. B.; Cukras, C.; Chew, E. Y.; Sadda, S. R.; Ferris, F. L. Treatment of Geographic Atrophy by the Topical Administration of OT-551: Results of a Phase II Clinical Trial. *Invest. Ophthalmol. Vis. Sci.* **2010**, *51* (12), 6131. https://doi.org/10.1167/iovs.10-5637.

(106) Zhang, K.; Hopkins, J. J.; Heier, J. S.; Birch, D. G.; Halperin, L. S.; Albini, T. A.; Brown, D. M.; Jaffe, G. J.; Tao, W.; Williams, G. A. Ciliary Neurotrophic Factor Delivered by Encapsulated Cell Intraocular Implants for Treatment of Geographic Atrophy in Age-Related Macular Degeneration. *Proc. Natl. Acad. Sci. U.S.A.* **2011**, *108* (15), 6241–6245. https://doi.org/10.1073/pnas.1018987108.

(107) Schwartz, S. D.; Hubschman, J.-P.; Heilwell, G.; Franco-Cardenas, V.; Pan, C. K.; Ostrick, R. M.; Mickunas, E.; Gay, R.; Klimanskaya, I.; Lanza, R. Embryonic Stem Cell Trials for Macular Degeneration: A Preliminary Report. *The Lancet* **2012**, *379* (9817), 713–720. https://doi.org/10.1016/S0140-6736(12)60028-2.

(108) Tufail, A.; Patel, P. J.; Egan, C.; Hykin, P.; Da Cruz, L.; Gregor, Z.; Dowler, J.; Majid, M. A.; Bailey, C.; Mohamed, Q.; Johnston, R.; Bunce, C.; Xing, W.; ABC Trial Investigators. Bevacizumab for Neovascular Age Related Macular Degeneration (ABC Trial): Multicentre Randomised Double Masked Study. *BMJ* **2010**, *340* (jun09 4), c2459–c2459. https://doi.org/10.1136/bmj.c2459.

(109) Rosenfeld, P. J.; Brown, D. M.; Heier, J. S.; Boyer, D. S.; Kaiser, P. K.; Chung, C. Y.; Kim, R. Y. Ranibizumab for Neovascular Age-Related Macular Degeneration. *N Engl J Med* **2006**, *355* (14), 1419–1431. https://doi.org/10.1056/NEJMoa054481.

(110) Kaiser, P. K.; Blodi, B. A.; Shapiro, H.; Acharya, N. R. Angiographic and Optical Coherence Tomographic Results of the MARINA Study of Ranibizumab in Neovascular Age-Related Macular Degeneration. *Ophthalmology* **2007**, *114* (10), 1868-1875.e4. https://doi.org/10.1016/j.ophtha.2007.04.030.

(111) Dugel, P. U.; Jaffe, G. J.; Sallstig, P.; Warburton, J.; Weichselberger, A.; Wieland, M.; Singerman, L. Brolucizumab Versus Aflibercept in Participants with Neovascular Age-Related Macular Degeneration: A Randomized Trial. *Ophthalmology* **2017**, *124* (9), 1296–1304. https://doi.org/10.1016/j.ophtha.2017.03.057.

(112) Sun, X.; Yang, S.; Zhao, J. Resistance to Anti-VEGF Therapy in Neovascular Age-Related Macular Degeneration: A Comprehensive Review. *DDDT* **2016**, 1857. https://doi.org/10.2147/DDDT.S97653.

(113) Van Asten, F.; Michels, C. T. J.; Hoyng, C. B.; Van Der Wilt, G. J.; Klevering, B. J.; Rovers, M. M.; Grutters, J. P. C. The Cost-Effectiveness of Bevacizumab, Ranibizumab and Aflibercept for the Treatment of Age-Related Macular Degeneration—A Cost-Effectiveness Analysis from a Societal Perspective. *PLoS ONE* **2018**, *13* (5), e0197670. https://doi.org/10.1371/journal.pone.0197670.

(114) Patel, S. S.; Sahni, J.; Sadikhov, S.; Pauly-Evers, M.; Szczesny, P.; Weikert, R. Anti-VEGF/Anti-Angiopoietin-2 Bispecific Antibody RG7716 in Diabetic Macular Edema: Complete 36-Week Results from the Phase 2, Multicenter, Randomized, Active Treatment-Controlled BOULEVARD Clinical Trial. *Investigative Ophthalmology & Visual Science* **2018**, *59* (9), 1959–1959.

(115) Stumpp, M. T.; Binz, H. K.; Amstutz, P. DARPins: A New Generation of Protein Therapeutics. *Drug Discovery Today* **2008**, *13* (15–16), 695–701. https://doi.org/10.1016/j.drudis.2008.04.013.

(116) Ricci, F.; Bandello, F.; Navarra, P.; Staurenghi, G.; Stumpp, M.; Zarbin, M. Neovascular Age-Related Macular Degeneration: Therapeutic Management and New-Upcoming Approaches. *IJMS* **2020**, *21* (21), 8242. https://doi.org/10.3390/ijms21218242.

(117) Yue, L.; Weiland, J. D.; Roska, B.; Humayun, M. S. Retinal Stimulation Strategies to Restore Vision: Fundamentals and Systems. *Progress in Retinal and Eye Research* **2016**, *53*, 21–47. https://doi.org/10.1016/j.preteyeres.2016.05.002.

(118) Schaffrath, K.; Lohmann, T.; Seifert, J.; Ingensiep, C.; Raffelberg, P.; Waschkowski, F.; Viga, R.; Kokozinski, R.; Mokwa, W.; Johnen, S.; Walter, P. New Epiretinal Implant with Integrated Sensor Chips for Optical Capturing Shows a Good Biocompatibility Profile in Vitro and in Vivo. *BioMed Eng OnLine* **2021**, *20* (1), 102. https://doi.org/10.1186/s12938-021-00938-9.

(119) Opie, N. L.; Burkitt, A. N.; Meffin, H.; Grayden, D. B. Heating of the Eye by a Retinal Prosthesis: Modeling, Cadaver and In Vivo Study. *IEEE Trans. Biomed. Eng.* **2012**, *59* (2), 339–345. https://doi.org/10.1109/TBME.2011.2171961.

(120) Yue, L.; Falabella, P.; Christopher, P.; Wuyyuru, V.; Dorn, J.; Schor, P.; Greenberg, R. J.; Weiland, J. D.; Humayun, M. S. Ten-Year Follow-up of a Blind Patient Chronically Implanted with Epiretinal Prosthesis Argus I. *Ophthalmology* **2015**, *122* (12), 2545-2552.e1. https://doi.org/10.1016/j.ophtha.2015.08.008.

(121) Yanai, D.; Weiland, J. D.; Mahadevappa, M.; Greenberg, R. J.; Fine, I.; Humayun, M. S. Visual Performance Using a Retinal Prosthesis in Three Subjects With Retinitis Pigmentosa. *American Journal of Ophthalmology* **2007**, *143* (5), 820-827.e2. https://doi.org/10.1016/j.ajo.2007.01.027.

(122) Humayun, M. S.; Dorn, J. D.; Da Cruz, L.; Dagnelie, G.; Sahel, J.-A.; Stanga, P. E.; Cideciyan, A. V.; Duncan, J. L.; Eliott, D.; Filley, E.; Ho, A. C.; Santos, A.; Safran, A. B.; Arditi, A.; Del Priore, L. V.; Greenberg, R. J. Interim Results from the International Trial of Second Sight's Visual Prosthesis. *Ophthalmology* **2012**, *119* (4), 779–788. https://doi.org/10.1016/j.ophtha.2011.09.028.

(123) Da Cruz, L.; Dorn, J. D.; Humayun, M. S.; Dagnelie, G.; Handa, J.; Barale, P.-O.; Sahel, J.-A.; Stanga, P. E.; Hafezi, F.; Safran, A. B.; Salzmann, J.; Santos, A.; Birch, D.; Spencer, R.; Cideciyan, A. V.; De Juan, E.; Duncan, J. L.; Eliott, D.; Fawzi, A.; Olmos De Koo, L. C.; Ho, A. C.; Brown, G.; Haller, J.; Regillo, C.; Del Priore, L. V.; Arditi, A.; Greenberg, R. J. Five-Year Safety and Performance Results from the Argus II Retinal Prosthesis System Clinical Trial. *Ophthalmology* **2016**, *123* (10), 2248–2254. https://doi.org/10.1016/j.ophtha.2016.06.049.

(124) Keserü, M.; Feucht, M.; Bornfeld, N.; Laube, T.; Walter, P.; Rössler, G.; Velikay-Parel, M.; Hornig, R.; Richard, G. Acute Electrical Stimulation of the Human Retina with an Epiretinal Electrode Array. *Acta Ophthalmologica* **2012**, *90* (1), e1–e8. https://doi.org/10.1111/j.1755-3768.2011.02288.x.

(125) Richard, G.; Feucht, M.; Bornfeld, N.; Laube, T.; Rössler, G.; Velikay–Parel, M.; Hornig, R. Multicenter Study on Acute Electrical Stimulation of the Human Retina With an Epiretinal Implant: Clinical Results in 20 Patients. *Investigative Ophthalmology & Visual Science* **2005**, *46* (13), 1143–1143.

(126) Richard, G.; Keserue, M.; Feucht, M.; Post, N.; Hornig, R. Visual Perception After Long-Term Implantation of a Retinal Implant. *Investigative Ophthalmology & Visual Science* **2008**, *49* (13), 1786–1786.

(127) Keserue, M.; Post, N.; Hornig, R.; Zeitz, O.; Richard, G. Long Term Tolerability of the First Wireless Implant for Electrical Epiretinal Stimulation. *Investigative Ophthalmology & Visual Science* **2009**, *50* (13), 4226–4226.

(128) Eckmiller, R.; Neumann, D.; Baruth, O. Tunable Retina Encoders for Retina Implants: Why and How. *J. Neural Eng.* **2005**, *2* (1), S91–S104. https://doi.org/10.1088/1741-2560/2/1/011.

(129) Hornig, R.; Dapper, M.; Le Joliff, E.; Hill, R.; Ishaque, K.; Posch, C.; Benosman, R.; LeMer, Y.; Sahel, J.-A.; Picaud, S. Pixium Vision: First Clinical Results and Innovative Developments. In *Artificial Vision*; Gabel, V. P., Ed.; Springer International Publishing: Cham, 2017; pp 99–113. https://doi.org/10.1007/978-3-319-41876-6_8.

(130) Muqit, M. M. K.; Velikay-Parel, M.; Weber, M.; Dupeyron, G.; Audemard, D.; Corcostegui, B.; Sahel, J.; Le Mer, Y. Six-Month Safety and Efficacy of the Intelligent Retinal Implant System II Device in Retinitis Pigmentosa. *Ophthalmology* **2019**, *126* (4), 637–639. https://doi.org/10.1016/j.ophtha.2018.11.010.

(131) Schwarz, M.; Ewe, L.; Hauschild, R.; Hosticka, B. J.; Huppertz, J.; Kolnsberg, S.; Mokwa, W.; Trieu, H. K. Single Chip CMOS Imagers and Flexible Microelectronic Stimulators for a Retina Implant System. *Sensors and Actuators A: Physical* **2000**, *83* (1–3), 40–46. https://doi.org/10.1016/S0924-4247(00)00290-9.

(132) Roessler, G.; Laube, T.; Brockmann, C.; Kirschkamp, T.; Mazinani, B.; Goertz, M.; Koch, C.; Krisch, I.; Sellhaus, B.; Trieu, H. K.; Weis, J.; Bornfeld, N.; Ro¨thgen, H.; Messner, A.; Mokwa, W.; Walter, P. Implantation and Explantation of a Wireless Epiretinal Retina Implant Device: Observations during the EPIRET3 Prospective Clinical Trial. *Invest. Ophthalmol. Vis. Sci.* **2009**, *50* (6), 3003. https://doi.org/10.1167/iovs.08-2752.

(133) Waschkowski, F.; Hesse, S.; Rieck, A. C.; Lohmann, T.; Brockmann, C.; Laube, T.; Bornfeld, N.; Thumann, G.; Walter, P.; Mokwa, W.; Johnen, S.; Roessler, G. Development of Very Large Electrode Arrays for Epiretinal Stimulation (VLARS). *BioMed Eng OnLine* **2014**, *13* (1), 11. https://doi.org/10.1186/1475-925X-13-11.

(134) Lohmann, T. K.; Haiss, F.; Schaffrath, K.; Schnitzler, A.-C.; Waschkowski, F.; Barz, C.; Van Der Meer, A.-M.; Werner, C.; Johnen, S.; Laube, T.; Bornfeld, N.; Mazinani, B. E.; Rößler, G.; Mokwa, W.; Walter, P. The Very Large Electrode Array for Retinal Stimulation (VLARS)—A Concept Study. *J. Neural Eng.* **2019**, *16* (6), 066031. https://doi.org/10.1088/1741-2552/ab4113.

(135) Raffelberg, P.; Burkard, R.; Viga, R.; Mokwa, W.; Walter, P.; Grabmaier, A.; Kokozinski, R. Current Controlled CMOS Stimulator with Programmable Pulse Pattern for a Retina Implant. In *2018 14th Conference on Ph.D. Research in Microelectronics and Electronics (PRIME)*; IEEE: Prague, Czech Republic, 2018; pp 253–256. https://doi.org/10.1109/PRIME.2018.8430332.

(136) Raz-Prag, D.; Weinberger, D.; Gefen, R. Implantation Procedure for Retinal Prosthesis: Adaptation of Extracapsular Cataract Procedure. *Investigative Ophthalmology & Visual Science* **2014**, *55* (13), 1809–1809.

(137) Yanovitz, L.; Raz-Prag, D.; Eden, K.-O.; Saini, R.; Hanein, Y.; Gefen, R. Retinal Responses Evoked and Recorded with 3D Electrodes Designated for a Novel Prosthetic Device. *Investigative Ophthalmology & Visual Science* **2014**, *55* (13), 1808–1808.

(138) Shire, D. B.; Kelly, S. K.; Chen, J.; Doyle, P.; Gingerich, M. D.; Cogan, S. F.; Drohan, W. A.; Mendoza, O.; Theogarajan, L.; Wyatt, J. L.; Rizzo, J. F. Development and Implantation of a Minimally Invasive Wireless Subretinal Neurostimulator. *IEEE Trans. Biomed. Eng.* **2009**, *56* (10), 2502–2511. https://doi.org/10.1109/TBME.2009.2021401.

(139) Kelly, S. K.; Shire, D. B.; Jinghua Chen; Doyle, P.; Gingerich, M. D.; Drohan, W. A.; Theogarajan, L. S.; Cogan, S. F.; Wyatt, J. L.; Rizzo, J. F. Realization of a 15-Channel, Hermetically-Encased Wireless Subretinal Prosthesis for the Blind. In *2009 Annual International Conference of the IEEE Engineering in Medicine and Biology Society*; IEEE: Minneapolis, MN, 2009; pp 200–203. https://doi.org/10.1109/IEMBS.2009.5333619.

(140) Kelly, S. K.; Ellersick, W. F.; Krishnan, A.; Doyle, P.; Shire, D. B.; Wyatt, J. L.; Rizzo, J. F. Redundant Safety Features in a High-Channel-Count Retinal Neurostimulator. In *2014 IEEE Biomedical Circuits and Systems Conference (BioCAS) Proceedings*; IEEE: Lausanne, Switzerland, 2014; pp 216–219. https://doi.org/10.1109/BioCAS.2014.6981701.

(141) Chow, A. Y. The Artificial Silicon Retina Microchip for the Treatment of VisionLoss From Retinitis Pigmentosa. *Arch Ophthalmol* **2004**, *122* (4), 460. https://doi.org/10.1001/archopht.122.4.460.

(142) Pardue, M. T.; Phillips, M. J.; Yin, H.; Fernandes, A.; Cheng, Y.; Chow, A. Y.; Ball, S. L. Possible Sources of Neuroprotection Following Subretinal Silicon Chip Implantation in RCS Rats. *J. Neural Eng.* **2005**, *2* (1), S39–S47. https://doi.org/10.1088/1741-2560/2/1/006.

(143) Pardue, M. T.; Phillips, M. J.; Yin, H.; Sippy, B. D.; Webb-Wood, S.; Chow, A. Y.; Ball, S. L. Neuroprotective Effect of Subretinal Implants in the RCS Rat. *Invest. Ophthalmol. Vis. Sci.* **2005**, *46* (2), 674. https://doi.org/10.1167/iovs.04-0515.

(144) Chow, A. Y.; Bittner, A. K.; Pardue, M. T. The Artificial Silicon Retina in Retinitis Pigmentosa Patients (an American Ophthalmological Association Thesis). *Trans Am Ophthalmol Soc* **2010**, *108*, 120–154.

(145) Zrenner, E.; Bartz-Schmidt, K. U.; Benav, H.; Besch, D.; Bruckmann, A.; Gabel, V.-P.; Gekeler, F.; Greppmaier, U.; Harscher, A.; Kibbel, S.; Koch, J.; Kusnyerik, A.; Peters, T.; Stingl, K.; Sachs, H.; Stett, A.; Szurman, P.; Wilhelm, B.; Wilke, R. Subretinal Electronic Chips Allow Blind Patients to Read Letters and Combine Them to Words. *Proc. R. Soc. B.* **2011**, *278* (1711), 1489–1497. https://doi.org/10.1098/rspb.2010.1747.

(146) Zrenner, E.; Bartz-Schmidt, K. U.; Besch, D.; Gekeler, F.; Koitschev, A.; Sachs, H. G.; Stingl, K. The Subretinal Implant ALPHA: Implantation and Functional Results. In *Artificial Vision*; Gabel, V. P., Ed.; Springer International Publishing: Cham, 2017; pp 65–83. https://doi.org/10.1007/978-3-319-41876-6_6.

(147) Kitiratschky, V. B. D.; Stingl, K.; Wilhelm, B.; Peters, T.; Besch, D.; Sachs, H.; Gekeler, F.; Bartz-Schmidt, K. U.; Zrenner, E. Safety Evaluation of "Retina Implant Alpha IMS"—a Prospective Clinical Trial. *Graefes Arch Clin Exp Ophthalmol* **2015**, *253* (3), 381–387. https://doi.org/10.1007/s00417-014-2797-x.

(148) Stingl, K.; Schippert, R.; Bartz-Schmidt, K. U.; Besch, D.; Cottriall, C. L.; Edwards, T. L.; Gekeler, F.; Greppmaier, U.; Kiel, K.; Koitschev, A.; Kühlewein, L.; MacLaren, R. E.; Ramsden, J. D.; Roider, J.; Rothermel, A.; Sachs, H.; Schröder, G. S.; Tode, J.; Troelenberg, N.; Zrenner, E. Interim Results of a Multicenter Trial with the New Electronic Subretinal Implant Alpha AMS in 15 Patients Blind from Inherited Retinal Degenerations. *Front. Neurosci.* **2017**, *11*, 445. https://doi.org/10.3389/fnins.2017.00445.

(149) Stingl, K.; Bartz-Schmidt, K. U.; Braun, A.; Gekeler, F.; Greppmaier, U.; Schatz, A.; Stett, A.; Strasser, T.; Kitiratschky, V.; Zrenner, E. Transfer Characteristics of Subretinal Visual Implants: Corneally Recorded Implant Responses. *Doc Ophthalmol* **2016**, *133* (2), 81–90. https://doi.org/10.1007/s10633-016-9557-7.

(150) Wang, L.; Mathieson, K.; Kamins, T. I.; Loudin, J. D.; Galambos, L.; Goetz, G.; Sher, A.; Mandel, Y.; Huie, P.; Lavinsky, D.; Harris, J. S.; Palanker, D. V. Photovoltaic Retinal Prosthesis: Implant Fabrication and Performance. *J. Neural Eng.* **2012**, *9* (4), 046014. https://doi.org/10.1088/1741-2560/9/4/046014.

(151) Mandel, Y.; Goetz, G.; Lavinsky, D.; Huie, P.; Mathieson, K.; Wang, L.; Kamins, T.; Galambos, L.; Manivanh, R.; Harris, J.; Palanker, D. Cortical Responses Elicited by Photovoltaic Subretinal Prostheses Exhibit Similarities to Visually Evoked Potentials. *Nat Commun* **2013**, *4* (1), 1980. https://doi.org/10.1038/ncomms2980.

(152) Palanker, D.; Le Mer, Y.; Mohand-Said, S.; Muqit, M.; Sahel, J. A. Photovoltaic Restoration of Central Vision in Atrophic Age-Related Macular Degeneration. *Ophthalmology* **2020**, *127* (8), 1097–1104. https://doi.org/10.1016/j.ophtha.2020.02.024.

(153) Palanker, D.; Le Mer, Y.; Mohand-Said, S.; Sahel, J. A. Simultaneous Perception of Prosthetic and Natural Vision in AMD Patients. *Nat Commun* **2022**, *13* (1), 513. https://doi.org/10.1038/s41467-022-28125-x.

(154) Bloch, E.; Luo, Y.; Da Cruz, L. Advances in Retinal Prosthesis Systems. *Ophthalmol Eye Dis* **2019**, *11*, 251584141881750. https://doi.org/10.1177/2515841418817501.

(155) Huang, T. W.; Kamins, T. I.; Chen, Z. C.; Wang, B.-Y.; Bhuckory, M.; Galambos, L.; Ho, E.; Ling, T.; Afshar, S.; Shin, A.; Zuckerman, V.; Harris, J. S.; Mathieson, K.; Palanker, D. Vertical-Junction Photodiodes for Smaller Pixels in Retinal Prostheses. *J. Neural Eng.* **2021**, *18* (3), 036015. https://doi.org/10.1088/1741-2552/abe6b8.

(156) Fujikado, T.; Kamei, M.; Sakaguchi, H.; Kanda, H.; Endo, T.; Hirota, M.; Morimoto, T.; Nishida, K.; Kishima, H.; Terasawa, Y.; Oosawa, K.; Ozawa, M.; Nishida, K. One-Year Outcome of 49-Channel Suprachoroidal–Transretinal Stimulation Prosthesis in Patients With Advanced Retinitis Pigmentosa. *Invest. Ophthalmol. Vis. Sci.* **2016**, *57* (14), 6147. https://doi.org/10.1167/iovs.16-20367.

(157) Eggenberger, S. C.; James, N. L.; Ho, C.; Eamegdool, S. S.; Tatarinoff, V.; Craig, N. A.; Gow, B. S.; Wan, S.; Dodds, C. W. D.; La Hood, D.; Gilmour, A.; Donahoe, S. L.; Krockenberger, M.; Tumuluri, K.; Da Cruz, M. J.; Grigg, J. R.; McCluskey, P.; Lovell, N. H.; Madigan, M. C.; Fung, A. T.; Suaning, G. J. Implantation and Long-Term Assessment of the Stability and Biocompatibility of a Novel 98 Channel Suprachoroidal Visual Prosthesis in Sheep. *Biomaterials* **2021**, *279*, 121191. https://doi.org/10.1016/j.biomaterials.2021.121191.

(158) Ayton, L. N.; Blamey, P. J.; Guymer, R. H.; Luu, C. D.; Nayagam, D. A. X.; Sinclair, N. C.; Shivdasani, M. N.; Yeoh, J.; McCombe, M. F.; Briggs, R. J.; Opie, N. L.; Villalobos, J.; Dimitrov, P. N.; Varsamidis, M.; Petoe, M. A.; McCarthy, C. D.; Walker, J. G.; Barnes, N.; Burkitt, A. N.; Williams, C. E.; Shepherd, R. K.; Allen, P. J.; for the Bionic Vision Australia Research Consortium. First-in-Human Trial of a Novel Suprachoroidal Retinal Prosthesis. *PLoS ONE* **2014**, *9* (12), e115239. https://doi.org/10.1371/journal.pone.0115239.

(159) Villalobos, J.; Nayagam, D. A. X.; Allen, P. J.; McKelvie, P.; Luu, C. D.; Ayton, L. N.; Freemantle, A. L.; McPhedran, M.; Basa, M.; McGowan, C. C.; Shepherd, R. K.; Williams, C. E. A Wide-Field Suprachoroidal Retinal Prosthesis Is Stable and Well Tolerated Following Chronic Implantation. *Invest. Ophthalmol. Vis. Sci.* **2013**, *54* (5), 3751. https://doi.org/10.1167/iovs.12-10843.

(160) Petoe, M. A.; Titchener, S. A.; Kolic, M.; Kentler, W. G.; Abbott, C. J.; Nayagam, D. A. X.; Baglin, E. K.; Kvansakul, J.; Barnes, N.; Walker, J. G.; Epp, S. B.; Young, K. A.; Ayton, L. N.; Luu, C. D.; Allen, P. J.; for the Bionics Institute and Centre for Eye Research Australia Retinal Prosthesis Consortium. A Second-Generation (44-Channel) Suprachoroidal Retinal Prosthesis: Interim Clinical Trial Results. *Trans. Vis. Sci. Tech.* **2021**, *10* (10), 12. https://doi.org/10.1167/tvst.10.10.12.

(161) Petoe, M. A.; McCarthy, C. D.; Shivdasani, M. N.; Sinclair, N. C.; Scott, A. F.; Ayton, L. N.; Barnes, N. M.; Guymer, R. H.; Allen, P. J.; Blamey, P. J.; for the Bionic Vision Australia Consortium. Determining the Contribution of Retinotopic Discrimination to Localization Performance With a Suprachoroidal Retinal Prosthesis. *Invest. Ophthalmol. Vis. Sci.* **2017**, *58* (7), 3231. https://doi.org/10.1167/iovs.16-21041.

(162) Shivdasani, M. N.; Sinclair, N. C.; Gillespie, L. N.; Petoe, M. A.; Titchener, S. A.; Fallon, J. B.; Perera, T.; Pardinas-Diaz, D.; Barnes, N. M.; Blamey, P. J.; for the Bionic Vision Australia Consortium. Identification of Characters and Localization of Images Using

Direct Multiple-Electrode Stimulation With a Suprachoroidal Retinal Prosthesis. *Invest. Ophthalmol. Vis. Sci.* **2017**, *58* (10), 3962. https://doi.org/10.1167/iovs.16-21311.

(163) Ayton, L. N.; Barnes, N.; Dagnelie, G.; Fujikado, T.; Goetz, G.; Hornig, R.; Jones, B. W.; Muqit, M. M. K.; Rathbun, D. L.; Stingl, K.; Weiland, J. D.; Petoe, M. A. An Update on Retinal Prostheses. *Clinical Neurophysiology* **2020**, *131* (6), 1383–1398. https://doi.org/10.1016/j.clinph.2019.11.029.

(164) Sinclair, N. C.; Shivdasani, M. N.; Perera, T.; Gillespie, L. N.; McDermott, H. J.; Ayton, L. N.; Blamey, P. J.; for the Bionic Vision Australia Consortium. The Appearance of Phosphenes Elicited Using a Suprachoroidal Retinal Prosthesis. *Invest. Ophthalmol. Vis. Sci.* **2016**, *57* (11), 4948. https://doi.org/10.1167/iovs.15-18991.

(165) Allen, P. J.; Ayton, L. N.; Yeoh, J.; Briggs, R.; Nayagam, D.; Williams, R.; Whitchurch, C.; Luu, C. D.; Shepherd, R.; Guymer, R. H.; Bionic Vision Australia Consortium. A Prototype Suprachoroidal Retinal Prosthesis: Device Reliability and Patient Safety Report of a 2 Year Clinical Study. *Investigative Ophthalmology & Visual Science* **2015**, *56* (7), 750–750.

(166) Barnes, N.; Scott, A. F.; Lieby, P.; Petoe, M. A.; McCarthy, C.; Stacey, A.; Ayton, L. N.; Sinclair, N. C.; Shivdasani, M. N.; Lovell, N. H.; McDermott, H. J.; Walker, J. G.; for the BVA Consortium. Vision Function Testing for a Suprachoroidal Retinal Prosthesis: Effects of Image Filtering. *J. Neural Eng.* **2016**, *13* (3), 036013. https://doi.org/10.1088/1741-2560/13/3/036013.

(167) Fujikado, T.; Morimoto, T.; Kanda, H.; Kusaka, S.; Nakauchi, K.; Ozawa, M.; Matsushita, K.; Sakaguchi, H.; Ikuno, Y.; Kamei, M.; Tano, Y. Evaluation of Phosphenes Elicited by Extraocular Stimulation in Normals and by Suprachoroidal-Transretinal Stimulation in Patients with Retinitis Pigmentosa. *Graefes Arch Clin Exp Ophthalmol* **2007**, *245* (10), 1411–1419. https://doi.org/10.1007/s00417-007-0563-z.

(168) Fujikado, T.; Kamei, M.; Sakaguchi, H.; Kanda, H.; Morimoto, T.; Ikuno, Y.; Nishida, K.; Kishima, H.; Maruo, T.; Konoma, K.; Ozawa, M.; Nishida, K. Testing of Semichronically Implanted Retinal Prosthesis by Suprachoroidal-Transretinal Stimulation in Patients with Retinitis Pigmentosa. *Invest. Ophthalmol. Vis. Sci.* **2011**, *52* (7), 4726. https://doi.org/10.1167/iovs.10-6836.

(169) Endo, T.; Fujikado, T.; Hirota, M.; Kanda, H.; Morimoto, T.; Nishida, K. Light Localization with Low-Contrast Targets in a Patient Implanted with a Suprachoroidal–Transretinal Stimulation Retinal Prosthesis. *Graefes Arch Clin Exp Ophthalmol* **2018**, *256* (9), 1723–1729. https://doi.org/10.1007/s00417-018-3982-0.

(170) Owens, R. M.; Malliaras, G. G. Organic Electronics at the Interface with Biology. *MRS Bull.* **2010**, *35* (6), 449–456. https://doi.org/10.1557/mrs2010.583.

(171) Inal, S.; Rivnay, J.; Suiu, A.-O.; Malliaras, G. G.; McCulloch, I. Conjugated Polymers in Bioelectronics. *Acc. Chem. Res.* **2018**, *51* (6), 1368–1376. https://doi.org/10.1021/acs.accounts.7b00624.

(172) Antognazza, M. R.; Di Paolo, M.; Ghezzi, D.; Mete, M.; Di Marco, S.; Maya-Vetencourt, J. F.; Maccarone, R.; Desii, A.; Di Fonzo, F.; Bramini, M.; Russo, A.; Laudato, L.; Donelli, I.; Cilli, M.; Freddi, G.; Pertile, G.; Lanzani, G.; Bisti, S.; Benfenati, F. Characterization of a Polymer-Based, Fully Organic Prosthesis for Implantation into the Subretinal Space of the Rat. *Adv. Healthcare Mater.* **2016**, *5* (17), 2271–2282. https://doi.org/10.1002/adhm.201600318.

(173) D'Cruz, P. M. Mutation of the Receptor Tyrosine Kinase Gene Mertk in the Retinal Dystrophic RCS Rat. *Human Molecular Genetics* **2000**, *9* (4), 645–651. https://doi.org/10.1093/hmg/9.4.645.

(174) Maya-Vetencourt, J. F.; Ghezzi, D.; Antognazza, M. R.; Colombo, E.; Mete, M.; Feyen, P.; Desii, A.; Buschiazzo, A.; Di Paolo, M.; Di Marco, S.; Ticconi, F.; Emionite, L.; Shmal,

D.; Marini, C.; Donelli, I.; Freddi, G.; Maccarone, R.; Bisti, S.; Sambuceti, G.; Pertile, G.; Lanzani, G.; Benfenati, F. A Fully Organic Retinal Prosthesis Restores Vision in a Rat Model of Degenerative Blindness. *Nature Mater* **2017**, *16* (6), 681–689. https://doi.org/10.1038/nmat4874.

(175) Ferlauto, L.; Airaghi Leccardi, M. J. I.; Chenais, N. A. L.; Gilliéron, S. C. A.; Vagni, P.; Bevilacqua, M.; Wolfensberger, T. J.; Sivula, K.; Ghezzi, D. Design and Validation of a Foldable and Photovoltaic Wide-Field Epiretinal Prosthesis. *Nat Commun* **2018**, *9* (1), 992. https://doi.org/10.1038/s41467-018-03386-7.

(176) Chenais, N. A. L.; Airaghi Leccardi, M. J. I.; Ghezzi, D. Photovoltaic Retinal Prosthesis Restores High-Resolution Responses to Single-Pixel Stimulation in Blind Retinas. *Commun Mater* **2021**, *2* (1), 28. https://doi.org/10.1038/s43246-021-00133-2.

(177) Vagni, P.; Airaghi Leccardi, M. J. I.; Vila, C.-H.; Zollinger, E. G.; Sherafatipour, G.; Wolfensberger, T. J.; Ghezzi, D. POLYRETINA Restores Light Responses in Vivo in Blind Göttingen Minipigs. *Nat Commun* **2022**, *13* (1), 3678. https://doi.org/10.1038/s41467-022-31180-z.

(178) Schaepdrijver, L. D.; Lauwers, H.; Simoens, P.; Geest, J. P. D. Development of the Retina in the Porcine Fetus A Light Microscopic Study. *Anatom Histol Embryol* **1990**, *19* (3), 222–235. https://doi.org/10.1111/j.1439-0264.1990.tb00884.x.

(179) Chandler, M. J. Photoreceptor Density of the Domestic Pig Retina. **1999**, *3*, 179–184.

(180) Sugawara, T.; Hagiwara, A.; Hiramatsu, A.; Ogata, K.; Mitamura, Y.; Yamamoto, S. Relationship between Peripheral Visual Field Loss and Vision-Related Quality of Life in Patients with Retinitis Pigmentosa. *Eye* **2010**, *24* (4), 535–539. https://doi.org/10.1038/eye.2009.176.

(181) Thorn, J. T.; Migliorini, E.; Ghezzi, D. Virtual Reality Simulation of Epiretinal Stimulation Highlights the Relevance of the Visual Angle in Prosthetic Vision. *J. Neural Eng.* **2020**, *17* (5), 056019. https://doi.org/10.1088/1741-2552/abb5bc.

(182) Sommerhalder, J.; Pérez Fornos, A. Prospects and Limitations of Spatial Resolution. In *Artificial Vision*; Gabel, V. P., Ed.; Springer International Publishing: Cham, 2017; pp 29–45. https://doi.org/10.1007/978-3-319-41876-6_4.

(183) Lorach, H.; Goetz, G.; Smith, R.; Lei, X.; Mandel, Y.; Kamins, T.; Mathieson, K.; Huie, P.; Harris, J.; Sher, A.; Palanker, D. Photovoltaic Restoration of Sight with High Visual Acuity. *Nat Med* **2015**, *21* (5), 476–482. https://doi.org/10.1038/nm.3851.

(184) Ghezzi, D.; Antognazza, M. R.; Maccarone, R.; Bellani, S.; Lanzarini, E.; Martino, N.; Mete, M.; Pertile, G.; Bisti, S.; Lanzani, G.; Benfenati, F. A Polymer Optoelectronic Interface Restores Light Sensitivity in Blind Rat Retinas. *Nature Photon* **2013**, *7* (5), 400–406. https://doi.org/10.1038/nphoton.2013.34.

(185) Antognazza, M. R.; Di Paolo, M.; Ghezzi, D.; Mete, M.; Di Marco, S.; Maya-Vetencourt, J. F.; Maccarone, R.; Desii, A.; Di Fonzo, F.; Bramini, M.; Russo, A.; Laudato, L.; Donelli, I.; Cilli, M.; Freddi, G.; Pertile, G.; Lanzani, G.; Bisti, S.; Benfenati, F. Characterization of a Polymer-Based, Fully Organic Prosthesis for Implantation into the Subretinal Space of the Rat. *Adv. Healthcare Mater.* **2016**, *5* (17), 2271–2282. https://doi.org/10.1002/adhm.201600318.

(186) Tang, J.; Qin, N.; Chong, Y.; Diao, Y.; Yiliguma; Wang, Z.; Xue, T.; Jiang, M.; Zhang, J.; Zheng, G. Nanowire Arrays Restore Vision in Blind Mice. *Nat Commun* **2018**, *9* (1), 786. https://doi.org/10.1038/s41467-018-03212-0.

(187) Airaghi Leccardi, M. J. I.; Chenais, N. A. L.; Ferlauto, L.; Kawecki, M.; Zollinger, E. G.; Ghezzi, D. Photovoltaic Organic Interface for Neuronal Stimulation in the Near-Infrared. *Commun Mater* **2020**, *1* (1), 21. https://doi.org/10.1038/s43246-020-0023-4.

(188) Nanduri, D.; Humayun, M. S.; Greenberg, R. J.; McMahon, M. J.; Weiland, J. D. Retinal Prosthesis Phosphene Shape Analysis. In *2008 30th Annual International*

Conference of the IEEE Engineering in Medicine and Biology Society; IEEE: Vancouver, BC, 2008; pp 1785–1788. https://doi.org/10.1109/IEMBS.2008.4649524.

(189) Luo, Y. H.-L.; Zhong, J. J.; Clemo, M.; Da Cruz, L. Long-Term Repeatability and Reproducibility of Phosphene Characteristics in Chronically Implanted Argus II Retinal Prosthesis Subjects. *American Journal of Ophthalmology* **2016**, *170*, 100–109. https://doi.org/10.1016/j.ajo.2016.07.021.

(190) Beyeler, M.; Nanduri, D.; Weiland, J. D.; Rokem, A.; Boynton, G. M.; Fine, I. A Model of Ganglion Axon Pathways Accounts for Percepts Elicited by Retinal Implants. *Sci Rep* **2019**, *9* (1), 9199. https://doi.org/10.1038/s41598-019-45416-4.

(191) Gogliettino, A. R.; Madugula, S. S.; Grosberg, L. E.; Vilkhu, R. S.; Brown, J.; Nguyen, H.; Kling, A.; Hottowy, P.; Dąbrowski, W.; Sher, A.; Litke, A. M.; Chichilnisky, E. J. *High-Fidelity Reproduction of Visual Signals by Electrical Stimulation in the Central Primate Retina*; preprint; Neuroscience, 2022. https://doi.org/10.1101/2022.05.24.493162.

(192) Cai, C.; Twyford, P.; Fried, S. The Response of Retinal Neurons to High-Frequency Stimulation. *J. Neural Eng.* **2013**, *10* (3), 036009. https://doi.org/10.1088/1741-2560/10/3/036009.

(193) Chenais, N. A. L.; Leccardi, M. J. I. A.; Ghezzi, D. Capacitive-like Photovoltaic Epiretinal Stimulation Enhances and Narrows the Network-Mediated Activity of Retinal Ganglion Cells by Recruiting the Lateral Inhibitory Network. *J. Neural Eng.* **2019**, *16* (6), 066009. https://doi.org/10.1088/1741-2552/ab3913.

(194) Weitz, A. C.; Nanduri, D.; Behrend, M. R.; Gonzalez-Calle, A.; Greenberg, R. J.; Humayun, M. S.; Chow, R. H.; Weiland, J. D. Improving the Spatial Resolution of Epiretinal Implants by Increasing Stimulus Pulse Duration. *Sci. Transl. Med.* **2015**, *7* (318). https://doi.org/10.1126/scitranslmed.aac4877.

(195) Behrend, M. R.; Ahuja, A. K.; Humayun, M. S.; Chow, R. H.; Weiland, J. D. Resolution of the Epiretinal Prosthesis Is Not Limited by Electrode Size. *IEEE Trans. Neural Syst. Rehabil. Eng.* **2011**, *19* (4), 436–442. https://doi.org/10.1109/TNSRE.2011.2140132.

(196) Yue, L.; Weiland, J. D.; Roska, B.; Humayun, M. S. Retinal Stimulation Strategies to Restore Vision: Fundamentals and Systems. *Progress in Retinal and Eye Research* **2016**, *53*, 21–47. https://doi.org/10.1016/j.preteyeres.2016.05.002.

(197) Ho, E.; Lei, X.; Flores, T.; Lorach, H.; Huang, T.; Galambos, L.; Kamins, T.; Harris, J.; Mathieson, K.; Palanker, D. Characteristics of Prosthetic Vision in Rats with Subretinal Flat and Pillar Electrode Arrays. *J. Neural Eng.* **2019**, *16* (6), 066027. https://doi.org/10.1088/1741-2552/ab34b3.

(198) Beauchamp, M. S.; Oswalt, D.; Sun, P.; Foster, B. L.; Magnotti, J. F.; Niketeghad, S.; Pouratian, N.; Bosking, W. H.; Yoshor, D. Dynamic Stimulation of Visual Cortex Produces Form Vision in Sighted and Blind Humans. *Cell* **2020**, *181* (4), 774-783.e5. https://doi.org/10.1016/j.cell.2020.04.033.

(199) Moleirinho, S.; Whalen, A. J.; Fried, S. I.; Pezaris, J. S. The Impact of Synchronous versus Asynchronous Electrical Stimulation in Artificial Vision. *J. Neural Eng.* **2021**, *18* (5), 051001. https://doi.org/10.1088/1741-2552/abecf1.

(200) Kagan, I.; Gur, M.; Snodderly, D. M. Saccades and Drifts Differentially Modulate Neuronal Activity in V1: Effects of Retinal Image Motion, Position, and Extraretinal Influences. *Journal of Vision* **2008**, *8* (14), 19–19. https://doi.org/10.1167/8.14.19.

(201) Greschner, M.; Bongard, M.; Rujan, P.; Ammermüller, J. Retinal Ganglion Cell Synchronization by Fixational Eye Movements Improves Feature Estimation. *Nat Neurosci* **2002**, *5* (4), 341–347. https://doi.org/10.1038/nn821.

(202) Freeman, D. K.; Fried, S. I. Multiple Components of Ganglion Cell Desensitization in Response to Prosthetic Stimulation. *J. Neural Eng.* **2011**, *8* (1), 016008. https://doi.org/10.1088/1741-2560/8/1/016008.

(203) Chenais, N. A. L.; Airaghi Leccardi, M. J. I.; Ghezzi, D. Naturalistic Spatiotemporal Modulation of Epiretinal Stimulation Increases the Response Persistence of Retinal Ganglion Cell. *J. Neural Eng.* **2021**, *18* (1), 016016. https://doi.org/10.1088/1741-2552/abcd6f.

(204) Jensen, R. J.; Rizzo, J. F. Responses of Ganglion Cells to Repetitive Electrical Stimulation of the Retina. *J. Neural Eng.* **2007**, *4* (1), S1–S6. https://doi.org/10.1088/1741-2560/4/1/S01.

(205) Chander, D.; Chichilnisky, E. J. Adaptation to Temporal Contrast in Primate and Salamander Retina. *J. Neurosci.* **2001**, *21* (24), 9904–9916. https://doi.org/10.1523/JNEUROSCI.21-24-09904.2001.

(206) Martinez-Conde, S.; Otero-Millan, J.; Macknik, S. L. The Impact of Microsaccades on Vision: Towards a Unified Theory of Saccadic Function. *Nat Rev Neurosci* **2013**, *14* (2), 83–96. https://doi.org/10.1038/nrn3405.

(207) Edwards, T. L.; Cottriall, C. L.; Xue, K.; Simunovic, M. P.; Ramsden, J. D.; Zrenner, E.; MacLaren, R. E. Assessment of the Electronic Retinal Implant Alpha AMS in Restoring Vision to Blind Patients with End-Stage Retinitis Pigmentosa. *Ophthalmology* **2018**, *125* (3), 432–443. https://doi.org/10.1016/j.ophtha.2017.09.019.

(208) Stronks, H. C.; Dagnelie, G. The Functional Performance of the Argus II Retinal Prosthesis. *Expert Review of Medical Devices* **2014**, *11* (1), 23–30. https://doi.org/10.1586/17434440.2014.862494.

(209) Caspi, A.; Roy, A.; Wuyyuru, V.; Rosendall, P. E.; Harper, J. W.; Katyal, K. D.; Barry, M. P.; Dagnelie, G.; Greenberg, R. J. Eye Movement Control in the Argus II Retinal-Prosthesis Enables Reduced Head Movement and Better Localization Precision. *Invest. Ophthalmol. Vis. Sci.* **2018**, *59* (2), 792. https://doi.org/10.1167/iovs.17-22377.

(210) Woeppel, K.; Yang, Q.; Cui, X. T. Recent Advances in Neural Electrode–Tissue Interfaces. *Current Opinion in Biomedical Engineering* **2017**, *4*, 21–31. https://doi.org/10.1016/j.cobme.2017.09.003.

(211) Airaghi Leccardi, M. J. I.; Ghezzi, D. Organic Electronics for Neuroprosthetics. *Healthcare Technology Letters* **2020**, *7* (3), 52–57. https://doi.org/10.1049/htl.2019.0108.

(212) Fernandez, E. Development of Visual Neuroprostheses: Trends and Challenges. *Bioelectron Med* **2018**, *4* (1), 12. https://doi.org/10.1186/s42234-018-0013-8.

(213) Damle, S.; Carleton, M.; Kapogianis, T.; Arya, S.; Cavichini-Corderio, M.; Freeman, W. R.; Lo, Y.-H.; Oesch, N. W. Minimizing Iridium Oxide Electrodes for High Visual Acuity Subretinal Stimulation. *eNeuro* **2021**, *8* (6), ENEURO.0506-20.2021. https://doi.org/10.1523/ENEURO.0506-20.2021.

(214) Corna, A.; Herrmann, T.; Zeck, G. Electrode-Size Dependent Thresholds in Subretinal Neuroprosthetic Stimulation. *J. Neural Eng.* **2018**, *15* (4), 045003. https://doi.org/10.1088/1741-2552/aac1c8.

(215) Kostarelos, K.; Vincent, M.; Hebert, C.; Garrido, J. A. Graphene in the Design and Engineering of Next-Generation Neural Interfaces. *Advanced Materials* **2017**, *29* (42), 1700909. https://doi.org/10.1002/adma.201700909.

(216) Zeng, Q.; Li, X.; Zhang, S.; Deng, C.; Wu, T. Think Big, See Small—A Review of Nanomaterials for Neural Interfaces. *Nano Select* **2022**, *3* (5), 903–918. https://doi.org/10.1002/nano.202100256.

(217) Wu, N.; Wan, S.; Su, S.; Huang, H.; Dou, G.; Sun, L. Electrode Materials for Brain–Machine Interface: A Review. *InfoMat* **2021**, *3* (11), 1174–1194. https://doi.org/10.1002/inf2.12234.

(218) Song, E.; Li, J.; Won, S. M.; Bai, W.; Rogers, J. A. Materials for Flexible Bioelectronic Systems as Chronic Neural Interfaces. *Nat. Mater.* **2020**, *19* (6), 590–603. https://doi.org/10.1038/s41563-020-0679-7.

(219) Fanelli, A.; Ghezzi, D. Transient Electronics: New Opportunities for Implantable Neurotechnology. *Current Opinion in Biotechnology* **2021**, *72*, 22–28. https://doi.org/10.1016/j.copbio.2021.08.011.

(220) Medagoda, D. I.; Ghezzi, D. Organic Semiconductors for Light-Mediated Neuromodulation. *Commun Mater* **2021**, *2* (1), 111. https://doi.org/10.1038/s43246-021-00217-z.

(221) Humayun, M. S.; Dorn, J. D.; Ahuja, A. K.; Caspi, A.; Filley, E.; Dagnelie, G.; Salzmann, J.; Santos, A.; Duncan, J.; daCruz, L.; Mohand-Said, S.; Eliott, D.; McMahon, M. J.; Greenberg, R. J. Preliminary 6 Month Results from the Argus^{tm} Ii Epiretinal Prosthesis Feasibility Study. In *2009 Annual International Conference of the IEEE Engineering in Medicine and Biology Society*; IEEE: Minneapolis, MN, 2009; pp 4566–4568. https://doi.org/10.1109/IEMBS.2009.5332695.

(222) Shire, D. B.; Ellersick, W.; Kelly, S. K.; Doyle, P.; Priplata, A.; Drohan, W.; Mendoza, O.; Gingerich, M.; McKee, B.; Wyatt, J. L.; Rizzo, J. F. ASIC Design and Data Communications for the Boston Retinal Prosthesis. In *2012 Annual International Conference of the IEEE Engineering in Medicine and Biology Society*; IEEE: San Diego, CA, 2012; pp 292–295. https://doi.org/10.1109/EMBC.2012.6345927.

(223) Wang, J.; Zhu, H.; Liu, J.; Li, H.; Han, Y.; Zhou, R.; Zhang, Y. The Application of Computer Vision to Visual Prosthesis. *Artificial Organs* **2021**, *45* (10), 1141–1154. https://doi.org/10.1111/aor.14022.

(224) Lozano, A.; Suárez, J. S.; Soto-Sánchez, C.; Garrigós, J.; Martínez-Alvarez, J. J.; Ferrández, J. M.; Fernández, E. Neurolight: A Deep Learning Neural Interface for Cortical Visual Prostheses. *Int. J. Neur. Syst.* **2020**, *30* (09), 2050045. https://doi.org/10.1142/S0129065720500458.

(225) De Ruyter Van Steveninck, J.; Güçlü, U.; Van Wezel, R.; Van Gerven, M. End-to-End Optimization of Prosthetic Vision. *Journal of Vision* **2022**, *22* (2), 20. https://doi.org/10.1167/jov.22.2.20.

(226) Shah, N. P.; Chichilnisky, E. J. Computational Challenges and Opportunities for a Bi-Directional Artificial Retina. *J. Neural Eng.* **2020**, *17* (5), 055002. https://doi.org/10.1088/1741-2552/aba8b1.

(227) Rincón Montes, V.; Gehlen, J.; Ingebrandt, S.; Mokwa, W.; Walter, P.; Müller, F.; Offenhäusser, A. Development and in Vitro Validation of Flexible Intraretinal Probes. *Sci Rep* **2020**, *10* (1), 19836. https://doi.org/10.1038/s41598-020-76582-5.

(228) Barbruni, G. L.; Ros, P. M.; Demarchi, D.; Carrara, S.; Ghezzi, D. Miniaturised Wireless Power Transfer Systems for Neurostimulation: A Review. *IEEE Trans. Biomed. Circuits Syst.* **2020**, *14* (6), 1160–1178. https://doi.org/10.1109/TBCAS.2020.3038599.

(229) Merabet, L. B.; Rizzo, J. F.; Amedi, A.; Somers, D. C.; Pascual-Leone, A. What Blindness Can Tell Us about Seeing Again: Merging Neuroplasticity and Neuroprostheses. *Nat Rev Neurosci* **2005**, *6* (1), 71–77. https://doi.org/10.1038/nrn1586.

(230) Beyeler, M.; Rokem, A.; Boynton, G. M.; Fine, I. Learning to See Again: Biological Constraints on Cortical Plasticity and the Implications for Sight Restoration Technologies. *J. Neural Eng.* **2017**, *14* (5), 051003. https://doi.org/10.1088/1741-2552/aa795e.

(231) Vargas-Martı´n, F.; Peli, E. Eye Movements of Patients with Tunnel Vision While Walking. *Invest. Ophthalmol. Vis. Sci.* **2006**, *47* (12), 5295. https://doi.org/10.1167/iovs.05-1043.

(232) Dulin, D.; Hatwell, Y.; Pylyshyn, Z.; Chokron, S. Effects of Peripheral and Central Visual Impairment on Mental Imagery Capacity. *Neuroscience & Biobehavioral Reviews* **2008**, *32* (8), 1396–1408. https://doi.org/10.1016/j.neubiorev.2008.04.007.

(233) Jones, B. W.; Marc, R. E. Retinal Remodeling during Retinal Degeneration. *Experimental Eye Research* **2005**, *81* (2), 123–137. https://doi.org/10.1016/j.exer.2005.03.006.

(234) Jones, B. W.; Watt, C. B.; Frederick, J. M.; Baehr, W.; Chen, C.-K.; Levine, E. M.; Milam, A. H.; Lavail, M. M.; Marc, R. E. Retinal Remodeling Triggered by Photoreceptor Degenerations. *J. Comp. Neurol.* **2003**, *464* (1), 1–16. https://doi.org/10.1002/cne.10703.

(235) Finn, A.; Grewal, D.; Vajzovic, L. Argus II Retinal Prosthesis System: A Review of Patient Selection Criteria, Surgical Considerations, and Post-Operative Outcomes. *OPTH* **2018**, *Volume 12*, 1089–1097. https://doi.org/10.2147/OPTH.S137525.

(236) Naycheva, L.; Schatz, A.; Röck, T.; Willmann, G.; Messias, A.; Bartz-Schmidt, K. U.; Zrenner, E.; Gekeler, F. Phosphene Thresholds Elicited by Transcorneal Electrical Stimulation in Healthy Subjects and Patients with Retinal Diseases. *Invest. Ophthalmol. Vis. Sci.* **2012**, *53* (12), 7440. https://doi.org/10.1167/iovs.12-9612.

(237) Erickson-Davis, C.; Korzybska, H. What Do Blind People "See" with Retinal Prostheses? Observations and Qualitative Reports of Epiretinal Implant Users. *PLoS ONE* **2021**, *16* (2), e0229189. https://doi.org/10.1371/journal.pone.0229189.

(238) Anselmo, A. C.; Mitragotri, S. Nanoparticles in the Clinic. *Bioengineering & Translational Medicine* **2016**, *1* (1), 10–29. https://doi.org/10.1002/btm2.10003.

(239) Benfenati, F.; Lanzani, G. Clinical Translation of Nanoparticles for Neural Stimulation. *Nat Rev Mater* **2020**, *6* (1), 1–4. https://doi.org/10.1038/s41578-020-00267-8.

(240) Scarpa, G.; Idzko, A.-L.; Götz, S.; Thalhammer, S. Biocompatibility Studies of Functionalized Regioregular Poly(3-Hexylthiophene) Layers for Sensing Applications: Biocompatibility Studies of Functionalized Regioregular Poly(3-Hexylthiophene) Layers …. *Macromol. Biosci.* **2010**, *10* (4), 378–383. https://doi.org/10.1002/mabi.200900412.

(241) Tropp, J.; Rivnay, J. Design of Biodegradable and Biocompatible Conjugated Polymers for Bioelectronics. *J. Mater. Chem. C* **2021**, *9* (39), 13543–13556. https://doi.org/10.1039/D1TC03600A.

(242) Root, S. E.; Savagatrup, S.; Printz, A. D.; Rodriquez, D.; Lipomi, D. J. Mechanical Properties of Organic Semiconductors for Stretchable, Highly Flexible, and Mechanically Robust Electronics. *Chem. Rev.* **2017**, *117* (9), 6467–6499. https://doi.org/10.1021/acs.chemrev.7b00003.

(243) Wu, Y.; Shi, C.; Wang, G.; Sun, H.; Yin, S. Recent Advances in the Development and Applications of Conjugated Polymer Dots. *J. Mater. Chem. B* **2022**, *10* (16), 2995–3015. https://doi.org/10.1039/D1TB02816B.

(244) Feng, L.; Zhu, C.; Yuan, H.; Liu, L.; Lv, F.; Wang, S. Conjugated Polymer Nanoparticles: Preparation, Properties, Functionalization and Biological Applications. *Chem. Soc. Rev.* **2013**, *42* (16), 6620. https://doi.org/10.1039/c3cs60036j.

(245) Gmucová, K. Structural Properties versus Electronic Structure of Donor-Acceptor Alternating Copolymers: A Review. *Synthetic Metals* **2021**, *274*, 116718. https://doi.org/10.1016/j.synthmet.2021.116718.

(246) Zangoli, M.; Di Maria, F.; Zucchetti, E.; Bossio, C.; Antognazza, M. R.; Lanzani, G.; Mazzaro, R.; Corticelli, F.; Baroncini, M.; Barbarella, G. Engineering Thiophene-Based Nanoparticles to Induce Phototransduction in Live Cells under Illumination. *Nanoscale* **2017**, *9* (26), 9202–9209. https://doi.org/10.1039/C7NR01793F.

(247) Maya-Vetencourt, J. F.; Manfredi, G.; Mete, M.; Colombo, E.; Bramini, M.; Di Marco, S.; Shmal, D.; Mantero, G.; Dipalo, M.; Rocchi, A.; DiFrancesco, M. L.; Papaleo, E. D.;

Russo, A.; Barsotti, J.; Eleftheriou, C.; Di Maria, F.; Cossu, V.; Piazza, F.; Emionite, L.; Ticconi, F.; Marini, C.; Sambuceti, G.; Pertile, G.; Lanzani, G.; Benfenati, F. Subretinally Injected Semiconducting Polymer Nanoparticles Rescue Vision in a Rat Model of Retinal Dystrophy. *Nat. Nanotechnol.* **2020**, *15* (8), 698–708. https://doi.org/10.1038/s41565-020-0696-3.

(248) Francia, S.; Shmal, D.; Di Marco, S.; Chiaravalli, G.; Maya-Vetencourt, J. F.; Mantero, G.; Michetti, C.; Cupini, S.; Manfredi, G.; DiFrancesco, M. L.; Rocchi, A.; Perotto, S.; Attanasio, M.; Sacco, R.; Bisti, S.; Mete, M.; Pertile, G.; Lanzani, G.; Colombo, E.; Benfenati, F. Light-Induced Charge Generation in Polymeric Nanoparticles Restores Vision in Advanced-Stage Retinitis Pigmentosa Rats. *Nat Commun* **2022**, *13* (1), 3677. https://doi.org/10.1038/s41467-022-31368-3.

(249) Amgoth, C.; Phan, C.; Banavoth, M.; Rompivalasa, S.; Tang, G. Polymer Properties: Functionalization and Surface Modified Nanoparticles. In *Role of Novel Drug Delivery Vehicles in Nanobiomedicine*; K. Tyagi, R., Garg, N., Shukla, R., Singh Bisen, P., Eds.; IntechOpen, 2020. https://doi.org/10.5772/intechopen.84424.

(250) *Role of Novel Drug Delivery Vehicles in Nanobiomedicine*; K. Tyagi, R., Garg, N., Shukla, R., Singh Bisen, P., Eds.; IntechOpen, 2020. https://doi.org/10.5772/intechopen.77468.

(251) Landfester, K. SYNTHESIS OF COLLOIDAL PARTICLES IN MINIEMULSIONS. *Annu. Rev. Mater. Res.* **2006**, *36* (1), 231–279. https://doi.org/10.1146/annurev.matsci.36.032905.091025.

(252) Landfester, K. Miniemulsion Polymerization and the Structure of Polymer and Hybrid Nanoparticles. *Angew Chem Int Ed* **2009**, *48* (25), 4488–4507. https://doi.org/10.1002/anie.200900723.

(253) Müller, K.; Klapper, M.; Müllen, K. Synthesis of Conjugated Polymer Nanoparticles in Non-Aqueous Emulsions. *Macromol. Rapid Commun.* **2006**, *27* (8), 586–593. https://doi.org/10.1002/marc.200600027.

(254) Evans, D. F.; Wennerström, H. *The Colloidal Domain: Where Physics, Chemistry, Biology, and Technology Meet*, 2nd ed.; Advances in interfacial engineering series; Wiley-VCH: New York, 1999.

(255) Nagarjuna, G.; Baghgar, M.; Labastide, J. A.; Algaier, D. D.; Barnes, M. D.; Venkataraman, D. Tuning Aggregation of Poly(3-Hexylthiophene) within Nanoparticles. *ACS Nano* **2012**, *6* (12), 10750–10758. https://doi.org/10.1021/nn305207b.

(256) Labastide, J. A.; Baghgar, M.; Dujovne, I.; Venkatraman, B. H.; Ramsdell, D. C.; Venkataraman, D.; Barnes, M. D. Time- and Polarization-Resolved Photoluminescence of Individual Semicrystalline Polythiophene (P3HT) Nanoparticles. *J. Phys. Chem. Lett.* **2011**, *2* (17), 2089–2093. https://doi.org/10.1021/jz200958x.

(257) Ulum, S.; Holmes, N.; Darwis, D.; Burke, K.; David Kilcoyne, A. L.; Zhou, X.; Belcher, W.; Dastoor, P. Determining the Structural Motif of P3HT:PCBM Nanoparticulate Organic Photovoltaic Devices. *Solar Energy Materials and Solar Cells* **2013**, *110*, 43–48. https://doi.org/10.1016/j.solmat.2012.11.015.

(258) Burke, K. B.; Stapleton, A. J.; Vaughan, B.; Zhou, X.; Kilcoyne, A. L. D.; Belcher, W. J.; Dastoor, P. C. Scanning Transmission X-Ray Microscopy of Polymer Nanoparticles: Probing Morphology on Sub-10 Nm Length Scales. *Nanotechnology* **2011**, *22* (26), 265710. https://doi.org/10.1088/0957-4484/22/26/265710.

(259) Richards, J. J.; Whittle, C. L.; Shao, G.; Pozzo, L. D. Correlating Structure and Photocurrent for Composite Semiconducting Nanoparticles with Contrast Variation Small-Angle Neutron Scattering and Photoconductive Atomic Force Microscopy. *ACS Nano* **2014**, *8* (5), 4313–4324. https://doi.org/10.1021/nn405914g.

(260) Fessi, H.; Puisieux, F.; Devissaguet, J. Ph.; Ammoury, N.; Benita, S. Nanocapsule Formation by Interfacial Polymer Deposition Following Solvent Displacement. *International Journal of Pharmaceutics* **1989**, *55* (1), R1–R4. https://doi.org/10.1016/0378-5173(89)90281-0.

(261) Pecher, J.; Mecking, S. Nanoparticles of Conjugated Polymers. *Chem. Rev.* **2010**, *110* (10), 6260–6279. https://doi.org/10.1021/cr100132y.

(262) Tuncel, D.; Demir, H. V. Conjugated Polymer Nanoparticles. *Nanoscale* **2010**, *2* (4), 484. https://doi.org/10.1039/b9nr00374f.

(263) Zangoli, M.; Di Maria, F. Synthesis, Characterization, and Biological Applications of Semiconducting Polythiophene-based Nanoparticles. *VIEW* **2021**, *2* (1), 20200086. https://doi.org/10.1002/VIW.20200086.

(264) Rao, J. P.; Geckeler, K. E. Polymer Nanoparticles: Preparation Techniques and Size-Control Parameters. *Progress in Polymer Science* **2011**, *36* (7), 887–913. https://doi.org/10.1016/j.progpolymsci.2011.01.001.

(265) Liu, Y.; Lu, Y. C.; Luo, G. S. Modified Nanoprecipitation Method for Polysulfone Nanoparticles Preparation. *Soft Matter* **2014**, *10* (19), 3414. https://doi.org/10.1039/c3sm53003e.

(266) Lince, F.; Marchisio, D. L.; Barresi, A. A. Strategies to Control the Particle Size Distribution of Poly-ε-Caprolactone Nanoparticles for Pharmaceutical Applications. *Journal of Colloid and Interface Science* **2008**, *322* (2), 505–515. https://doi.org/10.1016/j.jcis.2008.03.033.

(267) Whitesides, G. M. The Origins and the Future of Microfluidics. *Nature* **2006**, *442* (7101), 368–373. https://doi.org/10.1038/nature05058.

(268) Valencia, P. M.; Farokhzad, O. C.; Karnik, R.; Langer, R. Microfluidic Technologies for Accelerating the Clinical Translation of Nanoparticles. *Nature Nanotech* **2012**, *7* (10), 623–629. https://doi.org/10.1038/nnano.2012.168.

(269) Karnik, R.; Gu, F.; Basto, P.; Cannizzaro, C.; Dean, L.; Kyei-Manu, W.; Langer, R.; Farokhzad, O. C. Microfluidic Platform for Controlled Synthesis of Polymeric Nanoparticles. *Nano Lett.* **2008**, *8* (9), 2906–2912. https://doi.org/10.1021/nl801736q.

(270) Kang, X.; Luo, C.; Wei, Q.; Xiong, C.; Chen, Q.; Chen, Y.; Ouyang, Q. Mass Production of Highly Monodisperse Polymeric Nanoparticles by Parallel Flow Focusing System. *Microfluid Nanofluid* **2013**, *15* (3), 337–345. https://doi.org/10.1007/s10404-013-1152-6.

(271) Vu, H. T. H.; Streck, S.; Hook, S. M.; McDowell, A. Utilization of Microfluidics for the Preparation of Polymeric Nanoparticles for the Antioxidant Rutin: A Comparison with Bulk Production. *PNT* **2019**, *7* (6), 469–483. https://doi.org/10.2174/2211738507666191019141049.

(272) Wang, Z.; Guo, B.; Middha, E.; Huang, Z.; Hu, Q.; Fu, Z.; Liu, B. Microfluidics-Prepared Uniform Conjugated Polymer Nanoparticles for Photo-Triggered Immune Microenvironment Modulation and Cancer Therapy. *ACS Appl. Mater. Interfaces* **2019**, *11* (12), 11167–11176. https://doi.org/10.1021/acsami.8b22579.

(273) Shang, L.; Cheng, Y.; Zhao, Y. Emerging Droplet Microfluidics. *Chem. Rev.* **2017**, *117* (12), 7964–8040. https://doi.org/10.1021/acs.chemrev.6b00848.

(274) Kuehne, A. J. C.; Weitz, D. A. Highly Monodisperse Conjugated Polymer Particles Synthesized with Drop-Based Microfluidics. *Chem. Commun.* **2011**, *47* (45), 12379. https://doi.org/10.1039/c1cc14251h.

(275) Ciftci, S.; Kuehne, A. J. C. Direct Synthesis of Conjugated Polymer Nanoparticles. In *Conjugated Polymers for Biological and Biomedical Applications*; Liu, B. L., Ed.; Wiley, 2018; pp 35–58. https://doi.org/10.1002/9783527342747.ch2.

(276) Crespy, D.; Landfester, K. Miniemulsion Polymerization as a Versatile Tool for the Synthesis of Functionalized Polymers. *Beilstein J. Org. Chem.* **2010**, *6*, 1132–1148. https://doi.org/10.3762/bjoc.6.130.
(277) Chern, C. S. Emulsion Polymerization Mechanisms and Kinetics. *Progress in Polymer Science* **2006**, *31* (5), 443–486. https://doi.org/10.1016/j.progpolymsci.2006.02.001.
(278) Puig, J. E. Microemulsion Polymerization (Oil-in Water). *Polymeric materials encyclopedia* **1996**, *6* (J.C. Salamone (Ed.)), 4333–4341.
(279) Sarov, Y.; Capek, I. Kinetic Events of (Micro)Emulsion Polymerization of Styrene. *Polym. Bull.* **2020**, *77* (9), 4851–4865. https://doi.org/10.1007/s00289-019-02976-9.
(280) Kawaguchi, S.; Ito, K. Dispersion Polymerization. In *Polymer Particles*; Okubo, M., Ed.; Advances in Polymer Science; Springer Berlin Heidelberg: Berlin, Heidelberg, 2005; Vol. 175, pp 299–328. https://doi.org/10.1007/b100118.
(281) Xia, Y.; Gates, B.; Yin, Y.; Lu, Y. Monodispersed Colloidal Spheres: Old Materials with New Applications. *Adv. Mater.* **2000**, *12* (10), 693–713. https://doi.org/10.1002/(SICI)1521-4095(200005)12:10<693::AID-ADMA693>3.0.CO;2-J.
(282) Di Maria, F.; Lodola, F.; Zucchetti, E.; Benfenati, F.; Lanzani, G. The Evolution of Artificial Light Actuators in Living Systems: From Planar to Nanostructured Interfaces. *Chem. Soc. Rev.* **2018**, *47* (13), 4757–4780. https://doi.org/10.1039/C7CS00860K.
(283) Zhang, Y.; Zhan, X.; Xiong, J.; Peng, S.; Huang, W.; Joshi, R.; Cai, Y.; Liu, Y.; Li, R.; Yuan, K.; Zhou, N.; Min, W. Temperature-Dependent Cell Death Patterns Induced by Functionalized Gold Nanoparticle Photothermal Therapy in Melanoma Cells. *Sci Rep* **2018**, *8* (1), 8720. https://doi.org/10.1038/s41598-018-26978-1.
(284) Kučerka, N.; Nieh, M.-P.; Katsaras, J. Fluid Phase Lipid Areas and Bilayer Thicknesses of Commonly Used Phosphatidylcholines as a Function of Temperature. *Biochimica et Biophysica Acta (BBA) - Biomembranes* **2011**, *1808* (11), 2761–2771. https://doi.org/10.1016/j.bbamem.2011.07.022.
(285) Pinto, B. I.; Bassetto, C. A. Z.; Bezanilla, F. Optocapacitance: Physical Basis and Its Application. *Biophys Rev* **2022**, *14* (2), 569–577. https://doi.org/10.1007/s12551-022-00943-9.
(286) Martino, N.; Feyen, P.; Porro, M.; Bossio, C.; Zucchetti, E.; Ghezzi, D.; Benfenati, F.; Lanzani, G.; Antognazza, M. R. Photothermal Cellular Stimulation in Functional Bio-Polymer Interfaces. *Sci Rep* **2015**, *5* (1), 8911. https://doi.org/10.1038/srep08911.
(287) Arrigoni, C.; Minor, D. L. Global versus Local Mechanisms of Temperature Sensing in Ion Channels. *Pflugers Arch - Eur J Physiol* **2018**, *470* (5), 733–744. https://doi.org/10.1007/s00424-017-2102-z.
(288) Caterina, M. J.; Schumacher, M. A.; Tominaga, M.; Rosen, T. A.; Levine, J. D.; Julius, D. The Capsaicin Receptor: A Heat-Activated Ion Channel in the Pain Pathway. *Nature* **1997**, *389* (6653), 816–824. https://doi.org/10.1038/39807.
(289) Kwon, D. H.; Zhang, F.; Suo, Y.; Bouvette, J.; Borgnia, M. J.; Lee, S.-Y. Heat-Dependent Opening of TRPV1 in the Presence of Capsaicin. *Nat Struct Mol Biol* **2021**, *28* (7), 554–563. https://doi.org/10.1038/s41594-021-00616-3.
(290) Lyu, Y.; Xie, C.; Chechetka, S. A.; Miyako, E.; Pu, K. Semiconducting Polymer Nanobioconjugates for Targeted Photothermal Activation of Neurons. *J. Am. Chem. Soc.* **2016**, *138* (29), 9049–9052. https://doi.org/10.1021/jacs.6b05192.
(291) Feyen, P.; Colombo, E.; Endeman, D.; Nova, M.; Laudato, L.; Martino, N.; Antognazza, M. R.; Lanzani, G.; Benfenati, F.; Ghezzi, D. Light-Evoked Hyperpolarization and Silencing of Neurons by Conjugated Polymers. *Sci Rep* **2016**, *6* (1), 22718. https://doi.org/10.1038/srep22718.

(292) Lodola, F.; Martino, N.; Tullii, G.; Lanzani, G.; Antognazza, M. R. Conjugated Polymers Mediate Effective Activation of the Mammalian Ion Channel Transient Receptor Potential Vanilloid 1. *Sci Rep* **2017**, *7* (1), 8477. https://doi.org/10.1038/s41598-017-08541-6.

(293) Guenther, S.; Reeh, P. W.; Kress, M. Rises in [Ca^{2+}]$_i$ Mediate Capsaicin- and Proton-Induced Heat Sensitization of Rat Primary Nociceptive Neurons: Capsaicin, Acidosis and Nociceptor Sensitization. *European Journal of Neuroscience* **1999**, *11* (9), 3143–3150. https://doi.org/10.1046/j.1460-9568.1999.00734.x.

(294) Ryu, S.; Liu, B.; Qin, F. Low pH Potentiates Both Capsaicin Binding and Channel Gating of VR1 Receptors. *The Journal of General Physiology* **2003**, *122* (1), 45–61. https://doi.org/10.1085/jgp.200308847.

(295) Lanzarini, E.; Antognazza, M. R.; Biso, M.; Ansaldo, A.; Laudato, L.; Bruno, P.; Metrangolo, P.; Resnati, G.; Ricci, D.; Lanzani, G. Polymer-Based Photocatalytic Hydrogen Generation. *J. Phys. Chem. C* **2012**, *116* (20), 10944–10949. https://doi.org/10.1021/jp212107f.

(296) Antognazza, M. R.; Abdel Aziz, I.; Lodola, F. Use of Exogenous and Endogenous Photomediators as Efficient ROS Modulation Tools: Results and Perspectives for Therapeutic Purposes. *Oxidative Medicine and Cellular Longevity* **2019**, *2019*, 1–14. https://doi.org/10.1155/2019/2867516.

(297) Chen, L.; Yamane, S.; Mizukado, J.; Suzuki, Y.; Kutsuna, S.; Uchimaru, T.; Suda, H. ESR Study of Singlet Oxygen Generation and Its Behavior during the Photo-Oxidation of P3HT in Solution. *Chemical Physics Letters* **2015**, *624*, 87–92. https://doi.org/10.1016/j.cplett.2015.02.019.

(298) Suppes, G.; Ballard, E.; Holdcroft, S. Aqueous Photocathode Activity of Regioregular Poly(3-Hexylthiophene). *Polym. Chem.* **2013**, *4* (20), 5345. https://doi.org/10.1039/c3py00143a.

(299) Merrill, D. R.; Bikson, M.; Jefferys, J. G. R. Electrical Stimulation of Excitable Tissue: Design of Efficacious and Safe Protocols. *Journal of Neuroscience Methods* **2005**, *141* (2), 171–198. https://doi.org/10.1016/j.jneumeth.2004.10.020.

(300) Cogan, S. F. Neural Stimulation and Recording Electrodes. *Annu. Rev. Biomed. Eng.* **2008**, *10* (1), 275–309. https://doi.org/10.1146/annurev.bioeng.10.061807.160518.

(301) Halliwell, B. Biochemistry of Oxidative Stress. *Biochemical Society Transactions* **2007**, *35* (5), 1147–1150. https://doi.org/10.1042/BST0351147.

(302) Tortiglione, C.; Antognazza, M. R.; Tino, A.; Bossio, C.; Marchesano, V.; Bauduin, A.; Zangoli, M.; Morata, S. V.; Lanzani, G. Semiconducting Polymers Are Light Nanotransducers in Eyeless Animals. *Sci. Adv.* **2017**, *3* (1), e1601699. https://doi.org/10.1126/sciadv.1601699.

(303) Negri, S.; Faris, P.; Tullii, G.; Vismara, M.; Pellegata, A. F.; Lodola, F.; Guidetti, G.; Rosti, V.; Antognazza, M. R.; Moccia, F. Conjugated Polymers Mediate Intracellular Ca2+ Signals in Circulating Endothelial Colony Forming Cells through the Reactive Oxygen Species-Dependent Activation of Transient Receptor Potential Vanilloid 1 (TRPV1). *Cell Calcium* **2022**, *101*, 102502. https://doi.org/10.1016/j.ceca.2021.102502.

(304) Bossio, C.; Abdel Aziz, I.; Tullii, G.; Zucchetti, E.; Debellis, D.; Zangoli, M.; Di Maria, F.; Lanzani, G.; Antognazza, M. R. Photocatalytic Activity of Polymer Nanoparticles Modulates Intracellular Calcium Dynamics and Reactive Oxygen Species in HEK-293 Cells. *Front. Bioeng. Biotechnol.* **2018**, *6*, 114. https://doi.org/10.3389/fbioe.2018.00114.

(305) Moros, M.; Lewinska, A.; Onorato, G.; Antognazza, M. R.; Di Francesca, M.; Blasio, M.; Lanzani, G.; Tino, A.; Wnuk, M.; Tortiglione, C. Light-Triggered Modulation of Cell Antioxidant Defense by Polymer Semiconducting Nanoparticles in a Model

Organism. *MRS Communications* **2018**, *8* (3), 918–925. https://doi.org/10.1557/mrc.2018.104.

(306) Rand, D.; Jakešová, M.; Lubin, G.; Vėbraitė, I.; David-Pur, M.; Đerek, V.; Cramer, T.; Sariciftci, N. S.; Hanein, Y.; Głowacki, E. D. Direct Electrical Neurostimulation with Organic Pigment Photocapacitors. *Advanced Materials* **2018**, *30* (25), 1707292. https://doi.org/10.1002/adma.201707292.

(307) Jakešová, M.; Silverå Ejneby, M.; Đerek, V.; Schmidt, T.; Gryszel, M.; Brask, J.; Schindl, R.; Simon, D. T.; Berggren, M.; Elinder, F.; Głowacki, E. D. Optoelectronic Control of Single Cells Using Organic Photocapacitors. *Sci. Adv.* **2019**, *5* (4), eaav5265. https://doi.org/10.1126/sciadv.aav5265.

(308) Mosconi, E.; Salvatori, P.; Saba, M. I.; Mattoni, A.; Bellani, S.; Bruni, F.; Santiago Gonzalez, B.; Antognazza, M. R.; Brovelli, S.; Lanzani, G.; Li, H.; Brédas, J.-L.; De Angelis, F. Surface Polarization Drives Photoinduced Charge Separation at the P3HT/Water Interface. *ACS Energy Lett.* **2016**, *1* (2), 454–463. https://doi.org/10.1021/acsenergylett.6b00197.

(309) Benfenati, F.; Lanzani, G. Reply to: Questions about the Role of P3HT Nanoparticles in Retinal Stimulation. *Nat. Nanotechnol.* **2021**, *16* (12), 1333–1336. https://doi.org/10.1038/s41565-021-01043-7.

(310) Chiaravalli, G.; Manfredi, G.; Sacco, R.; Lanzani, G. Photoelectrochemistry and Drift–Diffusion Simulations in a Polythiophene Film Interfaced with an Electrolyte. *ACS Appl. Mater. Interfaces* **2021**, *13* (30), 36595–36604. https://doi.org/10.1021/acsami.1c10158.

(311) Bellani, S.; Fazzi, D.; Bruno, P.; Giussani, E.; Canesi, E. V.; Lanzani, G.; Antognazza, M. R. Reversible P3HT/Oxygen Charge Transfer Complex Identification in Thin Films Exposed to Direct Contact with Water. *J. Phys. Chem. C* **2014**, *118* (12), 6291–6299. https://doi.org/10.1021/jp4119309.

(312) Benfenati, V.; Martino, N.; Antognazza, M. R.; Pistone, A.; Toffanin, S.; Ferroni, S.; Lanzani, G.; Muccini, M. Photostimulation of Whole-Cell Conductance in Primary Rat Neocortical Astrocytes Mediated by Organic Semiconducting Thin Films. *Adv. Healthcare Mater.* **2014**, *3* (3), 392–399. https://doi.org/10.1002/adhm.201300179.

(313) Sinning, A.; Hübner, C. A. Minireview: pH and Synaptic Transmission. *FEBS Letters* **2013**, *587* (13), 1923–1928. https://doi.org/10.1016/j.febslet.2013.04.045.

(314) Zeng, W.-Z.; Liu, D.-S.; Liu, L.; She, L.; Wu, L.-J.; Xu, T.-L. Activation of Acid-Sensing Ion Channels by Localized Proton Transient Reveals Their Role in Proton Signaling. *Sci Rep* **2015**, *5* (1), 14125. https://doi.org/10.1038/srep14125.

(315) Geim, A. K. Graphene: Status and Prospects. *Science* **2009**, *324* (5934), 1530–1534. https://doi.org/10.1126/science.1158877.

(316) Kim, H.; Byun, J.; Bae, S.; Ahmed, T.; Zhu, J.; Kwon, S.; Lee, Y.; Min, S.; Wolf, C.; Seo, H.; Ahn, J.; Lee, T. On-Fabrication Solid-State N-Doping of Graphene by an Electron-Transporting Metal Oxide Layer for Efficient Inverted Organic Solar Cells. *Advanced Energy Materials* **2016**, *6* (12), 1600172. https://doi.org/10.1002/aenm.201600172.

(317) Zhong, S.; Zhong, J. Q.; Mao, H. Y.; Wang, R.; Wang, Y.; Qi, D. C.; Loh, K. P.; Wee, A. T. S.; Chen, Z. K.; Chen, W. CVD Graphene as Interfacial Layer to Engineer the Organic Donor–Acceptor Heterojunction Interface Properties. *ACS Appl. Mater. Interfaces* **2012**, *4* (6), 3134–3140. https://doi.org/10.1021/am300887j.

(318) Yang‡, Q.-D.; Li, J.; Cheng, Y.; Li, H.-W.; Guan, Z.; Yu, B.; Tsang, S.-W. Graphene Oxide as an Efficient Hole-Transporting Material for High-Performance Perovskite Solar Cells with Enhanced Stability. *J. Mater. Chem. A* **2017**, *5* (20), 9852–9858. https://doi.org/10.1039/C7TA01752A.

(319) Muchuweni, E.; Martincigh, B. S.; Nyamori, V. O. Organic Solar Cells: Current Perspectives on Graphene-based Materials for Electrodes, Electron Acceptors and Interfacial Layers. *Int J Energy Res* **2021**, *45* (5), 6518–6549. https://doi.org/10.1002/er.6301.

(320) Velasco Davoise, L.; Díez-Pascual, A. M.; Peña Capilla, R. Application of Graphene-Related Materials in Organic Solar Cells. *Materials* **2022**, *15* (3), 1171. https://doi.org/10.3390/ma15031171.

(321) Koo, D.; Jung, S.; Seo, J.; Jeong, G.; Choi, Y.; Lee, J.; Lee, S. M.; Cho, Y.; Jeong, M.; Lee, J.; Oh, J.; Yang, C.; Park, H. Flexible Organic Solar Cells Over 15% Efficiency with Polyimide-Integrated Graphene Electrodes. *Joule* **2020**, *4* (5), 1021–1034. https://doi.org/10.1016/j.joule.2020.02.012.

(322) Novoselov, K. S.; Fal'ko, V. I.; Colombo, L.; Gellert, P. R.; Schwab, M. G.; Kim, K. A Roadmap for Graphene. *Nature* **2012**, *490* (7419), 192–200. https://doi.org/10.1038/nature11458.

(323) Reina, G.; González-Domínguez, J. M.; Criado, A.; Vázquez, E.; Bianco, A.; Prato, M. Promises, Facts and Challenges for Graphene in Biomedical Applications. *Chem. Soc. Rev.* **2017**, *46* (15), 4400–4416. https://doi.org/10.1039/C7CS00363C.

(324) Fabbri, R.; Saracino, E.; Treossi, E.; Zamboni, R.; Palermo, V.; Benfenati, V. Graphene Glial-Interfaces: Challenges and Perspectives. *Nanoscale* **2021**, *13* (8), 4390–4407. https://doi.org/10.1039/D0NR07824G.

(325) Zhang, X.; Lee, H.; Zhang, Y.; Walmsley, T. S.; Li, D.; Levine, E.; Xu, Y.-Q. Probing Light-Stimulated Activities in the Retina via Transparent Graphene Electrodes. *ACS Appl. Bio Mater.* **2022**, *5* (1), 305–312. https://doi.org/10.1021/acsabm.1c01091.

(326) Kshirsagar, P.; Dickreuter, S.; Mierzejewski, M.; Burkhardt, C. J.; Chassé, T.; Fleischer, M.; Jones, P. D. Transparent Graphene/PEDOT:PSS Microelectrodes for Electro- and Optophysiology. *Adv Materials Technologies* **2019**, *4* (1), 1800318. https://doi.org/10.1002/admt.201800318.

(327) Yan, L.; Zhao, B.; Liu, X.; Li, X.; Zeng, C.; Shi, H.; Xu, X.; Lin, T.; Dai, L.; Liu, Y. Aligned Nanofibers from Polypyrrole/Graphene as Electrodes for Regeneration of Optic Nerve via Electrical Stimulation. *ACS Appl. Mater. Interfaces* **2016**, *8* (11), 6834–6840. https://doi.org/10.1021/acsami.5b12843.

(328) NoroozOliaei, M.; Riazi Esfahani, H.; Abrishamian, M. S. Graphene Coated Dielectric Resonator Antenna for Modeling the Photoreceptors at Visible Spectrum. *Heliyon* **2022**, *8* (6), e09611. https://doi.org/10.1016/j.heliyon.2022.e09611.

(329) Chen, C.-H.; Lin, C.-T.; Hsu, W.-L.; Chang, Y.-C.; Yeh, S.-R.; Li, L.-J.; Yao, D.-J. A Flexible Hydrophilic-Modified Graphene Microprobe for Neural and Cardiac Recording. *Nanomedicine: Nanotechnology, Biology and Medicine* **2013**, *9* (5), 600–604. https://doi.org/10.1016/j.nano.2012.12.004.

(330) Nguyen, D.; Valet, M.; Dégardin, J.; Boucherit, L.; Illa, X.; De La Cruz, J.; Del Corro, E.; Bousquet, J.; Garrido, J. A.; Hébert, C.; Picaud, S. Novel Graphene Electrode for Retinal Implants: An in Vivo Biocompatibility Study. *Front. Neurosci.* **2021**, *15*, 615256. https://doi.org/10.3389/fnins.2021.615256.

(331) De La Cruz, J.; Nguyen, D.; Illa, X.; Bousquet, J.; Pérez-Marín, A. P.; Del Corro, E.; Picaud, S.; Garrido, J. A.; Hebert, C. Single and Multisite Graphene-Based Electroretinography Recording Electrodes: A Benchmarking Study. *Adv Materials Technologies* **2022**, *7* (6), 2101181. https://doi.org/10.1002/admt.202101181.

(332) Kireev, D.; Shokoohimehr, P.; Ernst, M.; Montes, V. R.; Srikantharajah, K.; Maybeck, V.; Wolfrum, B.; Offenhäusser, A. Fabrication of Ultrathin and Flexible Graphene-Based Devices for in Vivo Neuroprosthetics. *MRS Advances* **2018**, *3* (29), 1621–1627. https://doi.org/10.1557/adv.2018.94.

(333) DiFrancesco, M. L.; Colombo, E.; Papaleo, E. D.; Maya-Vetencourt, J. F.; Manfredi, G.; Lanzani, G.; Benfenati, F. A Hybrid P3HT-Graphene Interface for Efficient Photostimulation of Neurons. *Carbon* **2020**, *162*, 308–317. https://doi.org/10.1016/j.carbon.2020.02.043.

(334) Francia, S.; Di Marco, S.; DiFrancesco, M. L.; Ferrari, D. V.; Shmal, D.; Cavalli, A.; Pertile, G.; Attanasio, M.; Maya-Vetencourt, J. F.; Manfredi, G.; Lanzani, G.; Benfenati, F.; Colombo, E. P3ht-Graphene Device for the Restoration of Visual Properties in a Rat Model of Retinitis Pigmentosa. *Adv Materials Technologies* **2023**, *8* (6), 2201467. https://doi.org/10.1002/admt.202201467.

(335) Khizar, S.; Zine, N.; Errachid, A.; Jaffrezic-Renault, N.; Elaissari, A. Microfluidic-based Nanoparticle Synthesis and Their Potential Applications. *Electrophoresis* **2022**, *43* (7–8), 819–838. https://doi.org/10.1002/elps.202100242.

(336) Schubert, S.; Delaney, Jr, J. T.; Schubert, U. S. Nanoprecipitation and Nanoformulation of Polymers: From History to Powerful Possibilities beyond Poly(Lactic Acid). *Soft Matter* **2011**, *7* (5), 1581–1588. https://doi.org/10.1039/C0SM00862A.

(337) Bondelli, G.; Sardar, S.; Chiaravalli, G.; Vurro, V.; Paternò, G. M.; Lanzani, G.; D'Andrea, C. Shedding Light on Thermally Induced Optocapacitance at the Organic Biointerface. *J. Phys. Chem. B* **2021**, *125* (38), 10748–10758. https://doi.org/10.1021/acs.jpcb.1c06054.

(338) Jiang, X. M.; Österbacka, R.; Korovyanko, O.; An, C. P.; Horovitz, B.; Janssen, R. A. J.; Vardeny, Z. V. [No Title Found]. *Adv. Funct. Mater.* **2002**, *12* (9), 587–597. https://doi.org/10.1002/1616-3028(20020916)12:9<587::AID-ADFM587>3.0.CO;2-T.

(339) Risk Factors Associated with Age-Related Macular Degeneration. *Ophthalmology* **2000**, *107* (12), 2224–2232. https://doi.org/10.1016/S0161-6420(00)00409-7.

(340) Berger, P. R.; Kim, M. Polymer Solar Cells: P3HT:PCBM and Beyond. *Journal of Renewable and Sustainable Energy* **2018**, *10* (1), 013508. https://doi.org/10.1063/1.5012992.

(341) Ulum, M. S.; Sesa, E.; Nismayanti, A.; Belcher, W. Donor Acceptor Ratio Effect on P3HT:PCBM Nanoparticulate Organic Photovoltaic Device Performance. *J. Phys.: Conf. Ser.* **2019**, *1242* (1), 012033. https://doi.org/10.1088/1742-6596/1242/1/012033.

(342) Knappett, B. R.; Abdulkin, P.; Ringe, E.; Jefferson, D. A.; Lozano-Perez, S.; Rojas, T. C.; Fernández, A.; Wheatley, A. E. H. Characterisation of Co@Fe3O4 Core@shell Nanoparticles Using Advanced Electron Microscopy. *Nanoscale* **2013**, *5* (13), 5765. https://doi.org/10.1039/c3nr33789h.

(343) Browning, N. D.; Chisholm, M. F.; Pennycook, S. J. Atomic-Resolution Chemical Analysis Using a Scanning Transmission Electron Microscope. *Nature* **1993**, *366* (6451), 143–146. https://doi.org/10.1038/366143a0.

(344) Chambon, S.; Schatz, C.; Sébire, V.; Pavageau, B.; Wantz, G.; Hirsch, L. Organic Semiconductor Core–Shell Nanoparticles Designed through Successive Solvent Displacements. *Mater. Horiz.* **2014**, *1* (4), 431–438. https://doi.org/10.1039/C4MH00021H.

(345) Vitale, S. A.; Katz, J. L. Liquid Droplet Dispersions Formed by Homogeneous Liquid−Liquid Nucleation: "The Ouzo Effect." *Langmuir* **2003**, *19* (10), 4105–4110. https://doi.org/10.1021/la026842o.

(346) *ISO 22412:2017; Particle Size Analysis—Dynamic Light Scattering (DLS). International Standard Organization: Geneva, Switzerland, 2017. Available Online: Https://Www.Iso.Org/Standard/65410.Html*.

(347) Bhattacharjee, S. DLS and Zeta Potential – What They Are and What They Are Not? *Journal of Controlled Release* **2016**, *235*, 337–351. https://doi.org/10.1016/j.jconrel.2016.06.017.

(348) Louarn, G.; Trznadel, M.; Buisson, J. P.; Laska, J.; Pron, A.; Lapkowski, M.; Lefrant, S. Raman Spectroscopic Studies of Regioregular Poly(3-Alkylthiophenes). *J. Phys. Chem.* **1996**, *100* (30), 12532–12539. https://doi.org/10.1021/jp960104p.

(349) Baibarac, M.; Lapkowski, M.; Pron, A.; Lefrant, S.; Baltog, I. SERS Spectra of Poly(3-Hexylthiophene) in Oxidized and Unoxidized States. *J. Raman Spectrosc.* **1998**, *29* (9), 825–832. https://doi.org/10.1002/(SICI)1097-4555(199809)29:9<825::AID-JRS309>3.0.CO;2-2.

(350) Alley, N. J.; Liao, K.-S.; Andreoli, E.; Dias, S.; Dillon, E. P.; Orbaek, A. W.; Barron, A. R.; Byrne, H. J.; Curran, S. A. Effect of Carbon Nanotube-Fullerene Hybrid Additive on P3HT:PCBM Bulk-Heterojunction Organic Photovoltaics. *Synthetic Metals* **2012**, *162* (1–2), 95–101. https://doi.org/10.1016/j.synthmet.2011.11.017.

(351) Kline, R. J.; McGehee, M. D.; Kadnikova, E. N.; Liu, J.; Fréchet, J. M. J.; Toney, M. F. Dependence of Regioregular Poly(3-Hexylthiophene) Film Morphology and Field-Effect Mobility on Molecular Weight. *Macromolecules* **2005**, *38* (8), 3312–3319. https://doi.org/10.1021/ma047415f.

(352) Brinkmann, M.; Rannou, P. Molecular Weight Dependence of Chain Packing and Semicrystalline Structure in Oriented Films of Regioregular Poly(3-Hexylthiophene) Revealed by High-Resolution Transmission Electron Microscopy. *Macromolecules* **2009**, *42* (4), 1125–1130. https://doi.org/10.1021/ma8023415.

(353) Dante, M.; Peet, J.; Nguyen, T.-Q. Nanoscale Charge Transport and Internal Structure of Bulk Heterojunction Conjugated Polymer/Fullerene Solar Cells by Scanning Probe Microscopy. *J. Phys. Chem. C* **2008**, *112* (18), 7241–7249. https://doi.org/10.1021/jp712086q.

(354) Yang, H.; Xia, H.; Wang, G.; Peng, J.; Qiu, F. Insights into Poly(3-Hexylthiophene)- *b* -Poly(Ethylene Oxide) Block Copolymer: Synthesis and Solvent-Induced Structure Formation in Thin Films. *J. Polym. Sci. A Polym. Chem.* **2012**, *50* (24), 5060–5067. https://doi.org/10.1002/pola.26353.

(355) Nicolet, C.; Deribew, D.; Renaud, C.; Fleury, G.; Brochon, C.; Cloutet, E.; Vignau, L.; Wantz, G.; Cramail, H.; Geoghegan, M.; Hadziioannou, G. Optimization of the Bulk Heterojunction Composition for Enhanced Photovoltaic Properties: Correlation between the Molecular Weight of the Semiconducting Polymer and Device Performance. *J. Phys. Chem. B* **2011**, *115* (44), 12717–12727. https://doi.org/10.1021/jp207669j.

(356) Holmes, N. P.; Burke, K. B.; Sista, P.; Barr, M.; Magurudeniya, H. D.; Stefan, M. C.; Kilcoyne, A. L. D.; Zhou, X.; Dastoor, P. C.; Belcher, W. J. Nano-Domain Behaviour in P3HT:PCBM Nanoparticles, Relating Material Properties to Morphological Changes. *Solar Energy Materials and Solar Cells* **2013**, *117*, 437–445. https://doi.org/10.1016/j.solmat.2013.06.003.

(357) Chirvase, D.; Parisi, J.; Hummelen, J. C.; Dyakonov, V. Influence of Nanomorphology on the Photovoltaic Action of Polymer–Fullerene Composites. *Nanotechnology* **2004**, *15* (9), 1317–1323. https://doi.org/10.1088/0957-4484/15/9/035.

(358) Millstone, J. E.; Kavulak, D. F. J.; Woo, C. H.; Holcombe, T. W.; Westling, E. J.; Briseno, A. L.; Toney, M. F.; Fréchet, J. M. J. Synthesis, Properties, and Electronic Applications of Size-Controlled Poly(3-Hexylthiophene) Nanoparticles. *Langmuir* **2010**, *26* (16), 13056–13061. https://doi.org/10.1021/la1022938.

(359) Malloy, A.; Carr, B. NanoParticle Tracking Analysis – The Halo™ System. *Part & Part Syst Charact* **2006**, *23* (2), 197–204. https://doi.org/10.1002/ppsc.200601031.

(360) Filipe, V.; Hawe, A.; Jiskoot, W. Critical Evaluation of Nanoparticle Tracking Analysis (NTA) by NanoSight for the Measurement of Nanoparticles and Protein Aggregates. *Pharm Res* **2010**, *27* (5), 796–810. https://doi.org/10.1007/s11095-010-0073-2.

(361) *Guideline, I. C. H. "Q3c (R6) on Impurities: Guideline for Residual Solvents." International Council for Harmonisation of Technical Requirements for Pharmaceuticals for Human Use 4 (2016): 1-51.*

(362) Newton, J. R.; Ellsworth, C.; Miyakawa, T.; Tonegawa, S.; Sur, M. Acceleration of Visually Cued Conditioned Fear through the Auditory Pathway. *Nat Neurosci* **2004**, *7* (9), 968–973. https://doi.org/10.1038/nn1306.

(363) Ross, M.; Ofri, R. The Future of Retinal Gene Therapy: Evolving from Subretinal to Intravitreal Vector Delivery. *Neural Regen Res* **2021**, *16* (9), 1751. https://doi.org/10.4103/1673-5374.306063.

(364) Chiang, J. (Pei-wen); Trzupek, K. The Current Status of Molecular Diagnosis of Inherited Retinal Dystrophies: *Current Opinion in Ophthalmology* **2015**, *26* (5), 346–351. https://doi.org/10.1097/ICU.0000000000000185.

(365) Bi, A.; Cui, J.; Ma, Y.-P.; Olshevskaya, E.; Pu, M.; Dizhoor, A. M.; Pan, Z.-H. Ectopic Expression of a Microbial-Type Rhodopsin Restores Visual Responses in Mice with Photoreceptor Degeneration. *Neuron* **2006**, *50* (1), 23–33. https://doi.org/10.1016/j.neuron.2006.02.026.

(366) Sengupta, A.; Chaffiol, A.; Macé, E.; Caplette, R.; Desrosiers, M.; Lampič, M.; Forster, V.; Marre, O.; Lin, J. Y.; Sahel, J.; Picaud, S.; Dalkara, D.; Duebel, J. Red-shifted Channelrhodopsin Stimulation Restores Light Responses in Blind Mice, Macaque Retina, and Human Retina. *EMBO Mol Med* **2016**, *8* (11), 1248–1264. https://doi.org/10.15252/emmm.201505699.

(367) ICNIRP Guidelines on Limits of Exposure to Incoherent Visible and Infrared Radiation. *Health Physics* **2013**, *105* (1), 74–96. https://doi.org/10.1097/HP.0b013e318289a611.

(368) Morizur, L.; Herardot, E.; Monville, C.; Ben M'Barek, K. Human Pluripotent Stem Cells: A Toolbox to Understand and Treat Retinal Degeneration. *Molecular and Cellular Neuroscience* **2020**, *107*, 103523. https://doi.org/10.1016/j.mcn.2020.103523.

(369) Holan, V.; Palacka, K.; Hermankova, B. Mesenchymal Stem Cell-Based Therapy for Retinal Degenerative Diseases: Experimental Models and Clinical Trials. *Cells* **2021**, *10* (3), 588. https://doi.org/10.3390/cells10030588.

(370) Malatesta, M. Transmission Electron Microscopy as a Powerful Tool to Investigate the Interaction of Nanoparticles with Subcellular Structures. *IJMS* **2021**, *22* (23), 12789. https://doi.org/10.3390/ijms222312789.

(371) Kaszuba, M.; McKnight, D.; Connah, M. T.; McNeil-Watson, F. K.; Nobbmann, U. Measuring Sub Nanometre Sizes Using Dynamic Light Scattering. *J Nanopart Res* **2008**, *10* (5), 823–829. https://doi.org/10.1007/s11051-007-9317-4.

(372) Hassan, P. A.; Rana, S.; Verma, G. Making Sense of Brownian Motion: Colloid Characterization by Dynamic Light Scattering. *Langmuir* **2015**, *31* (1), 3–12. https://doi.org/10.1021/la501789z.

(373) Behzadi, S.; Serpooshan, V.; Tao, W.; Hamaly, M. A.; Alkawareek, M. Y.; Dreaden, E. C.; Brown, D.; Alkilany, A. M.; Farokhzad, O. C.; Mahmoudi, M. Cellular Uptake of Nanoparticles: Journey inside the Cell. *Chem. Soc. Rev.* **2017**, *46* (14), 4218–4244. https://doi.org/10.1039/C6CS00636A.

(374) Ivashkina, O. I.; Toropova, K. A.; Roshchina, M. A.; Anokhin, K. V. Acquisition of a Conditioned Fear Reaction to a Light Stimulus in Mice: Comparison with Learning in Response to a Sound Stimulus. *Neurosci Behav Physi* **2017**, *47* (8), 994–998. https://doi.org/10.1007/s11055-017-0501-4.

APPENDIX

PUBLICATIONS

Chiaravalli, G.; Ravasenga, T.; Colombo, E.; Jasnoor; Francia, S.; Di Marco, S.; Sacco, R.; Pertile, G.; Benfenati, F.; Lanzani, G. The Light-Dependent Pseudo-Capacitive Charging of Conjugated Polymer Nanoparticles Is Coupled to Depolarization of the Neuronal Membrane. *Phys. Chem. Chem. Phys.* **2023**. https://doi.org/10.1039/D3CP04386J.

POSTER PRESENTATIONS

"Photo stimulation of dystrophic retinal explants after chronic and acute exposure to conjugated polymer nanoparticles"

- Federation of European Neuroscience Societies (FENS) July 2022, Paris, France.
- Society for Neuroscience (SfN) November 2022, San Diego, USA.
- 46th Annual Meeting of the Japan Neuroscience Society (JNS) August 2023, Sendai, Japan.
- European Retina Meeting (ERM) September 2023, Tübingen, Germany.